12-2010

Synthesis, Stabilization, and Characterization of Metal Nanoparticles

Gregory White ii
Clemson University, gwhite@clemson.edu

SYNTHESIS, STABILIZATION, AND CHARACTERIZATION OF METAL NANOPARTICLES

A Dissertation
Presented to
the Graduate School of
Clemson University

In Partial Fulfillment
of the Requirements for the Degree
Doctor of Philosophy
Chemical Engineering

---

by
Gregory Von White II
December 2010

Accepted by:
Dr. Christopher L. Kitchens, Committee Chair
Dr. Douglas E. Hirt
Dr. Scott M. Husson
Dr. Alexey A. Vertegel

ABSTRACT

Wet chemical synthesis techniques offer the ability to control various nanoparticle characteristics including size, shape, dispersibility in both aqueous and organic solvents, and tailored surface chemistries appropriate for different applications. Large quantities of stabilizing ligands or surfactants are often required during synthesis to achieve these nanoparticle characteristics. Unfortunately, excess reaction byproducts, surfactants, and ligands remaining in solution after nanoparticle synthesis can impede application, and therefore post-synthesis purification must be employed. A liquid-liquid solvent/anti-solvent pair (typically ethanol/toluene or ethanol/hexane for gold nanoparticles, GNPs) can be used to both purify and size-selectively fractionate hydrophobically modified nanoparticles. Alternatively, carbon dioxide may be used in place of a liquid anti-solvent, a "green" approach, enabling both nanoparticle purification and size-selective fractionation while simultaneously eliminating mixed solvent waste and allowing solvent recycle. We have used small-angle neutron scattering (SANS) to investigate the ligand structure and composition response of alkanethiol modified gold and silver nanoparticles at varying anti-solvent conditions (CO_2 or ethanol). The ligand lengths and ligand solvation for alkanethiol gold and silver NPs were found to decrease with increased anti-solvent concentrations directly impacting their dispersibility in solution. Calculated Flory-Huggins interaction parameters support our SANS study for dodecanethiol dispersibility in the mixed organic solvents. This research has led to a greater understanding of the liquid-liquid precipitation process for metal nanoparticles, and provides critical results for future interaction energy modeling.

DEDICATION

This dissertation is dedicated to my amazing, loving, and supportive parents (Greg and Armie). Thank you for providing me with the structure and tools necessary to take on graduate school, as well as show me how to be a good husband and father through your own marriage and parenting. Thank you for always encouraging me, praying with and for me, and listening to me. Thank you for flying numerous times from your home in Hawaii to visit me, my wife, and your grandsons. Thank you for believing in me, even when I wasn't sure, and thanks for just being you. I love you both. God bless you.

ACKNOWLEDEMENTS

First and foremost, I would like to thank God for granting me the knowledge, wisdom, talent, skills, and hard work ethics to succeed here at Clemson University. Moreover, I thank God for the many blessings and support He has bestowed upon me through family, friends, advisors, professors, collaborators, students, and colleagues. Without all of these blessings and support systems, this dissertation would not have been imaginable.

I would also like to express my sincere appreciation to the following individuals:

My loving wife Marta: thank you for always being there through all of the good times and bad, for praying with and for me, simultaneously loving and caring for me, our son Gregory, and our son on the way, José Antonio. Thank you for constantly encouraging me and always believing in me. Not many people can finish their doctoral degree, be a newlywed, and become a full time mother all at the same time! Wow, you are truly an amazing woman and a true gift from God. *Gracias Mi Chica Preciosa*.

My sons Gregory and José Antonio: although you are too young to understand (or are not quite born yet), both of you have helped me stay on track to finish my dissertation. Gregory your smiles, hugs, and kisses were more than enough to keep me motivated. José Antonio, news of your up and coming delivery was more than enough to increase my productivity which enabled me to tie up all of my research into this document. Thanks boys!

My Momma, Nancy: thanks for loving and supporting me in all that I do. Thanks for care packages, emails, talking on the phone, and even visits. No words can describe how you have helped me through this process.

My wonderful and awesome in-laws Don José and Doña Maria Elena: thank you for the constant prayers, support, and always believing in me. God bless you! *A mis suegros favoritos: muchas gracias por sus constantes oraciones,apoyo y por siempre creer en mi. Que Dios los bendiga!*

Dr. Christopher L. Kitchens: Thank you for the unique and amazing opportunity you gave me with this research project. Through your sound guidance, direction, insightful discussions, encouragement, and extreme patience I have significantly matured as a researcher improving my analytical skills and problem solving abilities, enhanced my capability to interpret data, and last but not least, I have vastly improved my writing skills. Thanks for being a great advisor, mentor, and friend.

My dissertation committee, Dr. Hirt, Dr. Husson, and Dr. Vertegel: Thank you all for taking the time to read this dissertation and provide feedback on my work and results.

My fellow lab cohorts: Esteban (and honorary group member Linda), Fiaz, and José Luis. Thanks for allowing me to work beside you fellas and for all of the thoughtful discussions (both research and non-research related), including awesome magic tricks. Thank you to the undergraduate group members who also played a role in this work including Brad, Grant, Petra, and Jake.

To all of those who supported me in various ways during my time at Clemson, including (but not limited to) Team Gallagher (in particular Jeff and Taco Bell), Fr.

Sandy McDonald, Fr. Emmanuel, Fr. Bernard, Fred, Jack, Becky, Chhavi, Marlon, Mary, Erick, Steven aka “Moose”, Dr. Christopher B. Roberts, Steven Saunders, Kendall Hurst, Jane E. Jacobi, Dr. Tremayne O. Waller, Dr. Lisa C. Benson, Annette Vandiver, and last but certainly not least the soon to be Dr. Kyle Gipson.

TABLE OF CONTENTS

Table of Contents (Continued)

Page

Table of Contents (Continued)

Page

Table of Contents (Continued)

Page

Table of Contents (Continued)

Page

LIST OF TABLES

Page

Table

LIST OF FIGURES

Page

Figure

List of Figures (Continued)

Page

Figure

List of Figures (Continued)

Page

Figure

List of Figures (Continued)

Page

Figure

CHAPTER ONE

INTRODUCTION AND BACKGROUND

Richard P. Feynman, a world renowned physicist presented a speech entitled, "There's Plenty of Room at the Bottom" during the annual American Physical Society meeting at the California Institute of Technology in 1959.[1] Feynman's speech is said to be the first account publically describing the manipulation of matter on a tiny scale, for example the possibility of writing 24 volumes of the Encyclopedia Britannica on the head of a pin. 50 years later, significant advances in the field of nanotechnology are making Feynman's speech more of a reality, with applications in nearly all fields. Albeit Feynman is credited with creating nanotechnology, nanoparticles have been around since ancient times.

Nano comes from the Greek word *nanos*, meaning dwarf or extremely small. Today, we denote nano to be 10^{-9} m in SI units. The first evidence of nanotechnology dates back to ~2,000 B.C., where silver and gold nanoparticles were used to create beautiful stained glass windows due to their unique optical properties.[2] The Romans mixed solutions of nano gold and silver (nanoparticles) to produce a variety of colored glasses, including ruby red and yellow. The Romans believed an *Elixir of Life* could be created using solutions of soluble gold which could cure many bodily ailments and increase both mental and physical abilities.[3] Today researchers and scientists are using nanoparticles to fight cancer,[4] catalyze various reactions,[5, 6] and as chemical and biological sensors.[7, 8] Over the past 20 years, significant advances have been made in the

field of nanotechnology; particularly for metal nanoparticles, whose properties differ from their bulk counterparts.

Silver and gold nanoparticles have unique size and shape dependent properties (optical,[9, 10] chemical,[11] photothermal,[12] and catalytic),[5, 13] making them useful for a variety of applications. Their optical properties are a result of the collective excitation of free electrons in response to light energy—this phenomena is commonly known as surface plasmon resonance.[9] The plasmon resonance of silver and gold nanoparticles is readily tunable with the nanoparticle size, shape, surface chemistry, and surrounding media (refractive index)—making them ideal for sensor applications.[7, 8, 14] For example, Storhoff et al. utilized ~13 nm gold nanoparticles modified with twelve nucleotides to determine errors in polynucleotide sequences based on colorimetric changes; a shift in color from red to blue was shown to indicate nanoparticle agglomeration and corresponded to errors in the target nucleotide sequence.[15] Similarly, Nath et al. tethered ~13.4 nm gold nanoparticles to a glass substrate for application as a biomolecular sensor, capable of detecting the presence and concentration of fibrinogen by variation in plasmon resonance intensity (measured by ultravisible light spectroscopy, UV-VIS).[16] Because the changes in plasmon resonance for these gold nanoparticles are colorimetric, Nath suggested that widely available optical scanners could be used to determine concentration of fibrinogen in lieu of UV-VIS spectrophotometers.[16]

Gold and silver nanoparticles have also demonstrated potential as electrochemical sensors and as catalysts. For example, Jena and Raj attached gold nanoparticles (5 - 6 nm) onto gold electrodes to simultaneously detect arsenic and

mercury at sub parts per billion concentrations based on electrochemical responses measured by voltammetery.[11] Geng et al. demonstrated the size-dependent catalytic properties of gold nanoparticles which were deposited onto glassy carbon electrodes.[17] Here, the gold nanoparticles aided in the oxidation reaction of carbon monoxide to carbon dioxide at basic conditions. This work demonstrated that smaller gold nanoparticles (2 - 6 nm in diameter) are much more catalytically reactive than larger nanoparticles (greater than 12 nm in diameter) as determined by cyclic voltammetry measurements;[17] comparably, bulk gold is inert.[18]

Research and development of biomedical applications which utilize the unique properties of gold and silver nanoparticles is rapidly increasing. For example, Ding et al used gold nanorods as targeted contrast agents for cancer cells, observed by both light and electron microscopy.[19] Advances in drug delivery are also evident in the literature.[4, 20] One example includes hybrid vesicle-nanoparticle systems which afford dual purposes. These systems incorporate hydrophobically modified nanoparticles into the bilayer of lipid vesicles (structurally similar to a cell membrane) and can provide medical imaging contrast useful for live tracking, and drug delivery by incorporate hydrophilic drugs into the aqueous core of the vesicle.[20-22] Recently, Bothun et al. demonstrated the ability to load 5.7 nm hydrophobically modified silver nanoparticles into the bilayer of lipid vesicles, and demonstrated that increasing nanoparticle loading increases the size of the overall vesicle;[21] a collaborative investigation with Bothun and coworkers is discussed in Chapter Six utilizing nanoparticles we have synthesized here at Clemson. Other biomedical applications of nanoparticles utilize the photothermal properties of gold

nanoparticles; here, radiation (generally light) energy is absorbed by the metallic nanoparticles and functions as a localized hyperthermia agent.[12, 23, 24] The anti-microbial and anti-bacterial properties of silver and gold nanoparticles are also applicable to consumer products and medical industries.[25-27]

The increasing number of nanoparticle applications necessitates tunable control of size and size-distribution either by optimizing the synthesis conditions or by post-synthesis processing. The focus of this dissertation was the synthesis, stabilization, and characterization of silver and gold nanoparticles. One of the primary objectives of this research was to develop a better fundamental understanding of nanoparticle dispersibility during anti-solvent induced precipitation. Interaction energy models which accurately predict nanoparticle dispersibility are advantageous because they afford the ability to determine the solvent and ligand conditions necessary to isolate a desired nanoparticle size during processing or tune the synthesis solvent composition. These interaction energy models could eliminate unnecessary experimentation and optimization of current nanoparticle processing techniques. While these models are advantageous, current interaction energy models overpredict nanoparticle dispersibility due to assumptions made regarding the stabilizing ligand structure and solvation at predetermined solvent conditions.[28, 29] A primary motivation for this work was to systematically investigate the ligand structure and solvation of hydrophobically stabilized nanoparticles at defined solvent compositions (both good and poor). Prior to the discussion of the research contained in this dissertation, a review of current nanoparticle synthesis and processing techniques is necessary.

Nanoparticle Synthesis

Wet chemical synthesis techniques afford facile control over nanoparticle size, size-distribution, shape, and surface chemistry.[10, 30-36] Two very common synthesis protocols for spherical silver and gold nanoparticles are the Turkevich [30, 31] and Brust methods,[32] which facilitate the nucleation, growth, and stabilization of aqueous and organic populations of nanoparticles, respectively. Both synthesis methods are desirable for varying reasons. For example, adaption of the Turkevich method provides relatively monodisperse populations of nanoparticles in which the surface chemistry can readily modified to facilitate dispersion in both aqueous and organic media.[33] Here, aqueous gold salts are added to hot or boiling citrate solution and particle size control (ranging from 10 to 20 nm in diameter) is afforded by variation of the synthesis time. [30] The citrate functions as both the reducing and stabilizing agents and hence, variation of citrate concentration can also afford size and size-distribution control. A downside to the Turkevich method is that the concentrations of nanoparticles produced is generally low (microgram quantities).[30] Adaptation to the Turkevich method has extended the synthesis from gold to other metal nanoparticles, for example silver, platinum, and palladium.[31] Adding reducing agents like borohydride or ascorbic acid can facilitate faster nucleation or add slow growth stages during nanoparticle synthesis, which provides greater size control. For example, Jana et al. used borohydride to create ~3.5 nm citrate stabilized gold nanoparticles and then used ascorbic acid to vary the particle diameter from 5 to 50 nm, through a seed-mediated growth step.[33]

Comparatively, the Brust method[32] can produce milligram quantities of hydrophobically modified spherical nanoparticles—though the particle size-distributions are generally larger than those produced by the Turkevich method, and therefore necessitate post-synthesis fractionation.[37, 38] Here, a cationic phase transfer catalyst (tetraoctylammonium bromide, TOAB) is employed to transfer gold or silver ions from aqueous solution to an organic solution (typically toluene or chloroform for gold or silver nanoparticles, respectively), where the reduction of the metal ions is achieved by sodium borohydride addition.[32] A downside to the Brust method is that TOAB is both expensive and toxic (generally 2.7 g of TOAB is required to make 0.19 g of silver nanoparticles); hence, post-synthesis purification steps must be employed prior to application.[39, 40]

More recent synthesis protocols have been developed which aim to minimize the quantities of harsh organic solvents and toxic surfactants. For example Liu et al. demonstrated the facile synthesis of gold nanoparticles (~ 6 nm in diameter) by using glucose as the stabilizing agent and sodium borohydride as the reducing agent.[36] The glucose stabilizing chemistry is readily displaced by amine or thiol chemistry, enabling resuspension in organic solvents, like hexane.[36] Similarly, Tan et al. demonstrated the synthesis of gold nanoparticles (~20 nm) where sodium carboxy methyl cellulose (derivative of cellulose) functioned as the reducing and stabilizing agent when reacted at 110 °C for 12 hours.[41] Other sugars including fructose and sucrose have also been used as both the reducing and stabilizing agents for silver nanoparticles.[42] However, the most "green" synthesis approaches for gold and silver nanoparticles thus far employ phytochemicals from renewable resources in addition to the aqueous gold or silver salt

solutions. For example, Shukla et al. demonstrated the synthesis of gold nanoparticles (~15 nm) using soybean extracts as both the reducing and stabilizing agents and demonstrated biocompatibility through cell culture assays.[35] Similarly, Philip et al. used honey as both the reducing and stabilizing agents to produce ~15 nm gold nanoparticles.[43]

Shape control of silver and gold nanoparticles is achieved with wet-chemical synthesis techniques that employ cationic surfactants in aqueous solutions (most often cetyltrimethylammonium bromide, CTAB). Though CTAB is known to be toxic, these protocols are beneficial because of the high yields and fine control over nanoparticle shape.[44-48] Yields up to 97% have been reported for gold nanorod synthesis (yield is considered to be number of rods/ number of particles counted by TEM)[49] and up to 2 g of gold metal in a single batch of gold nanorods (though the polydispersity of the sample is typically larger for high yield synthesis procedures).[50] Synthesis of non-spherical particles usually begins with a seed-mediated approach; for example spherical seed nanoparticles (generally sub 6 nm) can be used to create both silver and gold nanorods, cubes, spheroids, and nanowires of varying size and aspect ratio using CTAB.[50] Post-synthesis purification and later surface modification affords more biocompatible nanoparticles by removing excess CTAB and coats the remaining surface chemistries or replaces it.[51-53] Gold nanorods can also be synthesized in organic solutions (toluene); however, nanorod yields are extremely low, and the size-distributions produced are extremely polydisperse making surface modification of aqueous dispersions more advantageous.[54]

Nanoparticle Processing

As mentioned previously, the synthesis of gold and silver nanoparticles often requires toxic surfactants and excess stabilizing ligands to afford control over size, size-distribution, and shape.[37, 40, 55, 56] Moreover, improvement of the nanoparticle size-distribution is generally desirable for application. Hence, post-synthesis processing which facilitates both purification and fractionation steps is often necessary.

Aqueous dispersions of metallic nanoparticles can be fractionated and purified by recursive centrifugation steps or by chromatography.[57] Once precipitated, the nanoparticles can be redispersed in fresh solvent (water). This precipitation process can be enhanced by adding salts or polar water-miscible solvents (ex. acetone) to the nanoparticle dispersion; however, both centrifugation and non-aqueous solvent addition often induces aggregation for most sugar stabilized nanoparticles when the dispersion becomes concentrated.[57] Novak et al. showed that by selecting a stabilizing ligand with a bonding strength greater than citrate and less than a thiol, or adding a buffer surfactant (ex. sodium dodecyl sulfate, SDS) afforded more desirable purification results both for centrifugation and size-exclusion chromatography.[57]

Hydrophobically stabilized metallic nanoparticles can also be purified and fractionated by recursive centrifugation steps or chromatography. However, in practice the liquid-liquid solvent/anti-solvent system combined with centrifugation is most commonly employed to size-selectively precipitate the nanoparticles. For example, toluene/ethanol and chloroform/ethanol are liquid solvent pairs often used for the fractionation of gold and silver nanoparticles.[32, 37] Increasing the anti-solvent composition

in solution weakens the solvent strength for the hydrophobic stabilizing ligands which induces nanoparticle precipitation.[32] This process is the most widely used due to its simplicity, however it leads to large quantities of mixed organic solvent waste and can become quite expensive—to purify 214 mg of gold nanoparticles synthesized from the Brust method requires ~800 mL of ethanol, in addition to time intensive centrifugation which is not easily scalable.

Recent advances in nanoparticle processing have demonstrated that carbon dioxide is an effective anti-solvent for hydrophobically stabilized nanoparticles, similar to ethanol in the liquid-liquid system. Dissolving CO_2 into an organic solvent (for example toluene, cyclohexane, hexane, or pentane) changes the properties of the solvent. These properties are dependent upon the molar composition of CO_2—and hence pressure.[58] As CO_2 dissolves into an organic solvent (performed by applying pressurized CO_2 into the headspace above solvent within a pressure cell), the liquid volume also increases—effectively creating a pressure tunable gas-expanded liquid (GXL).[58]

Mcleod et al. demonstrated the facile fractionation of a polydisperse sample of dodecanethiol modified silver nanoparticles using CO_2-expanded hexane.[38] Here a rod-shaped Archimedes screw design (fabricated of glass—see Figure 1.1) enabled the size-selective fractionation of nanoparticles at CO_2 pressures between 500 and 600 psi. A small aliquot of nanoparticle dispersion (traditionally hexane has been used for the organic solvent) is placed in the first rung of the glass spiral rod, and subsequently the rod is placed into a stainless steel pressure cell.[38] When CO_2 pressure is added, the CO_2 mole fraction within the liquid solvent increases, and induces size-selective nanoparticle

precipitation.[28] The largest nanoparticles precipitate out of solution due to their larger van der Waals attractive forces.[28] Once the first fraction of nanoparticles has been precipitated, the glass rod can be rotated moving the remaining dispersed nanoparticles further up the rod into the next rung. Utilizing pressure increments of 25 to 50 psi with each turn of the glass rod was shown to facilitate progressive size-selective nanoparticle fractionation.[38] Since the work performed by Mcleod et al., alkanethiol modified silver,[59, 60] gold,[55, 59] platinum,[61] and CdSe/ZnS[62] nanoparticles have all been processed using GXLs (either fractionation or isolation)—though the sample volumes have been generally limited to ~100 to 200 μL. Scale-up of the GXL fractionation technique was recently demonstrated by Saunders et al., who built a new fractionation apparatus capable of isolating samples volumes up to ~20 mL (mg quantities of metal).[56]

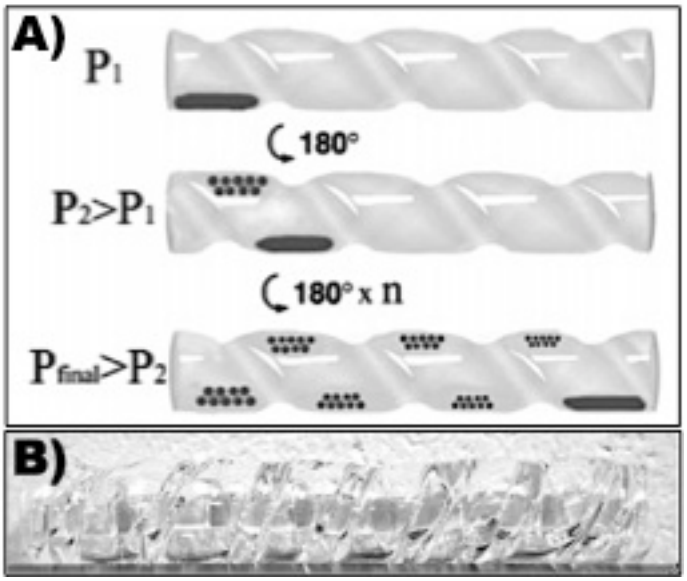

Figure 1.1: A) Schematic and B) image of glass cylindrical rod used to size-selectively fractionate metal nanoparticle dispersions. Image A is comes from Mcleod et al. *Nano Lett*., **2005**, *5* (3), pp 461–465

The recent advances in nanoparticle processing which employ GXLs is noteworthy because it essentially eliminates mixed organic solvent waste,[40] enables solvent recycle (both carbon dioxide and organic solvent),[40] and is useful for depositing nanoparticles into wide-area networks (ideal for thin film applications, deterring MEMS device stiction[36, 39] infusing nanoparticles into porous substrates for applications in catalysis or membranes),[63] and critical point drying where the solvent can be removed without going through a phase transition preserving nanoscale structure[40, 64] (analogous to supercritical drying of aerogels which minimizes detrimental capillary forces during the drying process).[65]

Dissertation Outline

As mentioned previously, current interaction energy models overpredict nanoparticle dispersibility because of assumptions made regarding ligand structure and solvation at predetermined solvent compositions. Hence, a primary objective of this dissertation aims to provide experimental measurements of the ligand structure and solvation at varying solvent conditions (during anti-solvent induced nanoparticle precipitation) which will aid in the development of more accurate and robust models to predict nanoparticle behavior.

In Chapter 2, we employ small-angle neutron scattering (SANS) to determine the ligand length and solvation for gold nanoparticles in both toluene and hexane with varying ethanol anti-solvent compositions. SANS was used because it is the only characterization technique that we are aware of which can provide non-destructive, in-situ measurements of nanoparticle ligand structure and solvation, as a result of sub

nanometer resolution and contrast matching which enables structural and compositional distinction between hydrogenated and deuterated species. These solvent pairs were selected because they are most commonly used in liquid-liquid nanoparticle processing procedures. During this investigation, we examined the role of chain length, surface coverage, and nanoparticle curvature on ligand structure, solvation, nanoparticle dispersibility, and then correlated the solvent composition induced changes to Flory-Huggins interaction parameters.

Due to the recent and numerous advantages previously demonstrated for GXL nanoparticle processing, compared to traditional liquid-liquid techniques, we again employed SANS to investigate ligand structure, solvation, and dispersibility of dodecanethiol stabilized gas-expanded hexane in Chapter 3. Here, four previously fractionated dispersions were studied at CO_2 mole fractions up to 60%. The dispersions varied in dodecanethiol surface coverage and surface curvature.

In Chapter 4, we extend the GXL fractionation process to non-spherical gold nanoparticles—more explicitly gold nanorods. Surface modification of CTAB capped gold nanorods afforded resuspension in various organic solvents which enabled a mechanistic investigation of their dispersibility in gas-expanded cyclohexane, toluene, and hexane. We also explored the impact of varying chain length (12 carbons and 18 carbons ligands) on nanorod dispersibility. Here we also present the first ever gold nanorod fractionation using the GXLs technique.

In Chapter 5, we present the facile and green synthesis of silver nanoparticles using extract from *Allium sativum*, known commonly as garlic. The intent was to create

stable silver nanoparticles which may be useful in the biomedical field as a result of compatibility with biological media and that have high oxidation resistance. We investigate various synthesis procedures, by varying the garlic extract quantity (the reducing and stabilizing agents), and temperature.

In Chapter 6, a biomedical application of gold nanoparticles is investigated. Here hybrid vesicle-nanoparticle systems are evaluated using SANS to determine the effect of nanoparticle loading concentration, temperature, and lipid content to better understand lipid ordering as measured by changes in the membrane thickness. This work was performed in collaboration with Dr. Geoffrey Bothun at the University of Rhode Island and his former graduate student Dr. Yanjing Chen.

Lastly, in Chapter 7, the conclusions of this dissertation and recommendations for future work are made. In addition, the most important finding of this work is described—the solvent composition dependent ligand length and solvation of hydrophobically stabilized nanoparticles, as measured by SANS.

References

(1) Feynman, R. P. There's Plenty of Room at the Bottom. *http://www.zyvex.com/nanotech/feynman.html* (accessed October 25, 2010).

(2) Daniel, M.; Astruc, D. *Chem. Rev.* **2004** *104* 293-346.

(3) van Albada, G. A.; Schreck, J. O. *J. Chem. Educ.* **1987** *64* 869-null.

(4) Bhattacharya, R.; Patra, C. R.; Earl, A.; Wang, S.; Katarya, A.; Lu, L.; Kizhakkedathu, J. N.; Yaszemski, M. J.; Greipp, P. R.; Mukhopadhyay, D.; Mukherjee, P. *Nanomed. Nanotechnol. Biol. Med* **2007** *3* 224-38.

(5) Lin, M.; Zhao, B.; Chen, Y. *Ind. Eng. Chem. Res.* **2009** *48* 7037-7043.

(6) Zhao, B.; Chen, Y. *J. Non Cryst. Solids* **2010** *356* 839-847.

(7) Manno, D.; Filippo, E.; Di Giulio, M.; Serra, A. *J. Non Cryst. Solids* **2008** *354* 5515-20.

(8) Kim, Y. J.; Yang Y. S.; Ha S.; Cho, S. M.; Kim Y. S.; Kim H. Y.; Yang, H.; Kim Y. T. *Sensor. Actuat. B-Chem.* **2005** *106* 189-98.

(9) Rotello, V. M., Ed.; *Nanoparticles: Building Blocks for Nanotechnology:* Rotello, V. M., Ed.; Nanostructure Science and Technology; Kluwer Academic/Plenum Publishers: New York, NY, 2004; .

(10) Murphy, C. J.; Sau, T. K.; Gole, A. M.; Orendorff, C. J.; Gao, J.; Gou, L.; Hunyadi, S. E.; Li, T. *J. Phys. Chem. B* **2005** *109* 13857-70.

(11) Jena, B. K.; Retna, C. R. *Anal. Chem.* **2008** *80* 4836-4844.

(12) Dickerson, E. B.; Dreaden, E. C.; Huang, X.; El-Sayed, I. H.; Chu, H.; Pushpanketh, S.; McDonald, J. F.; El-Sayed, M. A. *Cancer Lett.* **2008** *269* 57-66.

(13) LaLonde, A. D.; Grant Norton, M.; Zhang, D.; Ganadean, D.; Alkhateeb, A.; Padmanabhan, R.; McIlroy, D. N. *J. Mater. Res.* **2005** *20* 3021-7.

(14) Dhawan, A.; Gerhold, M.; Marinakos, S.; Leonard, D.; Wang, H.; Chilkoti, A.; Russell, P.; Vo-Dinh, T. In *In Fabrication of fiber-optic sensors based on plasmon resonances of metallic nanostructures;* Sensor, Actuators, and Microsystems General Session - 212th ECS Meeting; Electrochemical Society Inc: Pennington, NJ 08534-2896, United States, 2008; Vol. 11, pp 41-55.

(15) Storhoff, J. J.; Elghanian, R.; Mucic, R. C.; Mirkin, C. A.; Letsinger, R. L. *J. Am. Chem. Soc.* **1998** *120* 1959-1964.

(16) Nath, N.; Chilkoti, A. *Anal. Chem.* **2002** *74* 504-509.

(17) Geng, D.; Lu, G. *J. Nanopart. Res.* **2007** *9* 1145-1151.

(18) Achermann, M. *J. Phys. Chem. Lett.* **2010** *1* 2837-2843.

(19) Ding, H.; Yong, K.; Roy, I.; Pudavar, H. E.; Law, W. C.; Bergey, E. J.; Prasad, P. N. *J. Phys. Chem. C* **2007** *111* 12552-12557.

(20) Park, S.; Oh, S.; Mun, J.; Han, S. *Colloids Surf. , B* **2006** *48* 112-118.

(21) Bothun, G. D. *J. Nanobiotech.* **2008** *6* .

(22) Rasch, M. R.; Rossinyol, E.; Hueso, J. L.; Goodfellow, B. W.; Arbiol, J.; Korgel, B. A. *Nano Lett.* **2010** *10* 3733-3739.

(23) Didychuk, C. L.; Ephrat, P.; Chamson-Reig, A.; Jacques, S. L.; Carson, J. J. L. *Nanotechnology* **2009** *20* 195102 (9 pp.).

(24) Khlebtsov, B. N.; Zharov, V. P.; Melnikov, A. G.; Tuchin, V. V.; Khlebtsov, N. G. In *In Optimization of gold nanostructers for laser killing of cancer cells;* Saratov Fall Meeting 2005: Coherent Optics of Ordered and Random Media VI, September 27, 2005 - September 30; SPIE: Saratov, Russia, 2006; Vol. 6164, pp Russian Foundation for Basic Research, Russia; SPIE Russia Chapter; Saratov State University SPIE Student Chapter, Russia; CRDF.

(25) Shrivastava, S.; Bera, T.; Roy, A.; Singh, G.; Ramachandrarao, P.; Dash, D. *Nanotechnol.* **2007** *18* 9.

(26) Kvitek, L.; Pancek, A.; Soukupova, J.; Kolar, M.; Vecerova, R.; Prucek, R.; Holecova, M.; Zboril, R. *J. Phys. Chem. C* **2008** *112* 5825-34.

(27) Marambio-Jones, C.; Hoek, E. *J. Nanopart. Res.* **2010**, *12*, 1531-1551.

(28) Anand, M.; You, S.; Hurst, K. M.; Saunders, S. R.; Kitchens, C. L.; Ashurst, W. R.; Roberts, C. B. *Ind. Eng. Chem. Res.* **2008** *47* 553-559.

(29) Kitchens, C. L.; McLeod, M. C.; Roberts, C. B. *J Phys Chem B* **2003** *107* 11331-11338.

(30) Turkevich, J.; Stevenson, P. C.; Hillier, J. *Discuss. Faraday Soc.* **1951** *11* 55-75.

(31) Kimling, J.; Maier, M.; Okenve, B.; Kotaidis, V.; Ballot, H.; Plech, A. *J. Phys. Chem. B* **2006** *110* 15700-15707.

(32) Brust, M.; Walker, M.; Bethell, D.; Schiffrin, D. J.; Whyman, R. *J. Chem. Soc. - Chem. Commun.* **1994** 801-802.

(33) Jana, N. R.; Gearheart, L.; Murphy, C. J. *Langmuir* **2001** *17* 6782-6.

(34) Jana, N. R.; Gearheart, L.; Murphy, C. J. *J. Phys. Chem. B* **2001** *105* 4065-7.

(35) Shukla, R.; Nune, S. K.; Chanda, N.; Katti, K.; Mekapothula, S.; Kulkarni, R. R.; Welshons, W. V.; Kannan, R.; Katti, K. V. *Small* **2008** *4* 1425-36.

(36) Liu, J.; Anand, M.; Roberts, C. B. *Langmuir* **2006** *22* 3964-3971.

(37) Korgel, B. A.; Fullam, S.; Connolly, S.; Fitzmaurice, D. *J Phys Chem B* **1998** *102* 8379-88.

(38) McLeod, M. C.; Anand, M.; Kitchens, C. L.; Roberts, C. B. *Nano Lett.* **2005** *5* 461-5.

(39) McLeod, M. C.; Kitchens, C. L.; Roberts, C. B. *Langmuir* **2005** *21* 2414-2418.

(40) Kitchens, C. L.; Roberts, C. B.; Juncheng, L.; Robert, A. W.; Madhu, A.; Von, W. G.; Hurst, K. M.; Saunders, S. R. In *Application of Gas-Expanded Liquids for Nanoparticle Processing: Experiment and Theory;* Gas-Expanded Liquids and Near-Critical Media; American Chemical Society: Washington, DC, 2009; pp 290-308.

(41) Tan, J.; Liu, R.; Wang, W.; Liu, W.; Tian, Y.; Wu, M.; Huang, Y. *Langmuir* **2010** *26* 2093-2098.

(42) Mehta, S. K.; Chaudhary, S.; Gradzielski, M. *J. Colloid Interface Sci.* **2010** *343* 447-453.

(43) Philip, D. *Spectrochim. Acta, Part A* **2009** *73* 650-653.

(44) Sook, Y. M.; Kusunose, T.; Sekino, T. *Mater Lett* **2009** *63* 2038-40.

(45) Smith, D. K.; Korgel, B. A. *Langmuir* **2008** *24* 644-649.

(46) Chen, X.; Sui, Z. M.; Wang, L. Y.; Xu, L. M.; Zhuang, W. C.; Chai, Y. C.; Yang, C. J. *Physica E* **2006** *33* 308-14.

(47) Pileni, M. P.; Jiang, X. C. *Colloids Surf. , A* **2007** *295* 228-32.

(48) Nikoobakht, B.; El-Sayed, M. *Chem. Mater.* **2003** *15* 1957-1962.

(49) Sau, T. K.; Murphy, C. J. *Langmuir* **2004** *20* 6414-6420.

(50) Jana, N. R. *Small* **2005** *1* 875-82.

(51) Boca, S. C.; Astilean, S. *Nanotechnol.* **2010** *21* 235601 (8 pp.).

(52) Pastoriza-Santos, I.; Perez-Juste, J.; Liz-Marzan, L. M. *Chem. Mater.* **2006** *18* 2465-2467.

(53) Mitamura, K.; Imae, T.; Saito, N.; Takai, O. *J. Phys. Chem. B* **2007** *111* 8891-8898.

(54) Chandran, S. P.; Pasricha, R.; Bhatta, U. M.; Satyam, P. V.; Sastry, M. **2007** *7* 2808-2817.

(55) McLeod, M. C.; Anand, M.; Kitchens, C. L.; Roberts, C. B. **2005** *5* 461-465.

(56) Saunders, S. R.; Roberts, C. B. *Nanotechnol.* **2009** *20* .

(57) Novak, J. P.; Nickerson, C.; Franzen, S.; Feldheim, D. L. *Anal. Chem.* **2001** *73* 5758-5761.

(58) Jessop, P. G.; Subramaniam, B. *Chem. Rev.* **2007** *107* 2666-2694.

(59) Anand, M.; McLeod, M. C.; Bell, P. W.; Roberts, C. B. *J Phys Chem B* **2005** *109* 22852-22859.

(60) McLeod, M. C.; Kitchens, C. L.; Roberts, C. B. *Langmuir* **2005** *21* 2414-2418.

(61) Liu, J.; Sutton, J.; Roberts, C. B. *J. Phys. Chem. C* **2007** *111* 11566-11576.

(62) Anand, M.; Odom, L. A.; Roberts, C. B. *Langmuir* **2007** *23* 7338-7343.

(63) Gupta, G.; Shah, P. S.; Zhang, X.; Saunders, A. E.; Korgel, B. A.; Johnston, K. P. **2005** *17* 6728-6738.

(64) Hurst, K. M.; Roberts, C. B.; Ashurst, W. R. *Nanotechnol.* **2009** *20* 185303 (9 pp.).

(65) Reichenauer, G., Ed.; *Aerogels:*Kirk-Othmer Encyclopedia of Chemical Technology; John Wiley & Sons, Inc.: 2000; Vol. 1-30.

CHAPTER TWO

SANS INVESTIGATION OF GOLD NANOPARTICLE CLUSTERING AND LIGAND STRUCTURE UNDER ANTI-SOLVENT CONDITIONS

Introduction

Engineered nanomaterials of varying elemental composition, surface chemistry, size,[1] and shape[2] have found enormous potential for use in biomedical applications,[3-5] catalysis,[6] and sensing devices.[7] In particular, the unique size-dependent properties of metal nanoparticles (silver and gold) include plasmon resonance,[8, 9] catalytic properties,[6] as well as photo-thermal activity.[4] A significant benefit of solution based nanoparticle synthesis is the ability to control the size, shape,[10] and aspect ratio[11] of the nanoparticles by varying the temperature[12] and concentration of different surfactants, ligands, and other structure directing agents.[11] Most applications require monodisperse populations of nanoparticles that are free of excess surfactant or ligand. Thus post-synthesis processing is critical to remove any reaction byproducts and excess ligands or surfactants from solution that may be detrimental to the nanoparticle application. Typically, anti-solvent precipitation is used for nanoparticle purification, size or shape fractionation, and deposition.[13] Common liquid-liquid solvent/anti-solvent pairs that enable this nanoparticle size-selective precipitation and isolation include ethanol/toluene and ethanol/hexane for alkanethiol modified nanoparticles, including hydrophobic gold nanoparticles (GNPs).[14] Once precipitated, the nanoparticles can be redispersed in neat solvent, free from excess ligands and surfactants.

Small-angle scattering can provide detailed information on nanoparticle size and particle interactions in solution. Structural information is obtained from scattering data, and in general, dilute concentrations of particles are assumed to be non-interacting requiring only a form factor for size/shape determination. Saunders et al. used small-angle x-ray scattering (SAXS) to study dilute dispersions (~3 mg/mL) of dodecanethiol modified GNPs in toluene and found that particle-particle interactions between sub 6 nm core-diameter particles are sufficiently large and require the incorporation of a structure factor (in addition to a form factor) for accurate data fitting.[15] This study also stated that extremely dilute concentrations of GNPs (much less than 3 mg/mL) scattered x-rays similar to individual randomly dispersed particles, and proved to be non-interacting (structure factor assumed to be unity). Saunders also reported 30 to 60% ligand surface coverage values for dodecanethiol on the surface of GNPs for core diameters between ~1 nm to ~6 nm. Both particle interactions and ligand surface coverage values are critical in developing models which predict nanoparticle dispersibility. Similar to SAXS, small-angle neutron scattering (SANS) can also be used to obtain the structural information of nanoparticles. However, because neutrons scatter as a function of atomic composition and density (different than x-rays), detailed structural (e.g. ligand length) and compositional information can be obtained through selective deuteration and scattering length density (SLD) contrast enhancement. Ligand shell solvation can be determined from the measured ligand shell SLD (SLD_{shell}),[16] which receives contribution from the hydrogenated alkanethiol ligand SLD (SLD_{thiol}) and the deuterated solvent SLD (SLD_{solv}) which has penetrated into the ligand shell. The ligand shell thickness is also determined

using SANS. This investigation demonstrates in-situ determination of the ligand surface coverage, ligand solvation, ligand shell thickness, nanoparticle core-diameter, and particle-particle interactions using SANS as a function of the bulk anti-solvent composition for the ethanol/toluene and ethanol/hexane deuterated solvent systems.

Chapter 3 complements this work using SANS to study the ligand shell solvation and ligand length for dodecanethiol modified silver nanoparticles at varying CO_2 mole fractions in gas-expanded hexane.[16] We demonstrated that increased anti-solvent conditions (CO_2 dissolved in hexane) lowered the solvent strength of the hexane which resulted in simultaneous ligand shell collapse and decreased ligand solvation. This previous research (which will be discussed in detail later in Chapter 3) was limited to dodecanethiol stabilized silver nanoparticles dispersed in CO_2-expanded hexane; however, it demonstrated that SANS is a unique method for in-situ ligand measurements of nanoparticles, specifically ligand solvation and shell thickness. Investigation of the solvent-ligand interactions for different metal nanoparticles, varying alkane chain length, and additional solvent/anti-solvent systems is of significant importance for modeling nanoparticle interaction energies and the development of a fundamental understanding of nanoparticle dispersions.[17-19]

Interaction energy models aim to predict the maximum nanoparticle size dispersible in solution at given solvent conditions, metal type, and ligand surface coverage.[18, 20] Previous work has improved the accuracy of interaction energy models by incorporating ligand length and ligand solvation (elastic and osmotic contributions respectively); however, the maximum particle size dispersed in solution is often over

predicted.[17, 18] Development of accurate interaction energy models will lead to reduced costs and more efficient processing procedures which aim to isolate nanoparticles at predetermined conditions (size, shape, ligand length, surface coverage, and elemental composition),[17, 18, 21] the enhancement of novel techniques for nanoparticle self-assembly and deposition,[22, 23] and synthesis of nanoparticles.[19] Therefore, experimental work detailing the ligand response to solvent conditions is critical for the design of more robust and accurate interaction energy models.

In this work, we have investigated the shell thickness and solvation of alkanethiol ligands on GNPs in *n*-hexane-d_{14} and toluene-d_8 as a function of ethanol-d_6 anti-solvent composition. The octadecanethiol and dodecanethiol ligand length and solvation were found to decrease linearly as a result of increased ethanol-d_6 composition. It was found that both the length and solvation of the octadecanethiol ligands on GNPs decreased at lower ethanol-d_6 compositions compared to dodecanethiol. The combination of collapsed alkane ligands and poor solvation yields decreased nanoparticle stability and induces precipitation. The calculated Flory-Huggins interaction parameters (χ_{12}) for alkanenethiol/*n*-hexane-d_{14} were shown to be lower than in toluene-d_8 at solvent mixtures of up to 50% ethanol-d_6 concentration, excluding neat solvents. Our findings for ligand solvation and shell thicknesses will impact future interaction energy models predicting nanoparticle dispersibility and also demonstrate that Flory-Huggins interaction parameter calculations are relevant for predicting general trends in nanoparticle ligand solubility. GNP clustering was observed during SANS data analysis, and is also discussed with respect to dispersibility at varying solvent conditions.

Experimental

Materials

The metal precursor hydrogen tetrachloroaurate (III) trihydrate ($HAuCl_4 \cdot 3H_2O$, 99.99%) was purchased from VWR. The stabilizing agents sodium citrate dihydrate (99%, part no. BDH0288), 1-dodecanethiol (98%) and 1-octadecanethiol (90%), and reducing agent sodium borohydride ($NaBH_4$, 98%) were purchased from VWR. ACS grade ethanol (95%), toluene (99.7%), and n-hexane (95%) were purchased by VWR. *n*-hexane-d_{14} (98%), toluene-d_8 (99.5%), and ethanol-d_6 (99%) were purchased from Cambridge Isotope Laboratories. All chemicals were used without further purification.

Characterization

Transmission Electron Microscopy (TEM)

All TEM images were obtained using a Hitachi 7600 with a 120 kV accelerating voltage. TEM samples were prepared by drop casting ~5 μL of nanoparticle dispersion onto a 300 mesh formvar carbon coated copper TEM grid (Ted Pella), followed by solvent evaporation. The size distributions were obtained by image analysis performed with the ImageJ software package[24] counting at least 1500 particles for meaningful and relevant statistics.

Small Angle Neutron Scattering (SANS)

SANS experiments were performed on the NG7 30 meter SANS instrument at NIST Center for Neutron Research (NCNR, Gaithersburg, MD).[25] All samples had a volume fraction of $\varphi \sim 1\%$, and were considered dilute. The low concentration of the GNP dispersions was desired in order to minimize interparticle interactions and the need

for a structure factor in the scattering analysis. Each sample was loaded into a 2 mm path length titanium demountable cell and measured at 25 °C. Three sample-to-detector distances were used (1 m, 4.5 m, and 13.5 m) to obtain a q range from 0.004 to 0.5 $Å^{-1}$ with a neutron wavelength of $\lambda = 6$ Å and a resolution of $\Delta\lambda/\lambda$ equal to 12% (FWHM). Empty beam background, empty cell background, neat solvent (toluene-*d8* or *n*-hexane-*d14*) backgrounds, detector sensitivity, sample transmission, and sample thickness were considered during raw data reduction. The neat solvent and empty cell background measurements were used to normalize all SANS data. The reduced scattering intensities, I(q), were fit as a function of the scattering vector, q(θ). Here, $q(\theta) = 4\pi\sin(\theta)/\lambda$ and θ is defined as the scattering angle. All SANS fitting was performed using Igor Pro 6.03 software and models provided by NIST.[26]

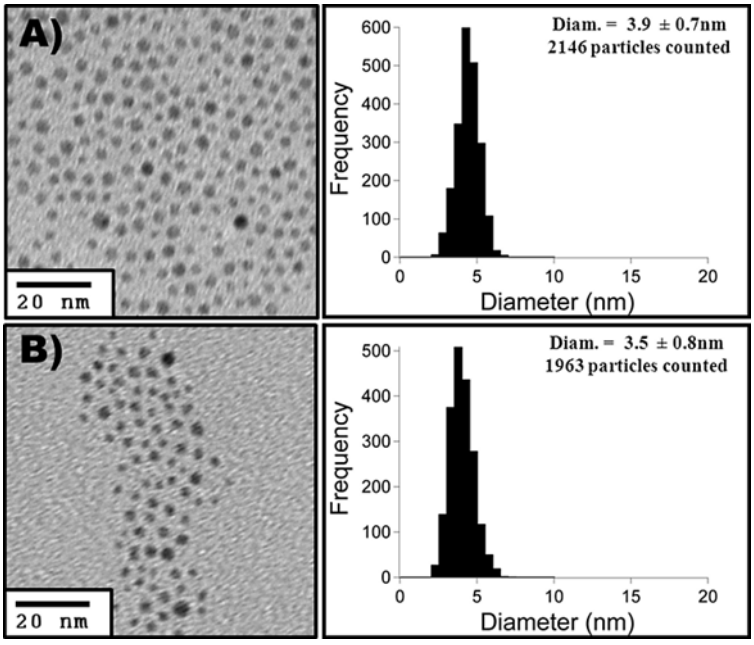

Figure 2.1: TEM image and histogram of A) dodecanethiol and B) octadecanethiol capped gold nanoparticles. All nanoparticles were sized using ImageJ software.

The SANS spectra were fit for all nanoparticles in the ~0.04 to ~0.5 $Å^{-1}$ q range using a polydisperse core-shell model according to Bartlett et al.[27] to determine the SLD_{shell} and shell thickness of the alkanethiol stabilizing ligands. The scattering intensity, I(q), is a function of both the volume fraction of the GNPs in solution (ϕ) and the form factor P(q). For dilute concentrations, the structure factor is assumed to be unity, S(q) = 1. The scattering intensity is fit as a function of the mean particle size (radius), polydispersity (Schulz distribution), average shell thickness, and component scattering length densities (SLD_{core}, SLD_{shell}, SLD_{solv}). The resulting form factor is normalized by the calculated mean GNP volume. The volume fraction, SLD_{core} (4.5×10^{-6} $Å^{-1}$), nanoparticle diameter/polydispersity (determined by TEM, see Figure 2.1), and SLD_{solv} were held constant during all SANS fitting, while the shell thickness and SLD_{shell} were used as adjustable parameters (See Figure 2.2A). For a more in depth discussion of the SANS models, see Appendix A.

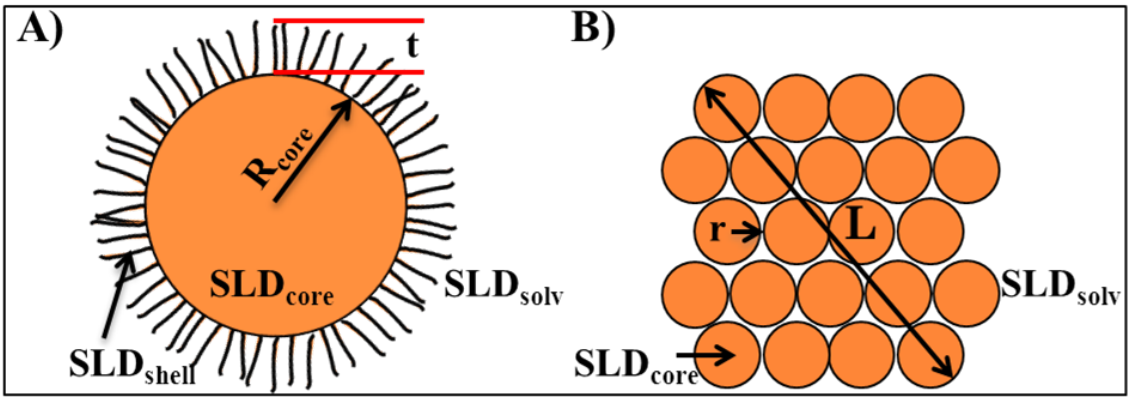

Figure 2.2: Schematic of the A) polydisperse core-shell model and B) fractal model. Adjustable parameters include the nanoparticle size, $R_{core;}$ scattering length density (SLD) of the nanoparticle core, ligand shell and bulk solvent; repeat block radius, r; and correlation length.

SANS spectra for the dodecanethiol and octadecanethiol modified GNPs dispersed in toluene-d_8 with varying ethanol-d_6 concentration were fit on the ~0.004 to 0.2 $Å^{-1}$ q range with a fractal model (see Teixeira et al.)[28] because cluster formation was evident from the scattering data, despite the dilute concentrations. The fractal model assumes that scattering occurs from fractal like clusters of GNPs dispersed in solution. The adjustable parameters used to fit the SANS spectra include the correlation length in solution, radius of the GNPs which make up the clusters, and the fractal dimension (see Figure 2.2B). The SLD_{solv}, SLD_{core}, and volume fraction were held constant during fractal model data fitting to pre-determined values.

Solvent and Ligand Properties

Deuterated solvents were used in all SANS experiments to provide contrast between the hydrogenated ligand tails and the bulk solvent. The molar compositions and densities of the ethanol-d_6/*n*-hexane-d_{14} and ethanol-d_6/toluene-d_8 mixtures were calculated assuming ideal mixing and the following neat solvent densities (0.943 g/cm^3, 0.767 g/cm^3, and 0.910 g/cm^3 for toluene-d_8, *n*-hexane-d_{14}, and ethanol-d_6 respectively). The SLD values were calculated for the liquid solvent mixtures and the GNP core using the NIST NCNR SLD calculator.[29] The SLD_{solv} values were determined to be 5.66 x 10^{-6} $Å^{-2}$, 6.14 x 10^{-6} $Å^{-2}$, and 6.22 x 10^{-6} $Å^{-2}$ for toluene-d_8, *n*-hexane-d_{14}, and ethanol-d_6 respectively. The SLD_{thiol} for dodecanethiol and octadecanethiol were calculated to be -3.67 x 10^{-7} $Å^{-2}$ and -3.49 x 10^{-7} $Å^{-2}$ respectively. Tables 2.1 - 2.2 show the calculated values for the molar compositions, densities, and SLD_{solv} as a function of ethanol-d_6 mole

fraction. The calculated values for the SLD_{solv} were used during all SANS fitting as accurate data analysis of the SLD_{shell}, shell thickness, cluster size, and repeat block diameter are dependent upon these values.

Table 2.1: Solvent properties for the mixed *n*-hexane-d_{14}/ethanol-d_6 solvent including scattering length density (SLD)

ethanol (mol. frac.)	density (g/cm^3)	SLD_{solv} (Å^{-2})
0.000	0.767	6.14E-06
0.202	0.796	6.26E-06
0.363	0.819	6.34E-06
0.495	0.838	6.38E-06
0.603	0.853	6.39E-06
0.695	0.866	6.38E-06

Table 2.2: Solvent properties for the mixed toluene-d_8/ ethanol-d_6 solvent including scattering length density (SLD)

ethanol (mol. frac.)	density (g/cm^3)	SLD_{solv} (Å^{-2})
0.000	0.943	5.66E-06
0.171	0.937	5.70E-06
0.317	0.933	5.75E-06
0.443	0.928	5.80E-06
0.553	0.925	5.85E-06
0.650	0.922	5.91E-06

Gold Nanoparticle Synthesis and Surface Modification

Citrate stabilized gold nanoparticles (GNPs) were prepared by a modified procedure similar to Jana et al.[30] yielding ~4 nm diameter particles. In short, 30 mL of citrate solution (0.05 M) was added to 567 mL of DI water in a 1 L volumetric flask. Next, 3 mL of 0.05M $HAuCl_4$ was added to the mixture and reduced with 3 mL sodium borohydride (0.05 M). The resulting aqueous dispersed GNPs were ruby red in color.

The surface modification of gold nanoparticles is well known and has been characterized extensively.[31, 32] Similar to a procedure performed by Jana et al., where GNPs originally stabilized by citrate are made hydrophobic with dodecanethiol,[34] we resuspended GNPs in toluene by surface modification using either dodecanethiol or octadecanethiol. Briefly, between 100 to 300 mL of 0.01 M dodecanethiol or octadecanethiol solutions in toluene were added to the 600 mL aqueous GNP dispersion in a volumetric flask. The biphasic mixture was vigorously shaken until the GNPs transferred from the aqueous phase to the toluene phase. Smaller ratios of toluene/aqueous (1:6) solution were found to yield incomplete phase transfers of the GNPs and particle aggregation. The biphasic mixture was placed in a 1 L separatory funnel, where the toluene dispersed GNPs were isolated from the aqueous phase. Next, ethanol was added to the GNPs (4:1 ethanol to GNP dispersion by volume) followed by centrifugation at 14,500 rpms for 10 min to induce nanoparticle precipitation. The supernatant liquid, containing excess stabilizing ligands and organic solvent was decanted. The GNPs were resuspended in 20 mL neat solvent (hexane or toluene) followed by 5 min of sonication. The purification procedure was performed a total of three times before use.

Purified GNPs stabilized by dodecanethiol were selectively size-fractionated by combining ethanol anti-solvent precipitation with centrifugation. In short, the toluene dispersed GNPs were diluted to 50% ethanol by volume, followed by centrifugation at 14,500 rpms for 10 min. The supernatant (containing GNPs) was collected and then diluted to a final ethanol composition of 55% by volume. Centrifugation was repeated at

14,500 rpms for 10 min and the supernatant was decanted. The precipitated GNPs were resuspended in fresh toluene followed by sonication for 5 min. The resulting size distribution was 3.9 ± 0.7 nm diameter for the dodecanethiol modified GNPs. Similarly, octadecanethiol stabilized GNPs were purified and then isolated between 40 and 45% ethanol volume fractions in toluene and were measured to be 3.5 ± 0.7 nm in diameter. The same procedure was performed for dodecanethiol and octadecanethiol modified GNPs in hexane resulting in the same size GNPs as fractionated in the toluene/ethanol solvent mixture (50 to 55% and 40 to 45% ethanol by volume for dodecanethiol and octadecanethiol modified GNPs respectively). The fractionated nanoparticles were dried to a thin film and redispersed in toluene-d_8 or *n*-hexane-d_{14} to achieve concentrations ~1% by volume. The final stable dispersions were simultaneously vortex mixed and sonicated for 5 min prior to use. Figure 2.1 shows TEM images for both the dodecanethiol and octadecanethiol stabilized GNPs with their respective histograms.

Results and Discussion

SANS Data Analysis

As described previously, the SANS spectra were fit with a polydisperse core-shell model[27] to determine ligand thickness and solvation. Figure 2.3 shows fit SANS data for A) dodecanethiol and B) octadecanethiol stabilized GNPs dispersed in toluene-d_8 as a function of varying ethanol-d_6 volume fraction. The variation in scattering intensity is due to changes in ligand structure and solvation, as well as SLD contrast between the solvent and GNPs/ligands. In Figure 2.3A, decreased scattering intensity is evident for

dodecanethiol stabilized GNPs in 50% ethanol-d_6/toluene-d_8 at low q. The lower scattering intensity is due to nanoparticle precipitation, consistent with previous isolation between 50 and 55% ethanol volume fraction. Decreased scattering intensity induced by increased ethanol-d_6 concentration is also observed in Figure 2.3B for octadecanethiol stabilized GNPs dispersed in toluene-d_8. The SANS spectra for the dodecanethiol stabilized GNPs dispersed in *n*-hexane-d_{14} are similar to that of the GNPs dispersed in toluene-d_8 and are omitted for brevity.

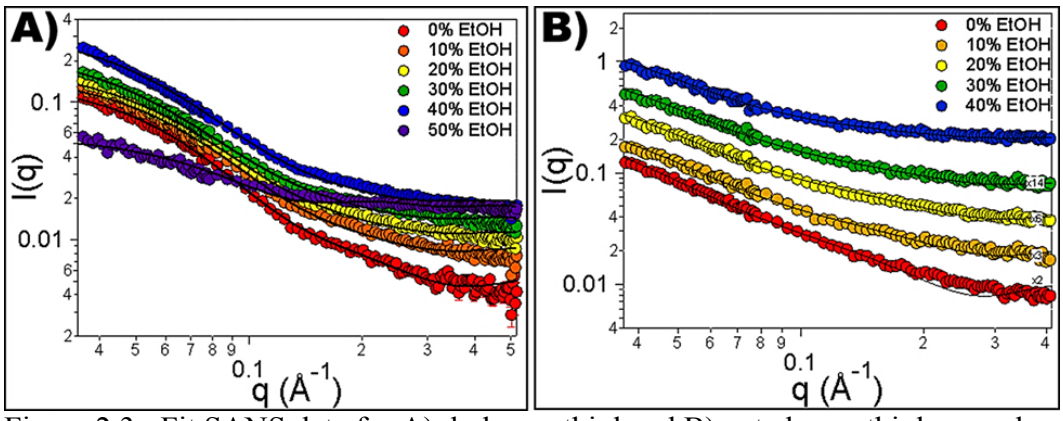

Figure 2.3: Fit SANS data for A) dodecanethiol and B) octadecanethiol capped gold nanoparticles dispersed in toluene-d_8 with varying ethanol-d_6 composition fit using a polydisperse core-shell model. Some of the scattering spectra have been offset for clarity.

Ligand Solvation Response to Ethanol Anti-Solvent and Determination of Surface Coverage

The mole fraction of solvent within the ligand shell can be calculated from the SLD_{shell}, SLD_{solv}, and SLD_{thiol} values obtained during SANS data analysis. Equation 2.1 calculates the percent ligand solvation, which accounts for the percent of the ligand shell which is occupied by solvent molecules, assuming the composition of the solvent within the shell is equal to the bulk. This equation has been previously used by Butter et al. to

determine the ligand solvation for oleic acid modified magnetic iron nanoparticles and White et al. for dodecanethiol stabilized silver nanoparticles as a function of CO_2 mole fraction in CO_2-expanded hexane.[16, 35]

$$\%\ Ligand\ Solvation = \frac{SLD_{Shell} - SLD_{thiol}}{SLD_{Solv} - SLD_{thiol}} \text{x} 100\% \qquad \textbf{(2.1)}$$

Figure 2.3 shows the fit SLD_{shell} and calculated ligand solvation values plotted as a function of ethanol-d_6 volume fraction in *n*-hexane-d_{14} and toluene-d_8. The ligand solvation values presented here are calculated averages for the entire length of the alkane chain. Dodecanethiol solvation was calculated to be 26% and 17% in neat *n*-hexane-d_{14} and toluene-d_8, respectively (Figure 2.4A). Comparatively, octadecanethiol solvation was calculated to be 18% and 20% in neat *n*-hexane-d_{14} and toluene-d_8, respectively (Figure 2.4B). As the ethanol-d_6 bulk solvent composition increases, the SLD_{shell} decreases linearly, indicating that the ligand shell composition is transitioning from a deuterated species to a hydrogenated species; i.e. scattering occurs primarily from the alkanethiol ligands rather than solvated ligands. The SLD_{shell} decreases to negative values similar to the SLD_{thiol} at ethanol-d_6 compositions nearing 40% - 50% by volume (the lower isolation solvent conditions for octadecanethiol and dodecanethiol modified GNPs, respectively). At 50% ethanol-d_6 composition, the SLD_{shell} values for dodecanethiol correspond to 4% solvation in *n*-hexane-d_{14} and nearly 0% in toluene-d_8. At 40% ethanol-d_6 composition, octadecanethiol solvation is nearly 0% for both *n*-hexane-d_{14} and toluene-d_8. These results demonstrate that poor ligand solvation contributes to complete ligand collapse and nanoparticle precipitation. However, ligand

solvation is also a function of ligand chain length, nanoparticle curvature, and surface coverage.

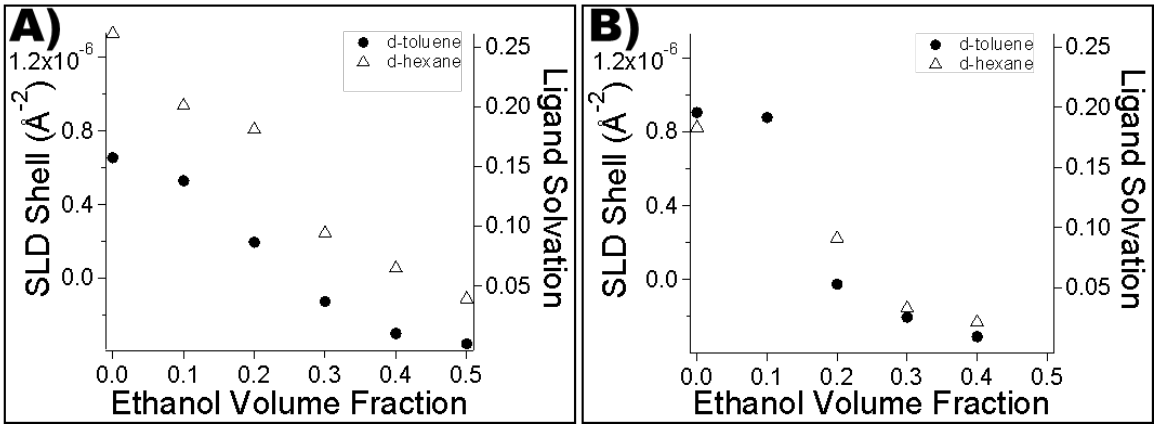

Figure 2.4: The shell scattering length density (SLD_{shell}) and ligand solvation plotted as a function ethanol-d_6 volume fraction for A) dodecanethiol and B) octadecanethiol stabilized gold nanoparticles dispersed in toluene-d_8 and *n*-hexane-d_{14}.

Saunders et al.[15] used SAXS to calculate the ligand surface coverage of dodecanethiol to be ~30 to 60% on 1 to 6 nm diameter GNPs, respectively based on geometrical constraints. The analysis by Saunders et al. incorporated the nanoparticle radius, ligand length (assumed to be 15 Å), ligand cross sectional area (14.5 Å^2), and the area of the thiol head group on the surface of the GNP SA_{thiol} (0.16 nm^2 from literature).[36] Employing these methods, the dodecanethiol and octadecanethiol surface coverage values were calculated to be 51% and 42% (we assumed octadecanethiol to be 20 Å in length), respectively and are comparable to those determined by Saunders et al.[15]

SANS is the only technique to our knowledge which can provide both ligand solvation and shell thickness measurements which affords direct surface coverage calcluations. Equation 2.2 calculates ligand surface coverage by incorporating the measured ligand length and solvation values (from SANS), Avogadro's number (N_A),

V_{molar_thiol} as the calculated molar volume of dodecanethiol (239.5 cm^3/mol) or octadecanethiol(338.3 cm^3/mol), and $r_{core+shell}$ and r_{core} the radius of the core + shell and core of the nanoparticle, respectively. The r_{core} values used in Equation 2.2 were equal to the radii measured by TEM. Using Equation 2.2, the average surface coverage of dodecanethiol on the GNPs values was determined to be 72% and 75% for both toluene-d_8 and *n*-hexane-d_{14}, respectively—hence, the average surface coverage of the two dodecanethiol GNP dispersions is 73.5%. Similarly, we calculated the average surface coverage of octadecanethiol on the GNPs to be 77% and 73% for both toluene-d_8 and *n*-hexane-d_{14}, respectively yielding an average of 75% surface coverage for both dispersions. Anand et al. measured the surface coverage of dodecanethiol on the surface of both gold and silver nanoparticles to be between 65% and 75% for particles with diameters between 5 and 7 nm in diameter, and is comparable to our calculated results.[18]

$$\%\,Surface\ Coverage = \frac{A_{head} * \frac{1}{3}(r^3{}_{core+shell} - r^3{}_{core})(100\% - \%Ligand\ Solvation)N_A}{r^2{}_{core} V_{molar\_thiol}} \quad \textbf{(2.2)}$$

Assuming the solvent-ligand interactions are similar for toluene and hexane, the ligand solvation values are expected to slightly greater in *n*-hexane-d_{14} compared to toluene-d_8 with varying ethanol-d_6 composition due to the respective SLD_{solv} values (see Tables 2.1-2.2 and Figure 2.4A). The dodecanethiol solvation was observed to be greater for the *n*-hexane-d_{14} dispersed GNPs compared to toluene-d_8 for the solvent compositions studied. Comparatively, Figure 2.4B shows that octadecanethiol solvation is similar for both toluene-d_8 and *n*-hexane-d_{14} with varying ethanol composition. These results demonstrate that ligand solvation is a function of chain length, as well as surface curvature and surface coverage—11% and 1.5% greater for octadecanethiol, respectively.

A greater degree of nanoparticle curvature (smaller core-diameter) may enable greater solvent penetration deep into the ligand shell providing the osmotic repulsive forces necessary for dispersibility.[16] Similarly, high surface coverage is ideal to prevent nanoparticle aggregation as the ligands provide steric repulsion forces preventing particle-particle attraction.[18] However, lower ligand surface coverage can afford greater solvation, as higher coverage may prevent deep solvent penetration into the ligands shell due to steric hindrances between adjacent alkyl tails.[16] The SANS results further establish that both surface coverage and surface curvature impact ligand solvation, and therefore nanoparticle dispersibility.

As mentioned earlier, the chain length also impacts the solvent-ligand interactions which provide sufficient repulsive forces preventing particle-particle attraction. Figure 2.4 shows that dodecanethiol solvation is greater for both *n*-hexane-d_{14} and toluene-d_8, compared to octadecanethiol. As the anti-solvent composition increases, the decrease in octadecanethiol solvation is more significant at lower ethanol-d_6 compositions compared to dodecanethiol, showing that the longer chain length is more sensitive to the changes in solvent composition. Anand et al. investigated the effect of chain length on GNP dispersibility in CO_2-expanded hexane, and suggested that dodecanethiol is an optimum ligand length for both favorable solvent-ligand interactions and ligand-ligand repulsive forces, thus enabling nanoparticle dispersibility under poor solvent conditions.[37] Our work compliments the work performed by Anand et al., where GNPs stabilized by octadecanethiol precipitate at lower ethanol compositions compared to dodecanethiol stabilized GNPs of a slightly larger size. Albeit, both hexane and toluene prove to be

good solvents for the alkanethiols on GNPs, as external force alone (centrifugation without ethanol addition) did not precipitate the GNPs out of solution, these results show that *n*-hexane-d_{14} solvates dodecanethiol more than toluene-d_8 in ethanol-d_6 mixtures. More explicitly, this work confirms that dodecanethiol may have an ideal ligand length contributing to greater nanoparticle dispersibility.

Shell Thickness Response to Ethanol Anti-Solvent

The shell thickness values for dodecanethiol and octadecanethiol modified GNPs were obtained as a function of ethanol-d_6 composition in toluene-d_8 and *n*-hexane-d_{14}. Figure 2.5A shows that as the ethanol-d_6 concentration increases, dodecanethiol thickness decreases from approximately 13 Å to 7 Å. Octadecanethiol also decreases in thickness upon increased ethanol-d_6 concentration (Figure 2.5B). In neat solvent, octadecanethiol extends into solution nearly 16 Å. At 20% ethanol-d_6 composition, octadecanethiol decreases in length to ~8 Å, and remains collapsed until complete nanoparticle precipitation at 45% ethanol concentration. The addition of ethanol-d_6 induces structural rearrangement of the ligand shell, causing the extended ligands to fold and collapse into a more compact state onto the core of the GNPs. The decreased ligand length leads to nanoparticle instability due to a decrease in steric repulsive forces and results in reversible nanoparticle precipitation beginning at 40 - 50% ethanol composition for octadecanethiol and dodecanethiol, respectively. Although the ligands are fully collapsed prior to the expected solvent precipitation compositions, the minimal ligand solvation is believed to provide sufficient repulsive forces to afford nanoparticle dispersibility. SANS

data analysis demonstrates that tuning the solvent properties enables control over ligand length and therefore nanoparticle dispersibility. However, as previously mentioned, nanoparticle dispersibility is a function of *several* factors which include: 1) chain length, 2) ligand solvation, 3) surface coverage, 4) the solvent properties, and 5) surface curvature.

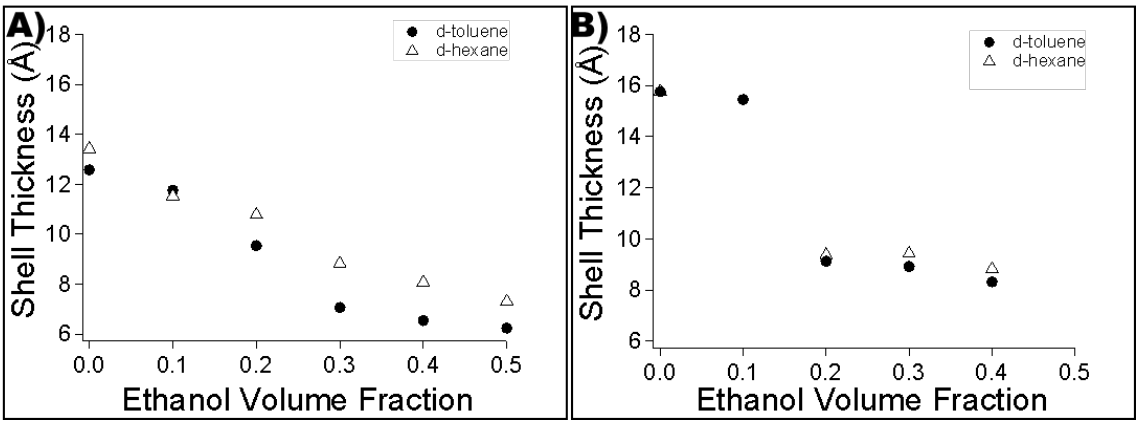

Figure 2.5: A) Dodecanethiol and B) octadecanethiol ligand shell thickness plotted as a function of ethanol-*d6* volume fraction for gold nanoparticles dispersed in either toluene-d_8 or *n*-hexane-d_{14}.

Flory-Huggins Interaction Parameter Response to Solvent Properties

To better understand the solvent-ligand interactions occurring during nanoparticle precipitation, we calculated the Flory Huggins interaction parameters (χ_{12}) of dodecanethiol and octadecanethiol in the organic solvent mixtures. Traditionally, $\chi_{12} < 0.5$ is an indicator of miscibility between a polymer and a solvent,[38] with lower values having more favorable interactions (solvation) . Investigation of this thermodynamic property enables the prediction of favorable solvent conditions without performing experiments and extends the potential of this work to other systems with other ligands and solvent mixtures.

We noted that values in literature[39-42] and those calculated for the solubility parameters of the alkanethiol ligands varied greatly (15.9 – 17.6 $MPa^{1/2}$ and 15.8 – 18.7 $MPa^{1/2}$ for dodecanethiol and octadecanethiol, respectively) and directly impact the calculated values for χ_{12}. Table 2.3 lists the solubility parameters, molecular weights, densities, and molar volumes for the hydrogenated solvents (toluene, hexane, and ethanol)[39] dodecanethiol,[42] and octadecanethiol[41] employed to determine the interaction parameters. Solubility parameters for the deuterated solvents were assumed to be comparable with the hydrogenated analogs for these calculations as the deuterated values were not readily available. Other SANS investigations have found deviations between the Flory-Huggins interaction parameter values for polymer systems comparing deuterated to hydrogenated solvents which may affect the results presented here.[43] χ_{12} was calculated as function of the molar volume of the mixture V_{molar_solv} (molecular weight/ density of the mixture), R (gas constant), temperature, and the solubility parameters[39] of the mixed solvent and dodecanethiol δ_{solv} and δ_{thiol} using Equation 2.3. The solubility parameters for the solvent mixtures (δ_1) were calculated based on mole fraction weighting of the neat solvents at the pre-determined solvent compositions.

$$\chi_{12} \approx \frac{V_{molar_{solv}}}{RT}(\delta_{solv} - \delta_{thiol})^2 \quad \textbf{(2.3)}$$

Table 2.3: Solubility Data for solvents and ligands

molecule	δ $(MPa)^{1/2}$	MW (g/mol)	Density (g/cm^3)	V_{molar} (cm^3/mol)
Hexane	14.9	86.81	0.656	132.3
Toluene	18.2	92.14	0.867	106.3
Ethanol	26	46.07	0.789	58.4
Dodecanethiol	17.6	202.4	0.845	239.5
Octadecanethiol	16.4	286.6	0.847	338.3

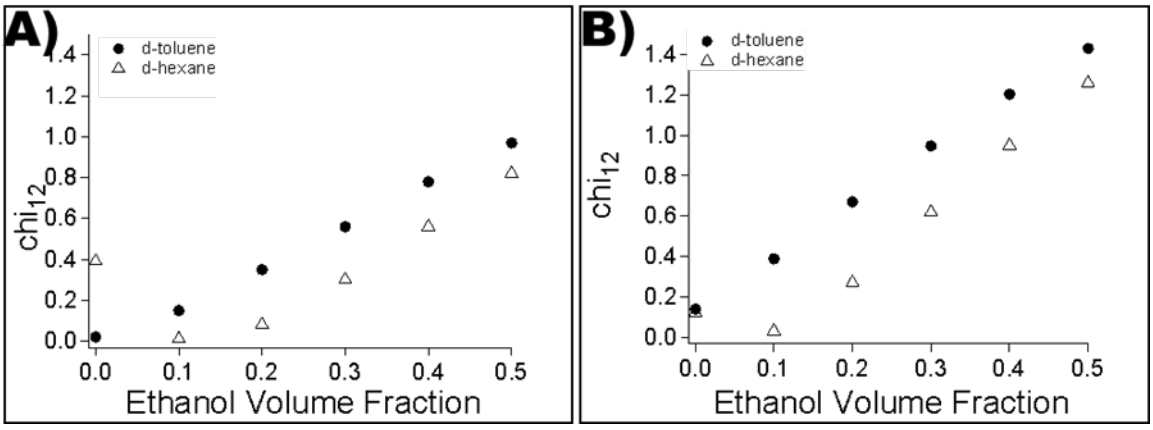

Figure 2.6: Calculated χ_{12} Flory-Huggins interaction parameter for A) dodecanethiol and B) octadecanethiol in the *n*-hexane-d_{14}/ethanol-d_6 and toluene-d_8/ethanol-d_6 solvent mixtures

Figure 2.6 shows χ_{12} values for dodecanethiol and octadecanethiol as a function of ethanol volume fraction in both hexane and toluene. χ_{12} is equal to 0.5 at ~0.37 and ~0.27 for dodecanethiol and ~0.26 and ~0.14 octadecanethiol at ethanol volume fractions in hexane and toluene, respectively. Figures 2.4 and 2.5 show the dodecanethiol and octadecanethiol thicknesses and solvation values to be substantially reduced when $\chi_{12} >$ 0.5 (compared to the respective values in neat solvent). In Figure 2.4A, the ethanol volume fractions of 0.3 and 0.4 are the initial solvent compositions measured where dodecanethiol solvation begins to equilibrate to a constant value prior to precipitation (for toluene-d_8 and *n*-hexane-d_{14}, respectively); the first decreased solvation measured for octadecanethiol occurs at approximately 0.2 ethanol volume fraction for both toluene-d_8 and *n*-hexane-d_{14}. A value of $\chi_{12} = 0.5$ corresponds well to the transition solvent compositions for decreased ligand solvation, and suggests that Flory-Huggins interaction parameters are useful in determining ligand solvation changes. Similarly, the Flory-

Huggins interaction parameters demonstrate that the decreases in ligand thicknesses also correspond well to $\chi_{12} = 0.5$, as shown in Figure 2.5.

Evaluation of χ_{12} values suggests better miscibility for dodecanethiol and octadecanethiol in *n*-hexane-d_{14} compared to toluene-d_8 when ethanol-d_6 anti-solvent is present (lower χ_{12} values are favorable). Pei et al. investigated the deposition of dodecanethiol modified GNPs by comparing thin films produced by solvent evaporation from both neat hexane and toluene.[42] This study points out that the solubility parameters of dodecanethiol and toluene are closer than dodecanethiol and hexane, which suggests that toluene is a better neat solvent for the GNP ligand tails. Calculated χ_{12} values for dodecanethiol were determined to be 0.02 in neat toluene and 0.39 in neat hexane, which supports the work of Pei et al. A minimum is evident for the ethanol-d_6/*n*-hexane-d_{14} due to the disparity in solubility parameters (Figure 2.6). The χ_{12} value for octadecanethiol was determined to be 0.12 and 0.14 in neat hexane and toluene, respectively and suggests that hexane provides better solvent-ligand interactions for octadecanethiol. The lower calculated interaction parameters correspond to the larger shell thicknesses and solvation values measured from SANS for *n*-hexane-d_{14} compared to toluene-d_8 when ethanol-d_6 anti-solvent is present, as their miscibility is predicted to be greater. Albeit, the calculated Flory-Huggins results show that agreeable correlations can be made with the SANS data, it is important to note that these calculations were not intended to determine ligand solvation and structural changes. Other factors including ligand surface coverage, solvent composition, ligand chain length, and solvation should also be considered when determining solvent-ligand interactions and dispersibility.

Dispersibility of GNP Clusters

The core diameters obtained by TEM imaging were compared to the radius of gyration (R_g), determined from low q scattering of the Guinier plot (ln(I) versus q^2). Although the R_g and radius obtained from TEM analysis are not the same value, they should be similar. The diameter of gyration ($D_g = 2 * R_g$) was observed to be larger than the diameter measured by TEM; this disparity is believed to be caused by GNP clustering in solution; ex. D_g = 42 nm compared to 3.9 ± 0.7 nm diameter (TEM) for dodecanethiol modified particles. As the anti-solvent composition increased in the dodecanethiol stabilized GNP dispersion (in toluene-d_8), D_g decreased from 42 nm to 22 nm at 40% ethanol-d_6 composition (see Figure 2.7A). Figure 2.7B shows the same decreasing trend for D_g with increasing ethanol composition for octadecanethiol stabilized GNPs. We expect the Guinier region for a 4 nm diameter particle to begin near 0.03 $Å^{-1}$ (see Figure 2.8A). The GNPs measured in neat solvent or low ethanol compositions in SANS experiments showed a Guinier region starting at 0.01 $Å^{-1}$ (see Figure 2.8B). The shift in Guinier region to lower q values is likely caused by nanoparticle clusters in solution.[46, 47]

To confirm the presence of GNP clusters, the SANS spectra for GNPs dispersed in toluene-d_8 were fit with a fractal model[28] on the q range from ~0.004 to 0.2 $Å^{-1}$ at varying ethanol-d_6 concentrations. Figure 2.8B shows the fit SANS spectra for dodecanethiol stabilized GNPs. Fractal model analysis yields a repeat block diameter for the clusters to be 5.2 nm in neat toluene-d_8 for both dodecanethiol and octadecanethiol stabilized GNPs. Figure 2.9 shows the repeat block diameters for both dodecanethiol and octadecanethiol to be relatively constant in the toluene-d_8/ethanol-d_6 mixture showing

that the GNP dispersions are stable, prior to their respective initial isolation compositions. At 50% ethanol-d_6, the dodecanethiol modified GNPs begin to precipitate, which is reflected by a decrease in the repeat block size to 2.2 nm (Figure 2.9). Similarly, a decrease in repeat block diameter is observed for octadecanethiol stabilized GNPs at 40% ethanol-d_6 composition to 3.5 nm. The core-sizes of the GNPs measured by TEM proved to be similar to the repeat block diameters fit from the fractal model compared to the D_g from Guinier analysis. The results from the fractal model demonstrate that the repeat block diameter is a good indicator of overall nanoparticle size, in particular for nanoparticles which are present in solution as clusters.

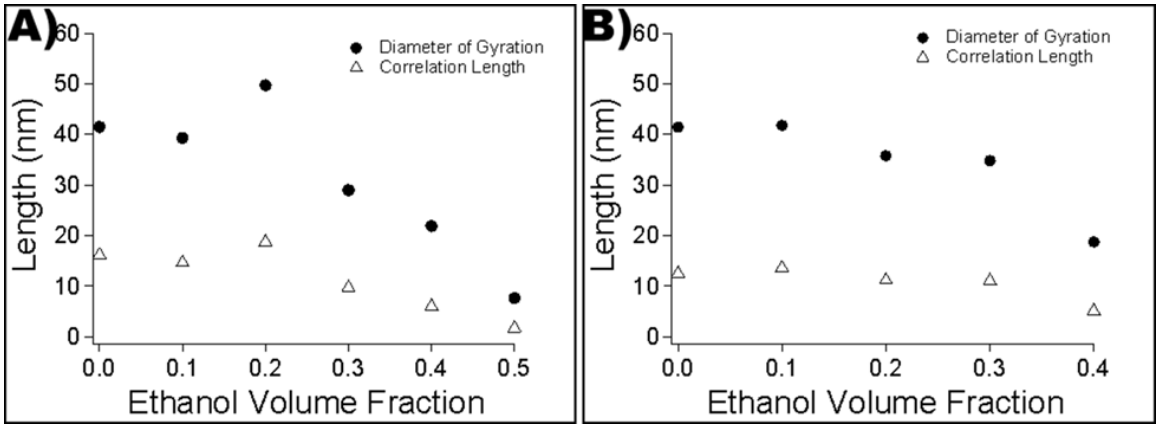

Figure 2.7: Diameter of gyration and correlation length for fractal-like clusters of A) dodecanethiol and B) octadecanethiol stabilized gold nanoparticles dispersed in toluene-d_8 with varying ethanol-d_6 composition. Both the diameter of gyration and correlation length were obtained by fitting SANS spectra with a fractal model.

The correlation lengths (indicative of the ordered cluster short range size dispersed in solution, Figure 2.7) were also found to be larger than the expected core-diameter of the individual GNPs (Figure 2.1). Increases of ethanol-d_6 composition from 0% to 20% and 0% to 10% in toluene-d_8 for dodecanethiol and octadecanethiol stabilized GNPs respectively demonstrated an increase in correlation length, which suggest that the reduced steric repulsive forces lead to nanoparticle clustering. At ethanol-*d6* compositions greater than 20%, a decrease in correlation length is observed prior to nanoparticle precipitation. The decrease in correlation length with increasing ethanol composition corresponds to shifts in the of the Guinier region to higher q values. Considering the gold clusters to be large individual GNPs dispersed in solution affords the clusters large van der Waals attractive forces (compared to the GNP building blocks). Hence, it is expected that the clusters precipitate at lower anti-solvent compositions compared to the GNPs.

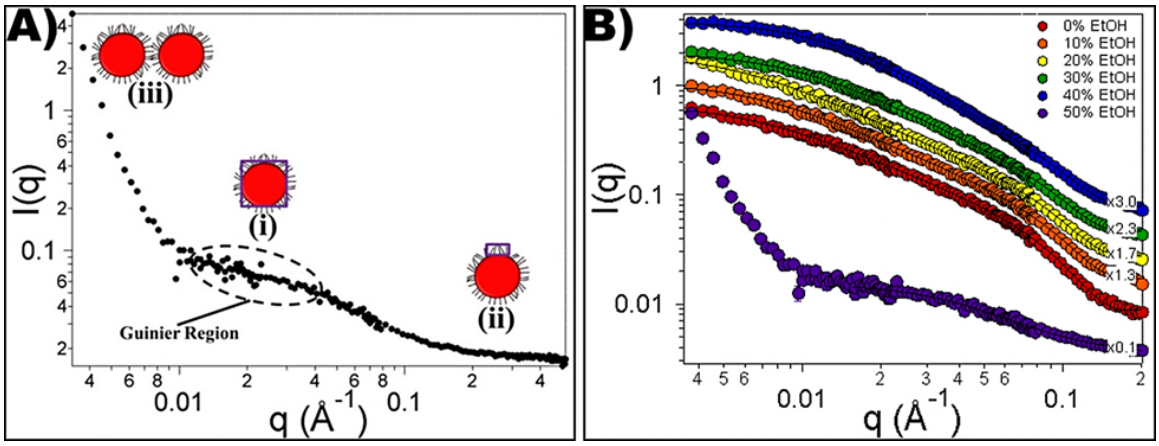

Figure 2.8: A) SANS spectra for dodecanethiol modified gold nanoparticles showing regions where (i) core-diameter (ii) ligand length and solvation, and (iii) particle-particle interactions can be determined. The Guinier region is shown to be in region (i) B) Fit SANS data for dodecanethiol modified gold nanoparticles dispersed in toluene-d_8 using a fractal model. The scattering spectra have been offset for clarity.

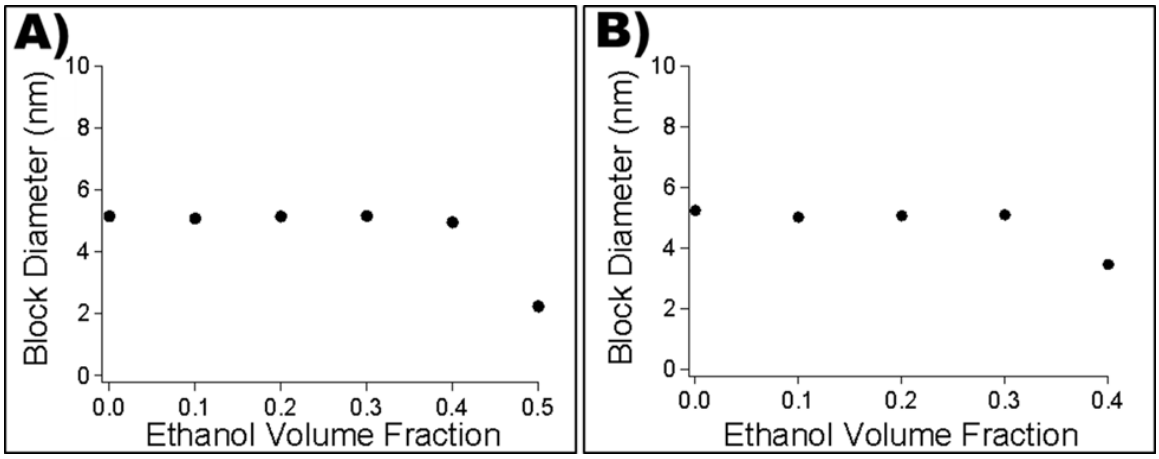

Figure 2.9: Repeat block diameter for A) dodecanethiol and B) octadecanethiol stabilized gold nanoparticles dispersed in toluene-d_8 with varying ethanol-d_6 composition as determined from fitting a fractal model to the SANS spectra.

Conclusions

Small-angle neutron scattering (SANS) was used to investigate the ligand response to increased ethanol-d_6 compositions. A polydisperse core-shell model was fit to the SANS spectra to determine the ligand shell thickness and solvation variation with changes in solvent conditions. Increased ethanol-d_6 anti-solvent compositions in both *n*-hexane-d_{14} and toluene-d_8 resulted in a decrease in both ligand length and solvation for octadecanethiol and dodecanethiol modified GNPs. The decreased ligand length and solvation resulted in nanoparticle precipitation, which occurs due to the weakened solvent properties as a function of ethanol-d_6 addition. The solvent compositions which induce decreased ligand shell thickness and solvation were shown to correlate with Flory-Huggins interaction parameter values ~0.5. Fractal model analysis of the SANS spectra demonstrated that clusters were present in the samples studied. The initial increase in correlation length upon ethanol-d_6 addition suggests that the weakened solvent strength induces GNP clustering in solution. Increased ethanol compositions leads to a decrease

in fractal correlation length caused by size-selective precipitation of the clusters; however, the repeat block diameter of the GNPs remains constant (~5 nm) until the expected nanoparticle precipitation solvent compositions. The ligand length and solvation values determined from SANS will prove useful in developing robust interaction energy models to predict nanoparticle dispersibility as a function of the solvent conditions and chain lengths, as well as the design of new nanoparticle processing techniques.

References

(1) Qi, W. H.; Wang, M. P. *Mater. Chem. Phys.* **2004** *88* 280-4.

(2) Murphy, C. J.; Sau, T. K.; Gole, A. M.; Orendorff, C. J.; Gao, J.; Gou, L.; Hunyadi, S. E.; Li, T. *J. Phys. Chem. B* **2005** *109* 13857-70.

(3) Bhattacharya, R.; Patra, C. R.; Earl, A.; Wang, S.; Katarya, A.; Lu, L.; Kizhakkedathu, J. N.; Yaszemski, M. J.; Greipp, P. R.; Mukhopadhyay, D.; Mukherjee, *Nanomed. Nanotechnol. Biol. Med.* **2007** *3* 224-38.

(4) Park, H.; Yang, J.; Seo, S.; Kim, K.; Suh, J.; Kim, D.; Haam, S.; Kyung-Hwa Yoo *Small* **2008** *4* 192-6.

(5) Scarberry, K. E.; Dickerson, E. B.; McDonald, J. F.; Zhang, Z. J. *J. Am. Chem. Soc.* **2008** *130* 10258-10262.

(6) LaLonde, A. D.; Grant Norton, M.; Zhang, D.; Ganadean, D.; Alkhateeb, A.; Padmanabhan, R.; McIlroy, D. N. *J. Mater. Res.* **2005** *20* 3021-7.

(7) Young Jun Kim; Yoon Seok Yang; Seung-Chul Ha; Cho, S. M.; Yong Shin Kim; Hye Yoon Kim; Yang, H.; Youn Tae Kim *Sensor. Actuat. B-Chem.* **2005** *106* 189-98.

(8) Ghosh, S. K.; Pal, T. *Chem. Rev.* 2007 ***107*** 4797-4862.

(9) Xu, X. -. N.; Huang, S.; Brownlow, W.; Salaita, K.; Jeffers, R. B. *J. Phys. Chem. B* **2004** *108* 15543-51.

(10) Sook, Y. M.; Kusunose, T.; Sekino, T. *Mater. Lett.* **2009** *63* 2038-40.

(11) Pileni, M. P.; Jiang, X. C. *Colloids Surf., A* **2007** *295* 228-32.

(12) Smetana, A. B.; Wang, J. S.; Boeckl, J.; Brown, G. J.; Wai, C. M. *Langmuir* **2007** *23* 10429-10432.

(13) Brust, M.; Walker, M.; Bethell, D.; Schiffrin, D. J.; Whyman, R. *J. Chem. Soc. - Chem. Commun.* **1994** 801-802.

(14) Korgel, B. A.; Fullam, S.; Connolly, S.; Fitzmaurice, D. *J. Phys. Chem. B* **1998** *102* 8379-88.

(15) Saunders, A. E.; Korgel, B. A. *J. Phys. Chem. B* **2004** *108* 16732-16738.

(16) Von White, G.; Kitchens, C. L. *J. Phys. Chem. C* **2010** *114* 16285-16291.

(17) Kitchens, C. L.; Roberts, C. B.; Juncheng, L.; Robert, A. W.; Madhu, A.; Von, W. G.; Hurst, K. M.; Saunders, S. R. In *Application of Gas-Expanded Liquids for Nanoparticle Processing: Experiment and Theory;* Gas-Expanded Liquids and Near-Critical Media; American Chemical Society: Washington, DC, **2009**; pp 290-308.

(18) Anand, M.; You, S.; Hurst, K. M.; Saunders, S. R.; Kitchens, C. L.; Ashurst, W. R.; Roberts, C. B. *Ind. Eng. Chem. Res.* **2008** *47* 553-559.

(19) Kitchens, C. L.; Roberts, C. B. *Ind. Eng. Chem. Res.* **2004** *43* 6070-6081.

(20) Fernandez, C. A.; Hoppes, E. M.; Bekhazi, J. G.; Wang, C.; Wiacek, R. J.; Warner, M. G.; Fryxell, G. E.; Bays, J. T.; Addleman, R. S. *J. Phys. Chem. C* **2008** *112* 13947-13957.

(21) Saunders, S. R.; Roberts, C. B. *Nanotechnol* **2009** *20* .

(22) Hurst, K. M.; Roberts, C. B.; Ashurst, W. R. *Nanotechnol.* **2009** *20* 185303 (9 pp.).

(23) McLeod, M. C.; Anand, M.; Kitchens, C. L.; Roberts, C. B. *Nano Lett.* **2005** *5* 461-5.

(24) Abramoff, M. D.; Magalhaes, P. J.; Ram, S. J. *Biophoton Int.* **2004** *11* 36-41.

(25) Glinka, C. J.; Barker, J. G.; Hammouda, B.; Krueger, S.; Moyer, J. J.; Orts, W. J. *J. Appl. Crystallogr.* **1998** *31* 430-45.

(26) Kline, S. R. J. Appl. *Crystallogr.* **2006** *39* 895-900.

(27) Bartlett, P.; Ottewill, R. H. *J. Chem. Phys.* **1992** *96* 3306-3318.

(28) Teixeira, J. In *In Small-angle scattering by fractal systems;* International Conference on Applications and Techniques of Small-Angle Scattering; Denmark, **1988**; Vol. 21, pp 781-5.

(29) Munter, A. Scattering Length Density Calculator. http://www.ncnr.nist.gov/resources/sldcalc.html (accessed 12/28, 2009).

(30) Jana, N. R.; Gearheart, L.; Murphy, C. J. *J. Phys. Chem. B* **2001** *105* 4065-7.

(31) Hong, R.; Fernandez, J. M.; Nakade, H.; Arvizo, R.; Emrick, T.; Rotello, V. M. *Chem. Commun.* **2006** 2347-2349.

(32) Guo, R.; Song, Y.; Wang, G.; Murray, R. W. *J. Am. Chem. Soc.* **2005** *127* 2752-2757.

(33) Liu, J.; Anand, M.; Roberts, C. B. *Langmuir* **2006** *22* 3964-3971.

(34) Jana, N. R.; Gearheart, L.; Murphy, C. J. *Langmuir* **2001** *17* 6782-6.

(35) Butter, K.; Hoell, A.; Wiedenmann, A.; Petukhov, A. V.; Vroege, G. -J. *J. Appl. Crystallogr.* **2004** *37* 847-56.

(36) Korgel, B. A.; Fitzmaurice, D. *Phys. Rev. B: Condens. Matter* **1999** *59* 14191-201.

(37) Anand, M.; McLeod, M. C.; Bell, P. W.; Roberts, C. B. *J. Phys. Chem. B* **2005** *109* 22852-22859.

(38) Ovejero, G.; Pérez, P.; Romero, M. D.; Guzmán, I.; Dı´ez, E. *Eur. Polym. J* 2007 ***43*** 1444-1449.

(39) Brandrup, J.; Immergut, E. H.; Grulke, E. A.; Abe, A.; Bloch, D. R. , In *Polymer Handbook (4th Edition)*. Online version available at: http://knovel.com/web/portal/browse/display?_EXT_KNOVEL_DISPLAY_bookid=1163&VerticalID=0

(40) Yaws, C. L. **2003**, In *Yaws' Handbook of Thermodynamic and Physical Properties of Chemical Compounds* . Online version available at: http://www.knovel.com/web/portal/browse/display?_EXT_KNOVEL_DISPLAY_bookid=667

(41) Mullen, K.; Carron, K. *Anal. Chem.***1994** *66* 478-483.

(42) Pei, L.; Mori, K.; Adachi, M. *Colloids Surf. Physicochem. Eng. Aspects* **2006** *281* 44-50.

(43) Graessley, W. W.; Krishnamoorti, R.; Balsara, N. P.; Fetters, L. J.; Lohse, D. J.; Schulz, D. N.; Sissano, J. A. *Macromolecules* **1993** *26* 1137-1143.

(44) Kitchens, C. L.; McLeod, M. C.; Roberts, C. B. *J. Phys. Chem. B* **2003** *107* 11331-11338.

(45) Vincent, B.; Luckham, P. F.; Waite, F. A. *J. Colloid Interface Sci.* **1980** *73* 508-521.

(46) Saint-Michel, F.; Pignon, F.; Magnin, A. *J. Colloid Interface Sci.* **2003** *267* 314-319.

(47) Schaefer, D. W.; Martin, J. E.; Wiltzius, P.; Cannell, D. S. *Phys. Rev. Lett.* **1984** *52* 2371-4.

CHAPTER THREE

SMALL-ANGLE NEUTRON SCATTERING OF SILVER NANOPARTICLES IN GAS-EXPANDED HEXANE

As published in The Journal of Physical Chemistry C **2010**, 114 (39), pp 16285-16291

with modifications

Introduction

As research continues in the field of nanotechnology, many techniques have been developed for the synthesis and processing of metallic nanoparticles into various sizes,[1] shapes,[2, 3] compositions,[4] and surface chemistry.[5,6] Novel applications that utilize the unique size-dependent properties of monodisperse metallic nanoparticles include optical/chemical sensors[7] and biomedical applications.[8, 9] It is well known that the unique properties (optical,[10] magnetic,[11] and electrical[12]) of these nanoparticles vary greatly as a function of size, shape,[13] material type,[14] and surface chemistry.[15,12] With advances in solution based synthesis and applications of novel nanoparticles, knowledge of the ligand structure and behavior as a function of the dispersing solvent medium is increasingly important as it is fundamental to nanoparticle stability, dispersibility and application. Specialty nanoparticle synthesis protocols often sacrifice particle size, shape, and/or ligand coverage uniformity in order to obtain desired properties or large scale production. In this case, post-synthesis processing and fractionation are required to obtain uniform nanoparticle populations.

Gas-expanded liquids[16] (GXLs) have significant potential for size-selective fractionation of nanoparticles to obtain monodisperse populations.[17] In particular, CO_2

expanded hexane has been used to size-selectively fractionate Au[6], CdSe/ZnS[18], Ag[1], and Pt[19] nanoparticles less than 10nm in diameter and stabilized by hydrophobic ligands. Particle populations with polydispersities of 25% or more can be fractionated to less than 10% with recursive fractionations using CO_2 as an anti-solvent.[17] GXLs have also been used to adsorb nanoparticles to surfaces, effectively infusing nanoparticles into porous structures,[20] and form uniform wide-area networks of nanostructures through the removal of the gas/liquid interface present in solvent drying deposition.[6, 19] In both nanoparticle fractionation and deposition, the CO_2 mole fraction is dependent on the system CO_2 partial pressure, thus 1) providing a tunable solvent media where nanoparticle dispersibility can be controlled with pressure and 2) demonstrating a potential for greater control of nanoparticle dispersibility and selectivity during processing (ex. size-selective fractionation) compared to liquid-liquid techniques. Additional benefits of GXLs include the significantly reduced time and solvent requirements for nanoparticle post-synthesis processing. For example, traditional post-synthesis processing techniques of liquid anti-solvent fractionation produce large volumes of mixed solvent waste (e.g., 800 mL ethanol required to purify 214 mg of gold nanoparticles with the toluene/ethanol solvent/anti-solvent system) and require time and energy intensive centrifugation for nanoparticle isolation.[5] Due to the reversibility of the GXL technique, simply relieving CO_2 pressure after nanoparticle fractionation affords nanoparticle redispersion and facile solvent and anti-solvent recycle, virtually eliminating any solvent waste.

Interaction energy models have been developed to fundamentally describe the dispersibility of nanoparticles in solution, including GXLs.[21, 22] Vincent et al.

investigated the stability/flocculation of free polymer in solution and suggested that elastic and osmotic repulsive forces play a role in their dispersibility.[23] Based on "soft sphere" theory, Shah et al. incorporated the elastic (ligand length) and osmotic (ligand solvation) contributions into interaction energy models to better predict nanoparticle dispersibility for silver and gold nanoparticles in supercritical ethane,[24] another pressure tunable fluid. These interaction energy models have been used to predict the dispersibility of dodecanethiol capped silver nanoparticles where the ligand length, metal type, size, solvent properties, and surface coverage impact the particle dispersibility.[22, 25] The practical function of these models is to predict the maximum particle size dispersible in solution at certain defined conditions and determine the relative impact of system variables on the ability to control the particle size synthesized or perform a post-synthesis size fractionation. However, the models rely on an accurate description of the nanoparticle ligand and often over-predict the particle size.[22, 26] Therefore, a detailed understanding of the nanoparticle ligand structure and solvation during anti-solvent precipitation is required to develop more accurate and robust models of nanoparticle behavior.

We have used small angle neutron scattering (SANS) to measure the nanoparticle ligand structure (ligand shell thickness) and the degree of ligand solvation (mole fraction of solvent within the ligand shell) as a function of the bulk GXL solvent composition; a novel use for SANS and a significant advancement for the fundamental understanding of nanoparticle dispersibility in CO_2 GXL systems. SANS is an ideal method of characterization for this system based on the length scales of interest (sub 10 nm diameter

particles and sub 15 Å ligand shell thickness) and the ability to introduce solvent/ligand contrast through selective deuteration. SANS was also used to measure the mean particle diameter and ligand surface coverage for four sizes of dodecanethiol stabilized silver nanoparticles in deuterated *n*-hexane-d_{14} with varying CO_2 mole fraction up to the point of nanoparticle precipitation. Results from this work demonstrate a simultaneous decrease in ligand shell thickness and ligand solvation with increasing CO_2 pressure, which leads to nanoparticle precipitation. This work also provides insight into the impact of nanoparticle surface curvature on the ligand structure and degree of ligand surface coverage. Based on our SANS results, we also suggest a novel concept for nanoparticle fractionation where dispersibility is a function of ligand surface coverage.

Experimental Methods

Materials

Metal precursor silver nitrate ($AgNO_3$, 99.995%) was ordered from VWR. The phase transfer catalyst tetraoctylammonium bromide (TOAB, 98%), stabilizing ligand 1-dodecanethiol (98%), and reducing agent sodium borohydride ($NaBH_4$, 98%) were purchased from VWR. The solvents ethanol (95%), chloroform (99.8%), and *n*-hexane (95%) were supplied by VWR. *n*-Hexane-d_{14} was purchased from Cambridge Isotope Laboratories (98%). The CO_2 was obtained from National Welders and was Coleman Grade (99.99%). All chemicals were used without further purification. All glassware used for the synthesis of metallic nanoparticles were washed and rinsed with acetone, rinsed with DI water, and then dried using compressed air.

Silver Nanoparticle Synthesis

Silver nanoparticles were synthesized by the Brust method in a biphasic system.[5] The resulting nanoparticle dispersion was washed with ethanol (5 mL of dispersion to 10 mL of ethanol) and centrifuged for 20 minutes at 6000 rpm to remove the excess dodecanethiol. The supernatant was removed, and the nanoparticles were re-dispersed in *n*-hexane for fractionation. The washing process was repeated 3 times. The nanoparticle diameters (3-8 nm), were measured with a Hitachi 7600 TEM and the size distributions were obtained via analysis in the ImageJ software package.[27]

Metal Nanoparticle Fractionation

The silver nanoparticles were size-fractionated using the gas-expanded liquid (GXL) technique described by McLeod et al. and re-dispersed in *n*-hexane-d_{14} following depressurization with moderate agitation in the deuterated solvent.[28] Similar to McLeod et al., a cylindrical glass rod with a spiral groove was placed inside of a stainless steel pressure vessel in order to size-fractionate the nanoparticles using the pressure tunable GXL solvent (see Figure 1.1). 500 μL of *n*-hexane was added to the pressure vessel to help prevent solvent evaporation during fractionation. A small aliquot (~100 μL) of *n*-hexane dispersed metal nanoparticles was placed in the first spiral rung of the glass rod and the vessel was sealed. Four different populations of silver nanoparticles with mean diameters of 7.1 ± 1.5 nm, 6.9 ± 1.4 nm, 6.6 ± 0.9 nm, and 5.9 ± 0.9 nm and capped with dodecanethiol were isolated between 400 to 450 psi, 450 to 500 psi, 500 to 550 psi, and 550 to 600 psi respectively and later investigated in the neutron scattering experiments.

To isolate dodecanethiol stabilized silver nanoparticles, the pressure vessel was charged to 400 psi and held for 20 minutes. The glass cylindrical rod was rotated 360°, allowing for the particles larger than 7.1 nm in diameter to precipitate and remain in the first rung of the rod. The CO_2 pressure was increased to 500 psi and held for 20 minutes allowing the 7.1 nm fraction to precipitate. The cylindrical rod was again rotated 360°. The CO_2 pressure was then slowly released (15 psi/min), and the second fraction (those nanoparticles precipitated between 400 and 500 psi) were then collected by re-dispersing them in *n*-hexane-d_{14}. This procedure was repeated until the desired amount of nanoparticles was collected. After re-dispersing the particles in the deuterated solvent, they were again fractionated with CO_2, but at 50 psi below their upper precipitation pressure (final $\Delta P = 50$ psi) to ensure no aggregates were present in the sample from the drying process and to lower the polydispersity once more. Fractionation was repeated at varying CO_2 mole fractions to obtain different populations of dodecanethiol stabilized silver nanoparticles. Figure 3.1 shows a TEM image and size distribution for the particles isolated between 450 to 500 psi measured to be 6.9 ± 1.4 nm. Table 3.1 lists all of the nanoparticles investigated and their corresponding isolation conditions. The SANS results for particle core diameter for the size-fractionated particles is similar to previous experiments for both mean particle size and size distribution obtained at various isolation pressures.[28]

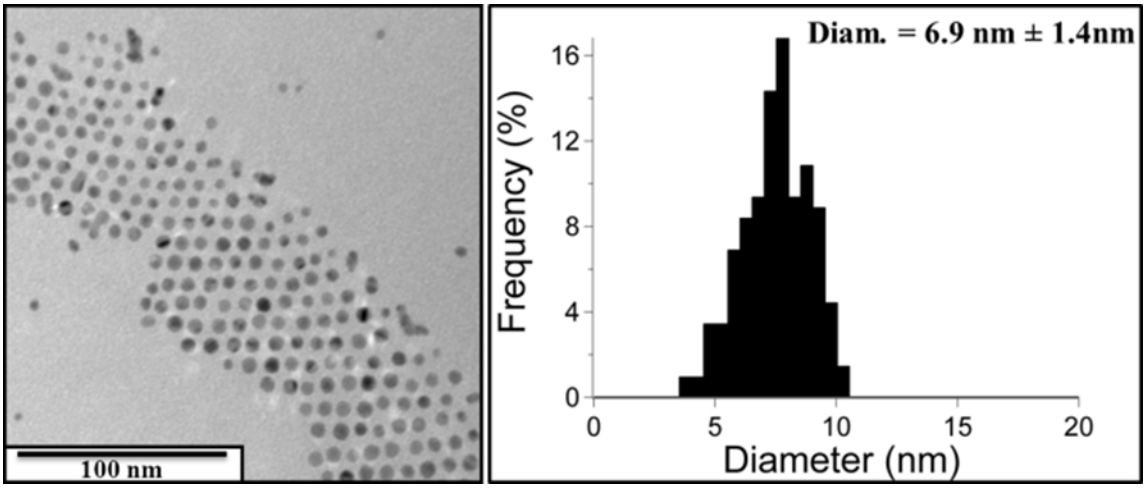

Figure 3.1: TEM image of silver nanoparticles capped by dodecanethiol after fractionation using GXL technique (on average 6.9 ± 1.4nm in diameter)

Table 3.1: Summary of metal nanoparticles studied in the SANS experiments
*The mean core diameter and polydispersity measurements were made from TEM images (over 300 particles counted for each sample). These results are similar to those measured from the SANS experiments. The remaining mean core size and standard deviation measurements were fit from the SANS data.

fraction (psi)	CO_2 fraction in GXL	mean diam. (nm)	σ diam. (nm)	surface coverage
400 to 450	37 to 44%	7.2 (7.1*)	1.4(1.5*)	44%
450 to 500	44 to 51%	7.0(6.9*)	1.3(1.4*)	55%
500 to 550	51 to 58%	6.6	1	62%
550 to 600	58 to 66%	5.9	0.9	60%

Small Angle Neutron Scattering (SANS) Experiments

SANS experiments were performed on the NG7 30 m SANS instrument at NIST Center for Neutron Research (NCNR, Gaithersburg, MD)[29] and the CG-2 General SANS instrument at the High Flux Isotope Reactor (HFIR) at Oak Ridge National Laboratories (ORNL) (Oak Ridge, TN). At NCNR, two sample-to-detector distances were used (1 m and 7.8 m) to obtain a q range from 0.007 to 0.23 $Å^{-1}$ with a neutron wavelength of λ = 6Å and a resolution of $\Delta\lambda/\lambda$ equal to 12% (FWHM). SANS experiments at ORNL used

one sample-to-detector distance at 6m with a neutron wavelength of 4.8 Å and a resolution of ~15% (FWHM), yielding a q range between 0.005 to 0.18 $Å^{-1}$. Empty beam background, empty cell background, detector sensitivity, sample transmission, and a sample thickness for a 1mm (NIST) or 4mm (ORNL) path length sample were used in the raw data reduction. The radial averaged reduced scattering intensity, I(q), was fit as a function of the scattering vector, q(θ). Where $q(\theta) = 4\pi\sin(\theta)/\lambda$ and θ is the scattering angle. All SANS fitting was done using Igor Pro 6.03 software and models provided by NIST.[30] Figure 3.2 shows fit SANS data for dodecanethiol stabilized silver nanoparticles.

The molar composition of the GXL solvent (*n*-hexane-d_{14} and CO_2) varies as a function of CO_2 pressure. As CO_2 pressure is increased in gas-expanded hexane, the molar composition of CO_2 in the GXL mixed solvent increases. The Patel-Teja equation of state (PT-EOS) was used to calculate the molar composition and properties of the CO_2 expanded *n*-hexane-d_{14} as a function of pressure. The PT-EOS is well suited for GXLs, as it allows for adjustability of the critical compressibility factor, and experimental data for hydrocarbon/CO_2 deviations is available for comparison.[31] The *n*-hexane-d_{14} /CO_2 GXL mixture density was calculated using the PT-EOS for pressures ranging from 0 to 717 psi using parameters obtained from published CO_2 – *n*-hexane VLE phase behavior[32, 33] including T_c, P_c, and Z_C, (304.1 K, 73.8 bar, 0.309 for CO_2 and 507.6 K, 30.25 bar, 0.308 for *n*-hexane), the K_{ij} and L_{ij} parameters (0.138 and 0.074 respectively), and appropriate molecular weights and pure solvent densities for the deuterated and hydrogenated *n*-hexane. The scattering length density (SLD) was calculated for the

deuterated GXL mixtures (using densities obtained from the PT-EOS, see Table 3.2), hydrogenated nanoparticle ligand and silver nanoparticle core (3.47×10^{-6} Å^{-2}) using the NIST NCNR SLD calculator.[34] Table 3.2 shows the calculated values for the CO_2 molar percentages, densities, and percent volume expansion as a function of CO_2 pressure for the GXL using the PT-EOS. A second order polynomial trend line was used to interpolate SLDs for pressures not initially calculated with the NCNR SLD calculator.[34] The calculated values for the SLD of the solvent were used during the data fitting after confirming the validity. The mean core-diameter, ligand length, and SLD of the ligand shell were investigated by fitting the SANS data in the q range of ~0.02 to ~0.2 Å^{-1} as a function of CO_2 mole fraction in the GXL.

A spherical model[35] was initially used to fit the reduced scattering data for the dodecanethiol capped 5.9 nm diameter silver nanoparticles. Figure 3.3A depicts the parameters of the sphere model used to measure the core radius and the SLD_{solv} as a function of pressure. The radius of the metal core and SLD of the solvent (SLD_{solv}) were adjustable parameters in the sphere model. First, the calculated SLD_{solv} values were held constant to fit the radius of the silver core as a function of pressure, which corresponds to TEM data (Figure 3.1) and previous literature results.[1] Next, the radius was held constant and SLD_{solv} became an adjustable parameter during refitting of the SANS data over the measured pressures. This second fitting was performed to compare the SLD_{solv} values obtained from the PT-EOS with the SANS modeling results. For both fits, the SLD_{solv} and radius were not used simultaneously as adjustable parameter to ensure accurate

results for the SLD_{colv}. For all other fitting, the calculated SLD_{solv} values determined from the PT-EOS and NCNR NIST SLD calculator[34] were used.

A core-shell model,[35] depicted in Figure 3.3B, was used to determine the SLD and thickness of the dodecanethiol stabilizing ligand shell for the GXL metal nanoparticle dispersions using the nanoparticle diameter and SLD_{solv} determined from the sphere modeling data. Fitting the shell thickness parameter provides information regarding the ligand shell structure (thickness, t) and ligand solvation data from the SLD of the shell (SLD_{shell}). The radius and SLD of the metal core (SLD_{core}) and the SLD_{solv}, determined from the sphere model, were held constant with the core-shell model.[35]

Additional SANS fitting was performed using a polydisperse core, constant shell thickness model[36] at ambient pressure, prior to any ligand shell changes, in order to estimate the nanoparticle diameter polydispersity. The radius, SLD_{core}, SLD_{shell}, SLD_{solv}, and shell thickness were held constant as previously determined from the core-shell and sphere models such that the polydispersity of the core radius was the only fitting parameter in this third model. For an in depth discussion of the sphere and core-shell model employed for SANS data analysis, please see Appendix A.

Table 3.2: Calculated solvent variables for the *n*-hexane-d_{14} /CO_2 solvent
*Scattering length densities were calculated using the NCNR NIST SLD calculator and densities obtained from the Patel-Teja Equation of State (PT-EOS)

p (psi)	x, CO_2	density (g/cm^3)	SLD* (Å^{-2})	volume expansion
0	0%	0.767	6.14E-06	0%
116	8%	0.768	5.98E-06	1%
208	16%	0.770	5.85E-06	6%
296	24%	0.773	5.67E-06	11%
407	36%	0.775	5.36E-06	21%
454	42%	0.776	5.19E-06	27%
585	60%	0.774	4.50E-06	63%
660	72%	0.766	3.89E-06	113%
717	81%	0.750	3.31E-06	190%

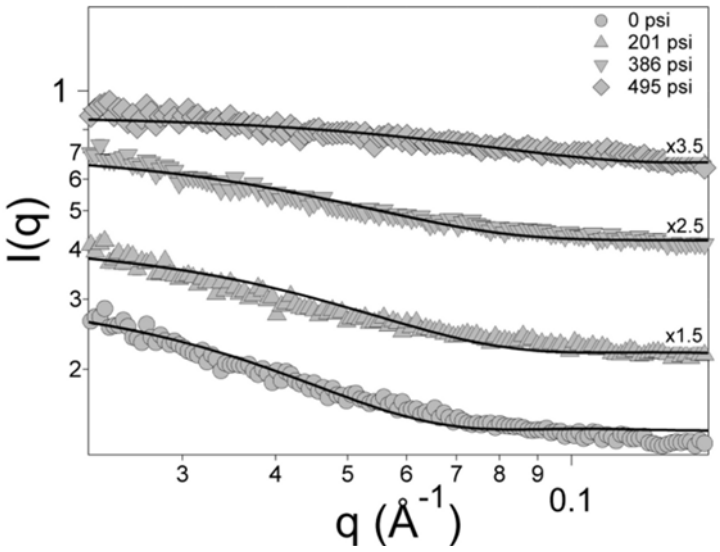

Figure 3.2: Reduced and fit SANS data (using a core-shell model) measured at ORNL for 6.9nm Ag NPs capped by dodecanethiol with varying CO_2 pressure ranging from 0 to 495 psi. The SANS curves have been offset for clarity and are labeled appropriately.

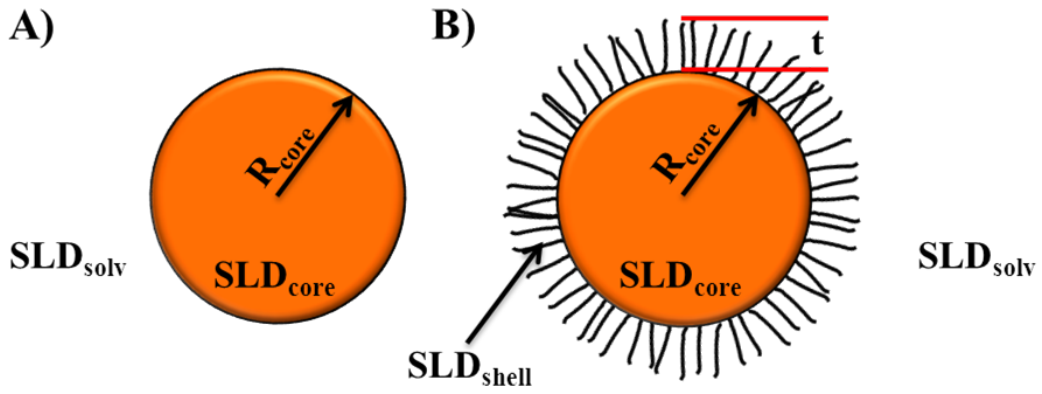

Figure 3.3: Schematic of the A) spherical model and B) core-shell model. Adjustable parameters include the nanoparticle size, R_{core}; scattering length density (SLD) of the nanoparticle core, ligand shell and bulk solvent; and the shell SLD and shell thickness, t.

Results and Discussion

Many variables impact nanoparticle dispersibility in non-polar media, most notably ligand length and ligand solvation. This work uses SANS to determine these contributions to the dispersibility of dodecanethiol stabilized silver nanoparticle as a function of CO_2 mole fraction and discusses the role that varying size (surface curvature) and surface coverage play on ligand length and ligand solvation. These measurements will aid in the development of accurate nanoparticle interaction energy models and better prediction of nanoparticle dispersion in solutions with varying size, shape, polydispersity, composition, ligand type, Hamaker constant (metal type), and surface coverage.

SANS on the CO_2/Hexane GXL System

Prior to analyzing the SANS data for the silver nanoparticle dispersions in gas-expanded hexane, calculation of the solvent composition of the CO_2/hexane mixture and validation of the SLD_{solv} from SANS fittings are necessary because these results are

critical for ligand length and ligand solvation determination. Figure 3.4 compares the SLD of the *n*-hexane-d_{14} – CO_2 GXL solvent as a function of pressure for the 5.9 nm diameter silver nanoparticles capped by dodecanethiol with the SLD values calculated from the PT-EOS and NIST SLD calculator.[34] The values are comparable, with minimal difference between the calculated and measured values. Based on mole fraction weighting, the SLD_{solv} of the GXL decreases as expected due to the molar composition of CO_2 increasing with pressure, from 6.14 x 10^{-6} $Å^{-2}$ down to 4.50 x 10^{-6} $Å^{-2}$ which corresponds to 0 and 60% CO_2 mole fraction. The calculated SLD_{solv} values (shown in Table 3.2) were used throughout the SANS fitting discussed in this paper.

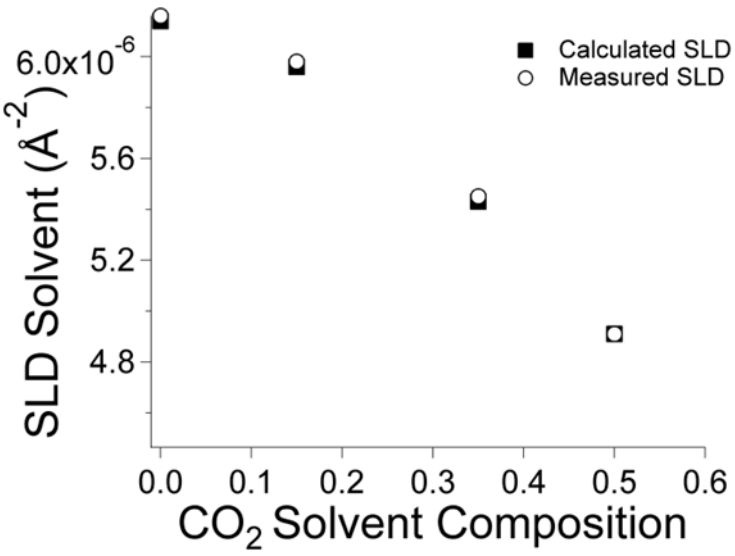

Figure 3.4: Scattering Length Density (SLD) of *n*-hexane-d_{14} as a function of pressure, measured using the spherical model versus calculated using the NCNR NIST SLD calculator.

The Role of Size on Nanoparticle Dispersibility

Figure 3.5 presents the mean nanoparticle diameters for four populations of dodecanethiol capped silver nanoparticles as a function of CO_2 mole fraction, obtained from fitting the SANS intensity using a sphere model.[35] The reduced χ^2 values for the all SANS spectra were all on the order of 5 or less (where χ^2 is the goodness of fit, $\chi^2 = (R^2/N)^{1/2}$ and R^2 is the difference of the slope for the fitted line of the least squares regression and zero). A smaller χ^2 value indicates a better fit of the data, where reasonable results are less than 5. The mean particle diameters obtained from the SANS data are comparable to TEM data, as evidenced by comparing Figure 3.1 and Figure 3.5 at 0% CO_2 mole fraction.

Figure 3.5 shows that with increasing CO_2 mole fraction, the mean diameter of silver nanoparticles dispersed in solution decreases, which is supported in the literature and has been used to size fractionate nanoparticles.[1] Nanoparticle interaction energy models have been used to describe this behavior, where the largest particles precipitate out of solution first under anti-solvent conditions due to their greater van der Waals attractive forces.[22] Figure 3.5 demonstrates further size fractionation with increasing CO_2 pressure, even though a precursive GXL fractionation was employed prior to the SANS experiments. The large sample quantities necessary for the SANS studies required the fractionation of large concentrations of silver nanoparticles. Fractionation of high concentrations of nanoparticles may yield more polydisperse samples compared to lower concentrations. The fractionation procedure used was not fully optimized to obtain the most monodisperse population of particles. Therefore, it is evident for our samples that

as the CO_2 mole fraction increases, the largest particles precipitate out of solution, lowering the average size of dispersed particles, the particle concentration, and the polydispersity of the sample. Size-selective particle fractionation is noticeable within the data; however, sample polydispersity was not determined at GXL compositions greater than 0% CO_2 due to the lack of a minimum in the I vs q plots and limitation in the maximum q value as a result of the pressure cell geometry.

Evaluation of Ligand Solvation and Surface Coverage

The fit values for shell scattering length density (SLD_{shell}) as a function of CO_2 mole fraction for the silver nanoparticles capped by dodecanethiol are shown in Figure 3.6. The SLD_{shell} is comprised of both the SLD_{tail} (-3.67×10^{-7} Å^{-2}) for the hydrogenated hydrocarbon tail of dodecanethiol and the GXL SLD_{solv} for the solvent mixture of *n*-hexane-d_{14} and CO_2. At ambient pressure, the SLD_{shell} is on the order of 8×10^{-7} Å^{-2} for the 6.6 nm, 6.9 nm, and 7.1 nm silver nanoparticles and 1×10^{-6} Å^{-2} for the 5.9 nm diameter silver nanoparticles. As CO_2 is dissolved into the organic nanoparticle solutions, the molar composition of the solvent changes and impacts the solvent environment within and around the ligand shell. The SANS fitting demonstrates a decrease in the SLD_{shell} occurring between 0% and 17% CO_2 for each silver nanoparticle population. Both the SLD_{solv} (Figure 3.4) and SLD_{shell} (Figure 3.6) decrease as the molar composition of CO_2 increases in the GXL; however, the decreasing trend is much more significant in the shell than the solvent, particularly at CO_2 mole fractions below 30%. This suggests that CO_2 is inducing a compositional change within the ligand shell beyond the simple change in

bulk solvent composition. This can be attributed to the collapse of the ligands on the surface of the nanoparticle, as well as potential preferential solvation of the ligands. The significantly lower SLD_{shell} values at elevated CO_2 mole fractions (above 30%) indicate that the molar composition of the shell is largely composed of the hydrogenated alkanethiol tail as opposed to the GXL solvent mixture. Thus increasing CO_2 mole fraction promotes decreased ligand solvation, which results in decreased nanoparticle dispersibility.

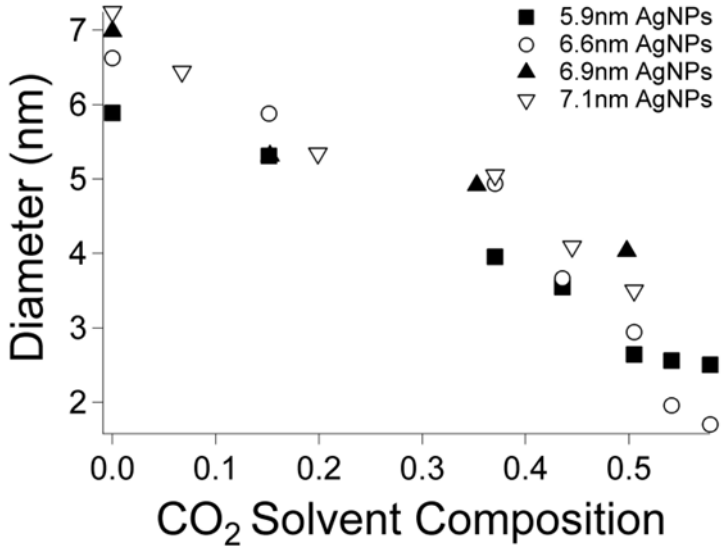

Figure 3.5: Mean diameter for four different silver nanoparticle populations capped by dodecanethiol dispersed in *n*-hexane-d_{14} as a function of CO_2 mole fraction measured at both NIST and ORNL.

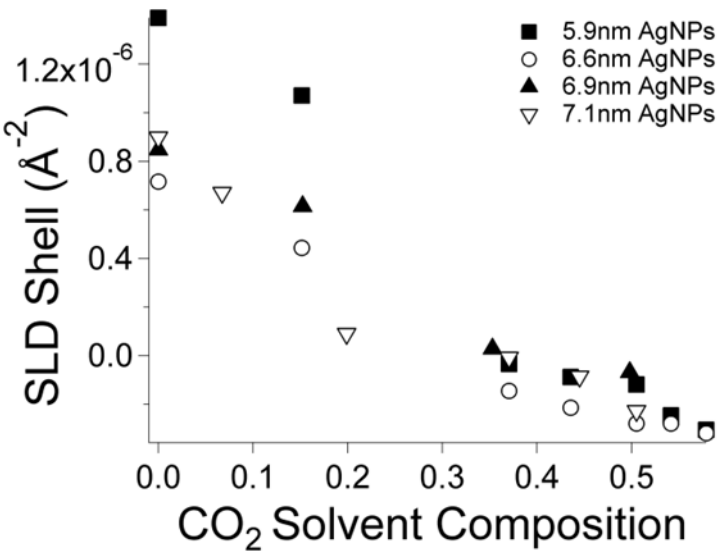

Figure 3.6: Scattering length density of the stabilizing ligand shell vs. CO_2 mole fraction for four different silver nanoparticle dispersions, all capped by dodecanethiol dispersed in *n*-hexane-d_{14}

The percent ligand solvation (mole fraction of solvent within the ligand shell) can be calculated by evaluating the SLD_{shell} as compared to the SLD_{solv} and SLD_{tail} using Equation 3.1 and assuming that the solvent composition in the shell and the bulk are equivalent. This equation was also used by Butter et al. for determining ligand solvation of oleic-acid capped magnetic iron nanoparticles.[37] The percent ligand solvation is proportional to the SLD_{shell} and shows the same trends.

Equation 3.2 was used to determine the percent ligand surface coverage at 0% CO_2 mole fraction with the percent ligand solvation and assuming spherical particles. A_{head} represents the total area taken up by a thiol head group on the surface of the nanoparticle assumed to be 0.16 nm^2 from literature[38], N_A is Avogadro's number, V_{molar_thiol} is the calculated molar volume of dodecanethiol (239.5 cm^3/mol), and $r_{core+shell}$ and r_{core} are the radius of the core + shell and core of the nanoparticle, respectively. It

should be noted that this relationship does not assume a cylindrical ligand volume, differing from other work,[37] and for the 6.9 nm diameter particles, 0% ligand solvation yields a maximum surface coverage of 66%. The ligand surface coverage ranged from 44% to 62% for the four silver nanoparticle dispersions and demonstrated size-dependence as well as fractionation dependence (see Table 3.1). The obtained surface coverage values in Table 3.1 are less than those previously presented in literature;[39] however, excessive washing of the particles with ethanol prior to fractionation experiments and re-dispersing the particles in deuterated solvents likely result in decreased surface coverage.

$$\%\, Ligand\ Solvation = \frac{\boldsymbol{SLD_{Shell} - SLD_{tail}}}{\boldsymbol{SLD_{Solv} - SLD_{tail}}} \text{x} 100\% \qquad \textbf{(3.1)}$$

$$\%\, Surface\ Coverage = \frac{A_{head} * \frac{1}{3}\left(r^3{}_{core+shell} - r^3{}_{core}\right)(100\% - \%Ligand\ Solvation)N_A}{r^2{}_{core} V_{molar\_thiol}} \qquad \textbf{(3.2)}$$

The surface coverage results reveal an interesting point not previously considered. The 7.1 ± 1.5 nm and 6.9 ± 1.4 nm silver nanoparticle populations studied are nearly the same size, considering their polydispersity and were isolated at different CO_2 mole fractions. It would seem that the nanoparticle fractionation was unsuccessful based on size alone. The data suggest that the nanoparticles were fractionated both by ligand surface coverage (44% and 55% surface coverage for the 7.1 and 6.9 nm silver nanoparticles respectively) and by size. A low ligand surface coverage would provide less steric hindrance between adjacent dodecanethiol ligands, allowing for tail collapsing/folding and decreased interparticle separation distance. Folded or collapsed

ligands would enable greater interparticle attractive forces, promoting particle precipitation at lower anti-solvent compositions. This demonstrates that surface coverage directly impacts nanoparticle dispersibility and the ability to fractionate nanoparticle populations of similar size based on ligand surface coverage. Conversely, this presents a limit to the degree of monodispersity attainable with an anti-solvent size fractionation when an appreciable distribution in surface coverage exists.

Furthermore, at ambient pressure the ligand shell solvation for the 7.1 nm and 6.9 nm diameter nanoparticles are nearly the same, 19.4% and 18.7% solvated respectively. As the CO_2 mole fraction in the GXL increases, CO_2 functions as an effective anti-solvent for the ligand shell and the ligand solvation decreases. Though more SANS data within the 20% to 35% CO_2 mole fraction range would be beneficial, the data suggests that the ligand solvation decreases at lower CO_2 mole fractions for nanoparticles with lower surface coverage compared to similar sized nanoparticles with higher surface coverage (the 7.1 nm versus the 6.9 nm nanoparticles). Kitchens and coworkers used a collapsed phase interaction energy model (CPM) with varying surface coverage to estimate the ligand length at solvent compositions between 51% and 78% CO_2 for dodecanethiol stabilized silver nanoparticles in gas-expanded hexane to predict the size dependent precipitation.[22,25] The CPM overpredicted the maximum nanoparticle size for silver nanoparticles dispersed at a given solvent condition compared to our SANS results (between 51 and 58% CO_2 mole fraction), but were generally within ~1Å for the measured ligand shell thickness values. The proposed CPM model made assumptions for the percent surface coverage, ligand solvation, and degree of ligand collapse on the

particle surface (i.e. the ligand shell thickness). The data obtained from our SANS experiments provides measurements of both ligand length and ligand solvation for dodecanethiol capped silver nanoparticles dispersed in gas-expanded hexane at varying CO_2 mole fractions. In the future, these results will be used to enhance current interaction energy models to better accommodate the variability in surface coverage, thermodynamic interactions of the solvent with ligands, and the ligand structure, each of which impact the interparticle repulsion terms.

The Role of Curvature and Surface Coverage on Ligand Solvation

The degree of ligand solvation determined by using Equation 3.2, demonstrates a dependence on nanoparticle size/curvature. The 6.6 nm and 5.9 nm nanoparticle dispersions have similar ligand surface coverage (62% and 60%, respectively), despite an 11% difference in curvature (1/radius). Consequently, they can be used to evaluate the effect of curvature alone with the influence of surface coverage. When comparing the 6.6 nm and 5.9 nm dodecanethiol capped silver nanoparticles at 0% CO_2 mole fraction in Figure 3.7, it is evident that higher surface curvature affords greater ligand solvation. Shah et al. modeled silver nanoparticles of varying diameter (3 to 15 nm) capped by dodecanethiol and showed that particles with smaller radii had greater ligand solvation, particularly as the radial distance increases from the surface of the particle to the end of the tail.[24] Our SANS results support the findings of Shah et al.[24] and suggests that higher surface curvature enables solvent molecules to penetrate deeper into the ligand shell, reaching closer to the surface of the nanoparticle while aiding in nanoparticle

dispersibility. Our results along with other studies [1, 28] show that nanoparticles with smaller radii (those particles with higher ligand solvation) are dispersible at larger CO_2 mole fractions. However, the data for the four silver nanoparticle solutions shows that ***both*** surface coverage and surface curvature dictate nanoparticle dispersibility.

The Role of Curvature and Surface Coverage on Ligand Length

Similar to ligand solvation, ligand length is also affected by ligand surface coverage and nanoparticle curvature. Figure 3.8 details the shell thickness values fit from SANS data for the silver nanoparticle populations as a function of CO_2 mole fraction. The dodecanethiol ligand lengths obtained from the core-shell model[35] at ambient pressure ranged from 9.4 and 13.5 Å, increasing with decreasing particle curvature. The shell thicknesses are shorter than reported (15 Å) for dodecanethiol extending from a flat gold surface[40] which is attributed to nanoparticle curvature.[38] The 6.6 nm and 5.9 nm silver particles with comparable percent surface coverage, yielded respective shell thicknesses of 12.3 Å and 9.4 Å at 0 CO_2 mole fraction, demonstrating a 24% decrease in ligand length with an 11% increase in particle curvature. The 6.9 nm and 7.1 nm particles do not provide a direct comparison due to the differences in surface coverage.

Figure 3.8 shows that the shell thickness decreases with increasing pressure from 0 to 60 mol % CO_2 mole fraction, indicating that the alkyl tails move from an extended to a collapsed/folded state measuring ~7 Å for all of the varying sized particles studied. The two largest core-size silver nanoparticles with varying surface coverage and similar surface curvature (7.1 and 6.9 nm) demonstrate an overall 6 Å decrease in ligand length

during the precipitation process. The smaller core diameter silver nanoparticles studied (5.9 nm) demonstrate a 2.6 Å decrease in ligand length during the precipitation process; however, these particles had 60% dodecanethiol surface coverage and greatest surface curvature. Both higher nanoparticle curvature and decreased surface coverage provide lower ligand-to-ligand steric hindrance, enabling higher alkane chain mobility and solvation. The data from the 5.9 nm diameter silver nanoparticles shows that as the CO_2 mole fraction in the GXL increases, the shell thickness decreases by no more than ~1/2 a ligand length. The surface coverage and surface curvature play a competing role in ligand length and nanoparticle dispersibility.

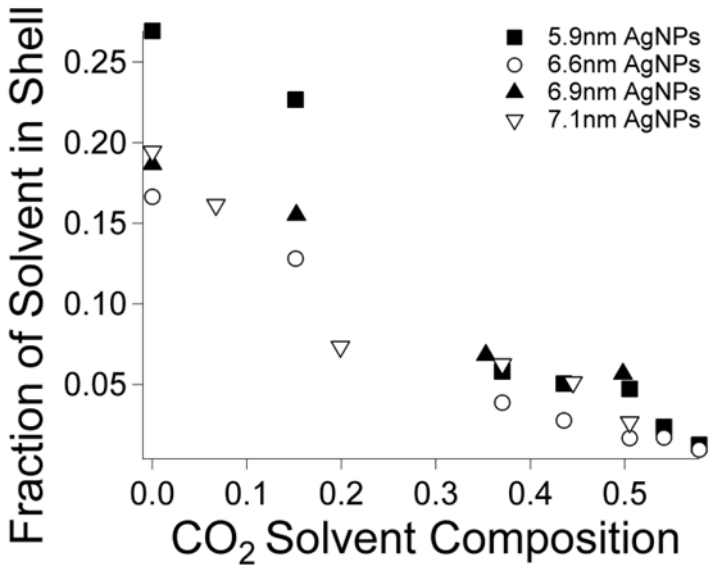

Figure 3.7: Fractional ligand solvation based on the core-shell model for four different silver nanoparticle samples dispersed in a GXL with *n*-hexane-d_{14} as a function of CO_2 mole fraction.

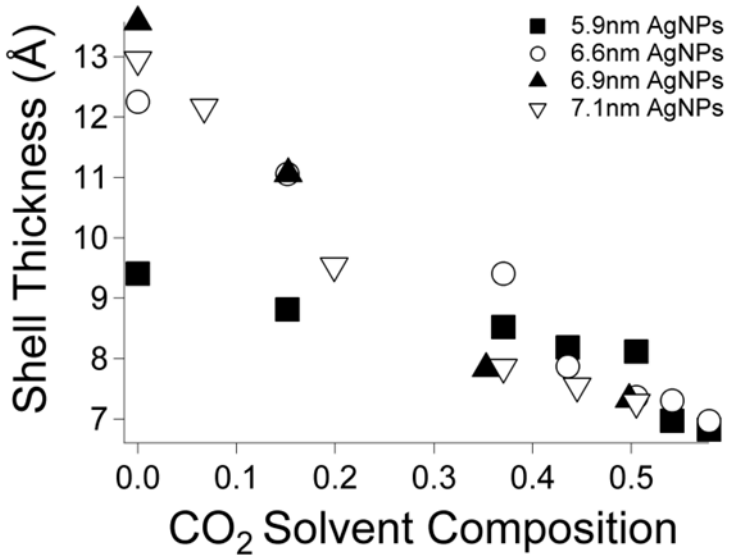

Figure 3.8: Dodecanethiol ligand shell thickness measured with the core-shell model for four different silver nanoparticle samples dispersed in a GXL with n-hexane as a function of CO_2 mole fraction.

The observed nanoparticle ligand behavior under anti-solvent conditions can be conceivably extended to other solvent removal processes (drying). As the solvent is removed from a concentrated dispersion, the stabilizing ligands collapse onto the core of the nanoparticle (extending only ~1/2 a ligand length). Previous studies have depicted ordered self–assembled arrays of nanoparticles prepared by drop casting or spin-coating concentrated solutions of hydrophobically stabilized monodisperse nanoparticles onto substrates where neighbor-to-neighbor distances are on the order of one ligand length.[41] Researchers have proposed that this tight packing is due to ligand interpenetration between neighboring particles.[41] Our results support an alternative mechanism where the nanoparticle ligands primarily collapse/fold onto their core, nearing the shell thickness of 1/2 the fully extended ligand length, which controls the film interparticle separation distance, more so than interpenetrating extended ligands. The end result is precipitated

nanoparticles with neighbor-to-neighbor separation distances on the order of one ligand length.[42]

Conclusions

Wet-chemical synthesis of metal nanoparticles often produces particle diameters ranging from 3 to 8 nm that are polydisperse in size and/or shape.[5] Polydispersity is a drawback for end applications that rely on size and/or shape dependent nanoparticle properties.[7] The GXL fractionation technique provides effective and potentially scalable means to isolate monodisperse populations of particles, offering many benefits over traditional liquid-liquid fractionation techniques, which include and the elimination of large volumes of mixed organic solvent waste and time/energy intensive centrifugation.[1, 28] Nanoparticle dispersibility and thus anti-solvent fractionation is dependent upon the metal type, mean particle size, ligand length, ligand solvation, and bulk solvent properties. SANS was used for in-situ measurement of the mean core diameter, the ligand length, and ligand solvation for dodecanethiol capped silver nanoparticles as a function of CO_2 mole fraction within the CO_2/hexane (GXL) solvent mixture prior to and during the fractionation process. CO_2 is an effective anti-solvent for the nanoparticles and ligands, causing the dodecanethiol ligands to collapse/fold onto the core nanoparticle; collapsing to 1/2 the ligand length of a fully extended dodecanethiol tail at particle precipitation. Ligand solvation data was determined from the SLD_{shell} as a function of the GXL composition, assuming the local solvent composition within the shell is the same as the bulk GXL. The ligand solvation decreases from over 20% to nearly 6%, with increasing CO_2 mole fraction from 17 mol % to 43 mol %. The decreased ligand

solvation coupled with the decreased ligand length, both induced by the CO_2 anti-solvent, create an unfavorable environment for the nanoparticles and promotes reversible size dependent precipitation. It was shown that both curvature and degree of surface coverage play significant roles in ligand solvation and shell thickness, which are deterministic of nanoparticle dispersibility in solution.

Future work will include developing a robust interaction energy model to predict nanoparticle dispersibility in solution as well as other nanoparticle behavior. Because previous results have overestimated the dodecanethiol ligand thickness upon its best solvation, having precise measurements of the ligand length, ligand solvation, and the ligand surface coverage will permit a greater understanding of the thermodynamics behind the dispersibility of these metallic nanostructures in solution. These results can be used in the improvement of current techniques for the synthesis, stabilization, and fractionation of metallic nanoparticles with the expectation of using them to develop novel materials, modeling particle-particle and solvent-ligand interactions, and nanoparticle deposition into ordered arrays using solvent/anti-solvent conditions.

References

(1) Anand, M.; McLeod, M. C.; Bell, P. W.; Roberts, C. B. *J. Phys. Chem. B.* **2005**, *109*, 22852-22859.

(2) Saunders, A. E.; Ghezelbash, A.; Sood, P.; Korgel, B. A. *Langmuir* **2008**, *24*, 9043-9049.

(3) Busbee, B. D.; Obare, S. O.; Murphy, C. J. *Adv. Mater.* **2003**, *15*, 414-416.

(4) Wu, M.; Lai, L. *Colloids Surf. Physicochem. Eng. Aspects* **2004**, *244*, 149-157.

(5) Brust, M.; Walker, M.; Bethell, D.; Schiffrin, D. J.; Whyman, R. *J. Chem. Soc. - Chem. Commun.* **1994**, 801-802.

(6) Liu, J.; Anand, M.; Roberts, C. B. *Langmuir* **2006**, *22*, 3964-3971.

(7) Young Jun Kim; Yoon Seok Yang; Seung-Chul Ha; Cho, S. M.; Yong Shin Kim; Hye Yoon Kim; Yang, H.; Youn Tae Kim *Sens. Actuators*, B **2005**, *106*, 189-98.

(8) Chen, M.; Yamamuro, S.; Farrell, D.; Majetich, S. A. *J. Appl. Phys.* **2003**, *93*, 7551-3.

(9) Saini, G.; Shenoy, D.; Nagesha, D. K.; Kautz, R.; Sridhar, S.; Amiji, M. NSTI Nanotech **2005**, 328-31.

(10) Grassian, V. H. *J. Phys. Chem. C* **2008**, *112*, 18303-18313.

(11) Liu, C.; Zhang, Z. J. *Chem. Mater.* **2001**, *13*, 2092-6.

(12) Baraton, M.; Merhari, L. *Electroceramics VIII* **2002** *24*, 1399-404.

(13) Qi, W. H.; Wang, M. P. *Chem. Phys.***2004**, *88*, 280-4.

(14) Jain, P. K.; Lee, K. S.; El-Sayed, I.; El-Sayed, M. *J. Phys. Chem. B* **2006**, *110*, 7238-48.

(15) Alivisatos, A. P. *Science* **1996**, *271*, 933-7.

(16) Jessop, P. G.; Subramaniam, B. *Chem. Rev.* **2007**, *107*, 2666-2694.

(17) McLeod, M. C.; Anand, M.; Kitchens, C. L.; Roberts, C. B. *Nano Lett.* **2005**, *5*, 461-465.

(18) Anand, M.; Odom, L. A.; Roberts, C. B. *Langmuir* **2007**, *23*, 7338-7343.

(19) Liu, J.; Sutton, J.; Roberts, C. B. *J. Phys. Chem. C* **2007**, *111*, 11566-11576.

(20) Gupta, G.; Shah, P. S.; Zhang, X.; Saunders, A. E.; Korgel, B. A.; Johnston, K. P. *Chem. Maters.* **2005**, *17*, 6728-6738.

(21) Fernandez, C. A.; Bekhazi, J. G.; Hoppes, E. M.; Wiacek, R. J.; Fryxell, G. E.; Bays, J. T.; Warner, M. G.; Wang, C.; Hutchison, J. E.; Addleman, R. S. *Small* **2009**, *5*, 961-969.

(22) Anand, M.; You, S.; Hurst, K. M.; Saunders, S. R.; Kitchens, C. L.; Ashurst, W. R.; Roberts, C. B. *Ind. Eng. Chem. Res.* **2008**, *47*, 553-559.

(23) Vincent, B.; Luckham, P. F.; Waite, F. A. *J. Colloid Interface Sci.* **1980**, *73*, 508-521.

(24) Shah, P. S.; Holmes, J. D.; Johnston, K. P.; Korgel, B. A. *J. Phys. Chem. B* **2002**, *106*, 2545-51.

(25) Kitchens, C. L.; Roberts, C. B.; Juncheng, L.; Robert, A. W.; Madhu, A.; Von, W. G.; Hurst, K. M.; Saunders, S. R. In *Application of Gas-Expanded Liquids for Nanoparticle Processing: Experiment and Theory;* Gas-Expanded Liquids and Near-Critical Media; American Chemical Society: Washington, DC, 2009; pp 290-308.

(26) Kitchens, C. L.; McLeod, M. C.; Roberts, C. B. *J. Phys. Chem. B* **2003**, *107*, 11331-11338.

(27) Abramoff, M. D.; Magalhaes, P. J.; Ram, S. J. *J. Biophoton Int.* **2004**, *11*, 36-41.

(28) McLeod, M. C.; Anand, M.; Kitchens, C. L.; Roberts, C. B. *Nano Lett.* **2005**, *5*, 461-5.

(29) Glinka, C. J.; Barker, J. G.; Hammouda, B.; Krueger, S.; Moyer, J. J.; Orts, W. J. *J.Appl. Crystallogr.* **1998**, *31*, 430-45.

(30) Kline, S. R. *J. Appl. Crystallogr.* **2006**, *39*, 895-900.

(31) Patel, N. C.; Teja, A. S. *Chem. Eng. Sci.* **1982**, *37*, 463-473.

(32) Cuadros, F.; Faúndez, C. A.; Renuncio, J. A. R.; Mulero, A. *Thermochim. Acta* **2002**, *389*, 167-177.

(33) Ohgaki, K.; Katayama, T. *J. Chem. Eng. Data* **1976**, *21*, 53-55.

(34) Munter, A. Scattering Length Density Calculator. *http://www.ncnr.nist.gov/resources/sldcalc.html* (accessed 12/28, 2009).

(35) Rice, S. A. *J. Polym. Sci.***1956**, *19*, 594.

(36) Bartlett, P.; Ottewill, R. H. *J. Chem. Phys.* **1992**, *96*, 3306-3318.

(37) Butter, K.; Hoell, A.; Wiedenmann, A.; Petukhov, A. V.; Vroege, G. *J. Appl. Crystallogr.* **2004**, *37*, 847-56.

(38) Korgel, B. A.; Fitzmaurice, D. *Phys. Rev. B: Condens. Matter* **1999**, *59*, 14191-201.

(39) Korgel, B. A.; Fullam, S.; Connolly, S.; Fitzmaurice, D. *J. Phys. Chem. B* **1998**, *102*, 8379-88.

(40) Porter, M. D.; Bright, T. B.; Allara, D. L.; Chidsey, C. E. D. *J. Am. Chem. Soc.* **1987**, *109*, 3559-68.

(41) Harfenist, S. A.; Wang, Z. L.; Alvarez, M. M.; Vezmar, I.; Whetten, R. L. *J. Phys. Chem.* **1996**, *100*, 13904-10.

(42) Terrill, R. H.; Postlethwaite, T. A.; Chen, C.; Poon, C.; Terzis, A.; Chen, A.; Hutchison, J. E.; Clark, M. R.; Wignall, G.; Londono, J. D.; Superfine, R.; Falvo, M.; Johnson Jr., C. S.; Samulski, E. T.; Murray, R. W. *J. Am. Chem. Soc.* **1995**, *117*, 12537-12548.

CHAPTER FOUR

FRACTIONATION OF SURFACE-MODIFIED GOLD NANORODS USING GAS-EXPANDED LIQUIDS

Introduction

Gold nanorods (GNRs) have unique size- and aspect ratio-dependent properties[1-3] which are ideal for sensing and electronic applications,[4] as well as biomedical contrast agents.[5] GNRs are also efficient at transforming absorbed radiation energy into heat (photothermal activity)[6, 7] making them useful in nanomedicine as hyperthermia agents. The long length, stiffness, and aspect ratios of rod shaped particles make GNRs ideal filler materials for polymers.[8] The incorporation of GNRs into polymer matrices would be highly advantageous due to the unique photothermal, electronic, and plasmonic properties and may potentially create a new class of nanomaterials.[9] However, most synthetic polymers are hydrophobic, including polyethylene, polypropylene, polystyrene, and polylactic acid. Unfortunately, GNR applications which require hydrophobic environments are limited because there are no high yield synthesis procedures which produce them.

Cetyltrimethylammonium bromide (CTAB) is the most widely used shape-directing cationic surfactant employed for the synthesis of non-spherical gold nanoparticles, in particular GNRs.[3, 10-12] Albeit CTAB is known to be toxic, tailoring the synthesis conditions affords high yields of hydrophilic GNRs with minimal growth of spherical and non-rod shaped nanoparticles.[2, 12] Hence, post-synthesis processing must be employed to lower toxicity and facilitate surface modification,[13] either by removal of

CTAB or encapsulation.[14] Removal of excess CTAB dispersed in solution is trivial and can be achieved by centrifugation and redispersion in neat solvent (water).[7, 13] Removal of CTAB bound to the nanorod surface, without compromising the GNR stability, is a far more daunting task, and is often circumvented by polymer encapsulation.[14] The CTAB bilayer provides steric hindrance and electrostatic repulsion forces which hinder the attractive forces between GNRs, and thus excessive removal can lead to irreversible aggregation due to the large van der Waals attractive forces. A significant barrier to hydrophobization of GNRs is maintaining sufficient repulsive forces during the surface modification process, preventing irreversible agglomeration.

Few researchers have successfully dispersed GNRs in organic solvents (chloroform, toluene, *n*-hexane, etc.).[1, 14-16] Recently, Chandran et al. used a seed-mediated process to synthesize GNRs in toluene.[15] Hydrophobic amines were used as phase transfer catalysts for gold ions and 6.1 nm seed nanoparticles, and also functioned as the reducing and stabilizing agents. By varying the synthesis conditions, size-control was achieved for aspect ratios up to 11. However, large spheres and other irregular shapes were synthesized in addition to GNRs. In this case, post-synthesis processing would be required to isolate the GNRs. Surface modification of aqueous dispersions is an alternative approach to obtain hydrophobically stabilized GNRs. Pastoriza-Santos et al. used a layer-by-layer technique to coat CTAB stabilized GNRs with a silica shell (varying thicknesses ranging between 12 to 58 nm) enabling their resuspension in chloroform;[14] however, the silica shell thicknesses demonstrated in this work are large and may lower some of the effects of the desirable characteristics produced by GNRs, for

example refractive index dependent plasmon resonance or photothermal activity. Mitamura et al. hydrophobized GNRs using 3-mercaptopropyltrimethoxysilane (MPS) and subsequent tethering to octadecyltrimethoxysilane (ODS) through the hydrolysis of the Si-OR groups.[16] This procedure is highly useful because it demonstrates a simple and successful approach to the hydrophobization of CTAB capped GNRs, with minimal changes to ligand shell thickness. Surface modification of GNRs is advantageous due to the demonstrated higher yield and monodispersity of GNRs produced; however, any undesired seed or other shaped nanoparticles will also be modified and resuspended with the dispersion. Hence, fractionation of hydrophobically stabilized GNRs in a tunable system will enhance the properties of the dispersion by minimizing the presence of seed nanoparticles, large spheres, or other shapes present.

Gas-expanded liquids (GXLs) are a class of pressure-tunable solvents used for a variety of processes, including extraction, separations, and even nanoparticle synthesis and size-selective fractionation.[17, 18] Carbon dioxide is the primary gas employed in GXL processes due to the high solubility in organic solvents. When CO_2 is added to an organic solvent, the mole fraction of CO_2 increases in the liquid phase (dependent on the CO_2 partial pressure) and simultaneously causes the liquid phase volume to expand.[17] CO_2 has been shown to be an effective anti-solvent for hydrophobic nanoparticles dispersed in non-polar solvents, enabling size-selective precipitation of alkanethiol–modified, sub 10 nm spherical nanoparticles of gold,[19-21] silver,[19, 22] and platinum.[23] Once precipitated, the nanoparticles can be redispersed in neat solvent for later use. The GXL technique is ideal for nanoparticle isolation compared to recursive liquid-liquid solvent/anti-solvent

techniques (ex. ethanol/chloroform) because it minimizes the quantity of mixed solvent waste and eliminates time-intensive centrifugation because of the enhanced transport properties.[24] Moreover, the GXL technique enables recycle of neat organic solvents and gases employed during nanoparticle isolation.[18] In this work, we use an adapted procedure developed by Mitamura et al.[25] to hydrophobize CTAB capped GNRs and resuspend them in various organic solvents. We investigate the dispersibility of GNRs in varying CO_2-expanded solvents, including cyclohexane, toluene, and *n*-hexane. This work also investigates the impact varying chain length has on GNR dispersibility in CO_2-expanded toluene. This work demonstrates that GNRs stabilized by 18 carbon long ligands are dispersible in cyclohexane, toluene, and *n*-hexane up to CO_2 pressures of 400 psi, 350 psi, and 250 psi, respectively. GNRs stabilized by 12 carbon long chains proved to have greater dispersibility, and precipitated at 525 psi in CO_2-expanded toluene. We also present the first ever GNR fractionation using GXLs—this demonstrated an improvement in GNR monodispersity and decreased the excess seed concentration by 73%. These results will directly impact future GNR application by providing tunable means to minimize polydispersity, and gives evidence that GXL processing may be performed on other non-spherical particles.

Experimental Methods

Materials

The metal precursors hydrogen tetrachloroaurate (III) trihydrate ($HAuCl_4 \cdot 3H_2O$, 99.99%) and silver nitrate (AgNO3, 99.995%) were purchased from VWR. The stabilizing agents

cetyltrimethylammonium bromide (CTAB, 99%), 1-dodecanethiol (98%) and 1-octadecanethiol (90%), and the reducing agents sodium borohydride ($NaBH_4$, 98%) and ascorbic acid (AA, 99%) were purchased from VWR. ACS grade ethanol (95%), toluene (99.7%), *n*-hexane (95%), and cyclohexane (99%) were purchased by VWR. 3-Mercaptopropyltrimethoxysilane (MPS, 99%), *n*-octadecyltrimethoxysilane (ODS, 95%), and dodecyltrimethoxysilane (DDS) were purchased from Gelest Inc. The Coleman Grade CO2 was purchased from National Welders (99.99%).

Synthesis of GNRs

The GNR synthesis was adapted from a seed-mediated growth procedure by Sau et al.[10] Gold seed nanoparticles were prepared by adding 0.25 mL of 0.01 M $HAuCl_4$ to 7.5 mL solution of 0.1 M CTAB (maintained at 27 °C). Next, 600 μL of 0.01 M $NaBH_4$ (ice cold) was added to the CTAB/gold salt mixture yielding seed nanoparticles. All seeds employed for GNR synthesis were incubated at 27 °C and used within 3 hours of initial preparation. 5.0 mL of 0.01 M $HAuCl_4$ and 0.75 mL of 0.01 M $AgNO_3$ were added to 118.75 mL of 0.1 M CTAB solution. Ascorbic acid (0.80 mL of 0.1 M) was then added to the metal salt solution, changing the color from yellow/orange to clear. The solution was incubated at 27 °C for 10 min, followed by the addition of 0.50 mL of gold seed nanoparticle solution with gentle mixing for ~20 sec. After 3 to 5 min, the clear solution turned purple indicating the presence of GNRs. The GNRs were incubated at 27 °C for at least 3 hours, allowing their complete growth. The GNRs were centrifuged at 14,500 rpm for 10 min yielding a dark pellet at the bottom of the centrifuge

tube. The supernatant solution (containing excess CTAB) was decanted, and the GNR pellet was redispersed in deionized water. The purification process was performed twice. Further CTAB extraction was employed by mixing GNRs with chloroform (2:1 GNRs to chloroform by volume) for 5 min, followed by isolation of the aqueous GNR dispersion. Figure 4.1 shows a representative TEM image of the purified CTAB capped GNRs (aspect ratio = 3.2 ± 0.8, length = 40.1 ± 10.3 nm, width = 14.4 ± 4.0 nm).

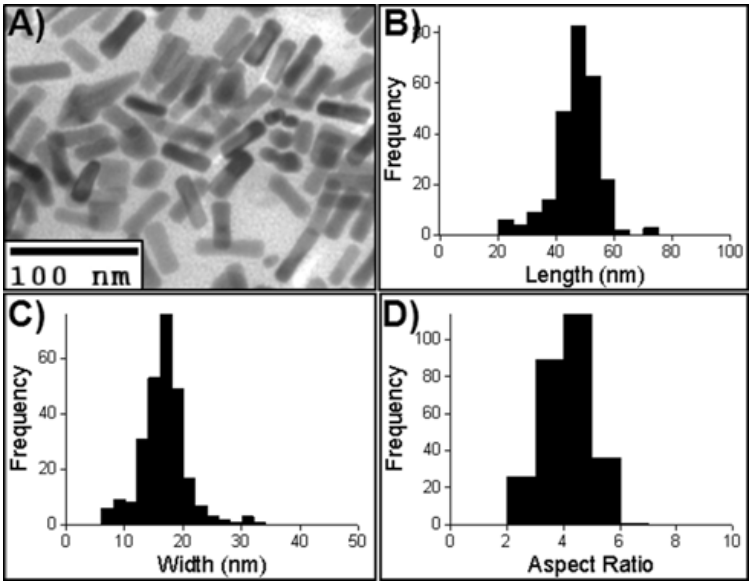

Figure 4.1: A) TEM image of gold nanorods stabilized by cetyltrimethylammonium bromide and respective histograms of B) length (40.1 ± 10.3 nm), C) width (14.4 ± 4.0 nm), and D) aspect ratio (3.2 ± 0.8).

Surface Modification of GNRs

The surface modification process which enabled the CTAB stabilized GNRs to be redispersed in toluene, was adapted from the work previously presented by Mitamura et al.[16] In short, 0.30 mL of 0.02 M MPS in ethanol was added to 30.0 mL of aqueous GNRs followed by vigorous mixing for at least 30 min. Next, 15.0 mL of 0.02M ODS in

chloroform was added creating a biphasic mixture, followed by 0.30 mL of 1M NaOH with vigorous mixing. The biphasic system was mixed vigorously using a magnetic stir bar for at least 4 hours, enabling adequate surface modification. After mixing, the deep purple color transferred from the upper aqueous phase to the lower chloroform phase. The ODS stabilized GNRs were removed from the biphasic mixture, followed by the addition 1 mL of 0.01 M octadecanethiol in chloroform, functioning as a co-stabilizing ligand. GNR dispersions prepared without the addition of a co-stabilizing agent (alkanethiol) demonstrated mild oxidation and a decrease in GNR concentration during water purification and inhibited redispersion after ethanol purification during centrifugation.

The octadecanethiol/ODS stabilized GNRs were washed by adding 15.0 mL of water and vortex mixing for ~ 30 sec. The cloudy white supernatant containing water soluble ligands was removed, and the process was repeated. Next the GNR solution was diluted with ethanol (2:1 ratio ethanol to GNRs) and centrifuged at 5,000 rpms for 5 min to precipitate the GNRs and decant any excess dispersing ligands. The precipitated GNRs were dried with nitrogen and resuspended in neat solvent (cyclohexane, toluene, or *n*-hexane). The stable dispersion of GNRs was sonicated for 5 min. GNRs were also stabilized with DDS and dodecanethiol co-stabilizing ligand, replacing ODS and octadecanethiol during modification. Figure 4.2 shows a TEM image and respective histograms of the length, width, and aspect ratios of the octadecanethiol/ODS stabilized GNRs.

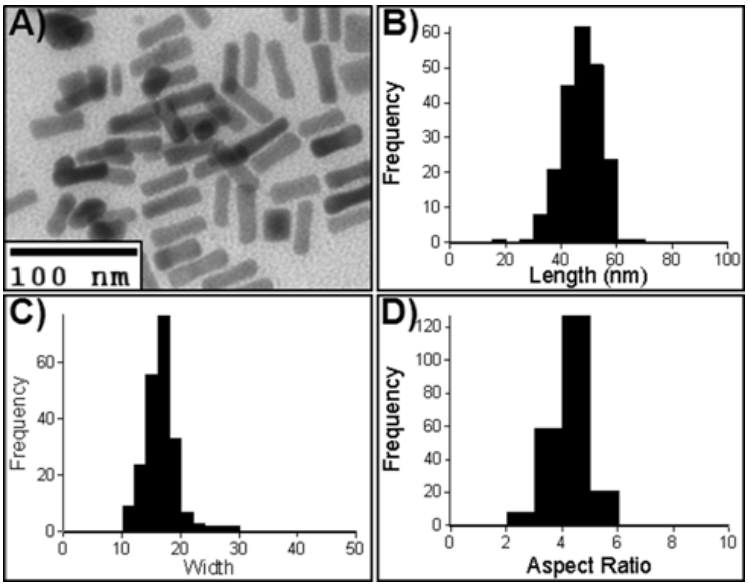

Figure 4.2: A) TEM image of gold nanorods stabilized by octadecanethiol/ODS and respective histograms of B) length (42.1 ± 6.8 nm), C) width (14.7 ± 2.9 nm), and D) aspect ratio (3.3 ± 0.6).

Characterization

Ultraviolet-visible (UV-VIS) Light Spectroscopy of GNRs in GXLs

UV-VIS spectroscopy of GNRs dispersed in GXLs was performed on a Varian Cary 50 spectrophotometer. The sample cell used during experimentation is a custom stainless steel pressure cell equipped with two sapphire windows (12.7 mm thick/windows, 15.75 mm total path length), a pressure transducer, and an inlet valve for CO_2 addition/removal. Neat solvent (toluene, *n*-hexane, or cyclohexane) was used for baseline correction of all UV-VIS spectra. For each experiment, 4 mL of GNR dispersion was added to the pressure cell prior to pressurization. CO_2 was delivered to the cell under pressure using a Teledyne Isco 500 HP syringe pump. Spectra were

collected 20 to 30 minutes after pressurization, allowing the system to reach equilibrium pressure and a constant UV-VIS absorbance.

Analysis of the UV-VIS spectra for GNRs in GXLs requires a correction for volume expansion due to increased CO_2 pressure.[19] The volume expansion coefficients, V/V_o, were calculated for predetermined CO_2 pressures in toluene, cyclohexane, and *n*-hexane using the Patel-Teja equation of state (PT-EOS).[26] The PT-EOS was chosen because it allows for adjustability of the critical compressibility factor, and experimental/modeling data are available for comparison.[26-28] All UV-VIS spectra were corrected for volume expansion using the calculated volume expansion coefficients or a polynomial trend line fit to the calculated coefficients for pressures not calculated initially.

The acentric factor and critical properties (ω, P_c, T_c, Z_c) for CO_2 (0.707, 73.8 bar, 304.1 K, 0.309),[29] toluene (0.262, 591.8 K, 41.06 bar, 0.264),[30] *n*-hexane (0.225, 507.6 K, 30.25 bar, 0.266),[29] and cyclohexane (0.210, 553.6 K, 40.73 bar, 0.273)[31] were readily found in the literature and used to determine the volume expansion coefficients. The binary interaction parameters (k_{ij}, l_{ij}) used in the PT-EOS were also obtained from literature for CO_2-toluene (0.090, 0.000), CO_2-*n*-hexane (0.138, 0.074), [29] and CO_2-cyclohexane (0.007404, -0.1710).[32] The calculated volume expansion coefficients determined from the PT-EOS compare well to previously published results. Figure 4.3 shows the PT-EOS predicted volume expansion coefficients compared to experimental data measured at 25 °C for CO_2 in toluene[30] and *n*-hexane;[31] no experimental data for CO_2 in cyclohexane was found in the literature for comparison.

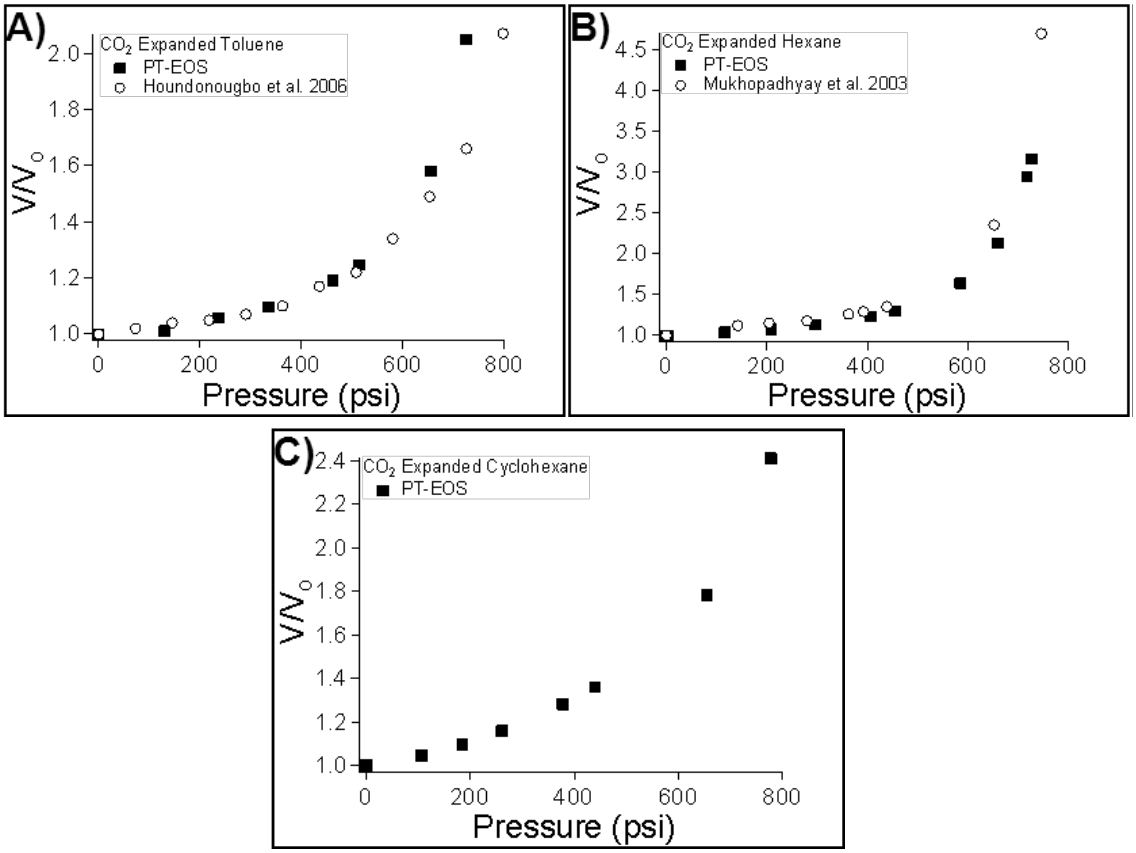

Figure 4.3: Calculated volume expansion coefficients (V/V_o) determined using the Patel-Teja Equation of state for CO_2-expanded A) toluene[a], B) *n*-hexane[b], and C) cyclohexane at 25 °C.
[a, b]The volume expansion coefficients for CO_2-expanded toluene are compared to the experimental work presented by Houndonougbo et al.[30] and Mukhopadhyay et al.[31] respectively measured at 25 °C.

Transmission Electron Microscopy (TEM)

A Hitachi 7600 TEM was used with an accelerating voltage of 120 kV to obtain images. Samples were prepared by drop casting ~5 μL of nanoparticle dispersion onto a 300 mesh formvar carbon coated copper TEM grid (Ted Pella), followed by solvent evaporation. Size distributions were determined using the ImageJ software package.[33] Nearly 300 GNRs were counted for each sample in order to obtain meaningful statistics.

GNR Isolation using CO_2-Expanded Toluene

The GNRs were precipitated using the gas-expanded liquid (GXL) technique previously demonstrated by McLeod et al. for spherical nanoparticles.[34] A cylindrical glass rod with a spiral groove was placed inside of a custom stainless steel pressure vessel (rod shaped) in order to fractionate the GNRs using the pressure tunable properties of the GXLs (see Figure 4.4, same apparatus used in Chapter 3).[29] Prior to GNR isolation, 1 mL of toluene was added to the pressure vessel to prevent solvent evaporation during fractionation. Next, 0.2 mL of toluene dispersed GNRs were placed in the first spiral rung of the glass rod and the vessel was sealed. Five different populations of GNRs were isolated at varying conditions. Table 4.1 shows the isolation pressures, average length, width, aspect ratio, and volume of the GNRs from each population.

Octadecanethiol/ODS modified GNRs were isolated by initially pressurizing the vessel to 100 psi and then allowing the sample to reach equilibrium (20 min). Next, the cylindrical glass rod was rotated 270° (1.5 turns). This rotation enabled the first fraction of precipitated GNRs to remain in the first rung of the rod and transfer of the dispersed GNRs to a rung further up the rod. More CO_2 was added until the pressure reached 150 psi and remained constant for 20 min (isolating the second fraction of GNRs between 100 and 150 psi). Subsequently, the glass rod was rotated 270° and the cell was depressurized at a constant rate of ~15 psi/min. The first and second fraction of GNRs were collected by toluene addition, gentle agitation, and then removed from the glass rod

using a pipette. The precipitation process was repeated producing GNRs isolated at A) 100 psi and lower, B) 100 to 150 psi, C) 150 to 200 psi, and D) 250 to 300 psi.

Table 4.1: Average length, width, aspect ratio, and volume of octadecanethiol/ODS stabilized GNRs obtained at varying isolation conditions in CO_2-expanded toluene. The standard deviations for length, width, and aspect ratio are also shown.

fraction, (psi)	length (nm)	width (nm)	volume (nm^3)	aspect ratio
-	42.1 ± 6.8	14.7 ± 2.9	7145	3.3 ± 0.6
100 <	43.6 ± 8.4	14.6 ± 2.9	7299	3.3 ± 0.6
100 to 150	40.7 ± 11.0	14.2 ± 3.7	6446	3.3 ± 0.7
150 to 200	39.9 ± 11.5	13.7 ± 4.1	5882	3.3 ± 0.7
250 to 300	38.4 ± 14.5	13.8 ± 4.8	5744	3.1 ± 0.7

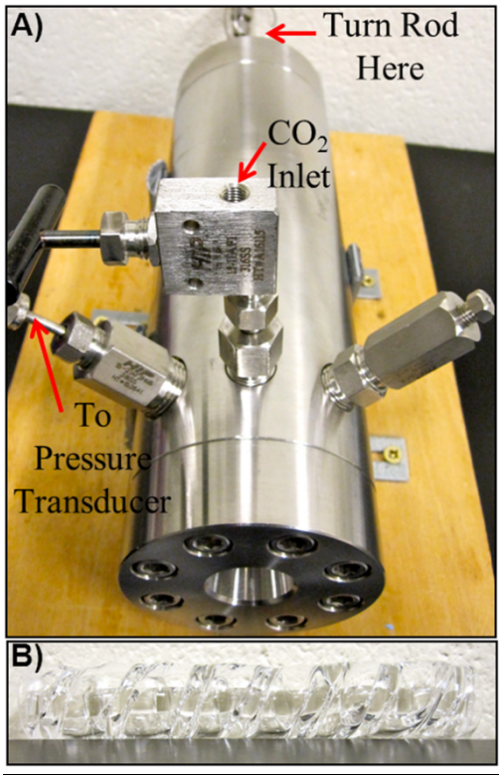

Figure 4.4: The A) pressure cell and B) glass spiral rod used for GNR fractionation using gas-expanded toluene.

Results and Discussion

Volume Expansion of GXLs

Figure 4.5A shows the UV-VIS spectra for octadecanethiol/ODS modified GNRs dispersed in CO_2-expanded toluene with varying pressure. The UV-VIS absorbance decreases with increasing pressure, demonstrating that GNRs precipitate as a result of the CO_2 anti-solvent behavior. Figure 4.5B shows the normalized nanorod absorbance maximum with varying pressure. The octadecanethiol/ODS modified GNRs begin to precipitate near 75 psi (the precipitation point was determined to be the pressure at which the normalized absorbance was equivalent to ~0.9) and are completely precipitated out of solution at 350 psi. Comparatively, CO_2 pressures exceeding 700 psi did not precipitate octadecanethiol stabilized gold nanoparticles (~4 nm) out of toluene (results not presented here for brevity). It is expected that the GNRs will precipitate at lower pressures than small spherical nanoparticles due to their larger van der Waals attractive forces.

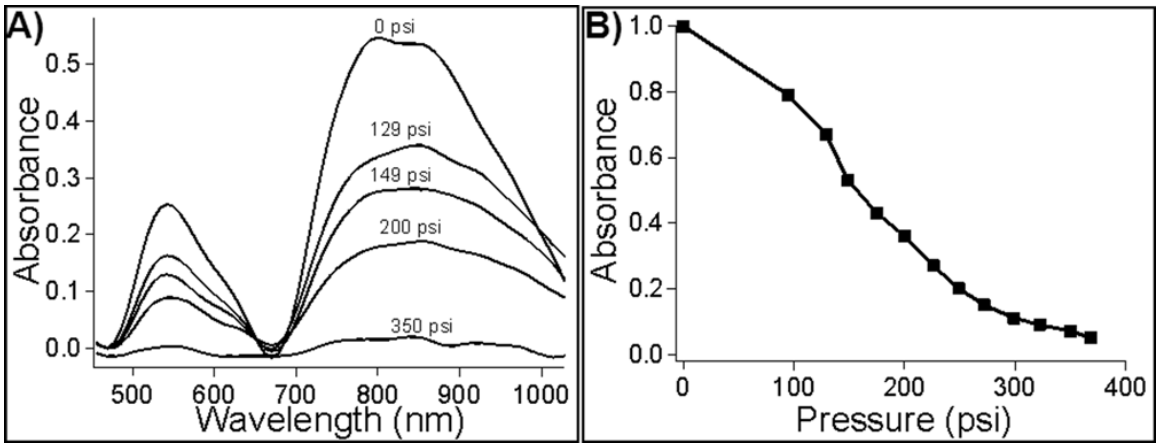

Figure 4.5: A) UV-VIS spectra for ODS/octadecanethiol modified GNRs dispersed in CO_2-expanded toluene with varying pressure. B) Normalized maximum UV-VIS absorbance with varying CO_2 pressure in toluene. All UV-VIS spectra were corrected for dilution effects using the volume expansion coefficients determined with the Patel-Teja equation of state.

Effect of Ligand Length on GNR Dispersibility

Nanoparticle dispersibility is tunable by varying the stabilizing ligand length.[19, 35] The nanoparticle ligands contribute to the steric repulsive forces which mediate particle-particle attraction forces in solution and provide favorable interactions with the solvent (osmotic repulsive forces due to solvation).[36] Anand et al. demonstrated that hexanethiol, octanethiol, and tetradecanethiol modified silver nanoparticles precipitate at lower pressures than dodecanethiol; though in general, increases in ligand length showed increased nanoparticle dispersibility in poor solvent conditions. Dodecanethiol has been suggested to be an "optimum" ligand length[19] for spherical nanoparticles, both for increased nanoparticle dispersibility and deposition into thin films and ordered arrays.[20, 37] Analogously, Chapter 2 demonstrated liquid anti-solvent precipitation (ethanol/toluene

and ethanol/hexane as the poor/good solvent pairs) to isolate octadecanethiol and dodecanethiol stabilized gold nanoparticles (~ 4 nm). The octadecanethiol stabilized gold nanoparticles were precipitated at a lower ethanol volume fraction compared to those which were dodecanethiol stabilized.

The dispersibility of GNRs in GXL systems has not been previously investigated. Hence, we have varied the stabilizing ligand length (octadecanethiol/ODS or dodecanethiol/DDS) in order to develop a better fundamental understanding of GNR dispersibility. Figure 4.6 shows the normalized maximum absorbance values of dodecanethiol/DDS and octadecanethiol/ODS stabilized GNRs in CO_2-expanded toluene. The octadecanethiol/ODS stabilized GNRs began to precipitate at 100 psi and completely precipitated out of solution at 350 psi. The shorter dodecanethiol/DDS stabilized GNRs began precipitating out of solution at 150 psi and remained stabilized until 525 psi. Previous small-angle neutron scattering (SANS) investigations have demonstrated that the ligand lengths of hydrophobically modified nanoparticles decrease with increasing anti-solvent composition, thus directly impacting their dispersibility.[29] The ligand shell collapse and decreased ligand solvation resulting from increased anti-solvent conditions induce GNR precipitation.

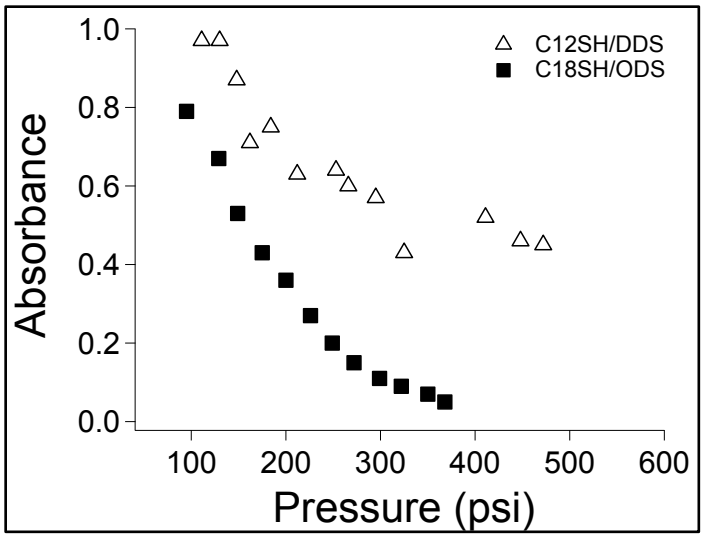

Figure 4.6: UV-VIS spectra for GNRs stabilized with varying ligands dispersed in CO_2-expanded toluene at varying pressure. All UV-VIS spectra were corrected for dilution effects using the volume expansion coefficients determined with the Patel-Teja equation of state.

Effect of Solvent on GNR Precipitation

Tuning the solvent properties by varying temperature,[38] adding a liquid co-solvent,[39] or increasing the mole fraction of a dissolved gas[40] has been shown to alter the threshold nanoparticle size dispersed or synthesized at defined solvent conditions. Kitchens et al. showed that tailoring the synthesis conditions (temperature and pressure) of microemulsions, the mean core-diameter of AOT stabilized copper nanoparticles could be readily controlled.[38] Anand et al. showed that by increasing the solvent alkane length (ranging from 5 to 8 carbons long), dodecanethiol stabilized gold nanoparticle dispersibility was increased, shifting the precipitation conditions to higher CO_2 pressures.[19] Here we investigate dispersibility of GNRs in three different CO_2-expanded solvents (cyclohexane, toluene, and *n*-hexane) that are expected to have favorable solvent-ligand interactions with the GNRs. Figure 4.7 shows the normalized UV-VIS

absorbance values for octadecanethiol/ODS stabilized GNRs in varying CO_2-expanded solvents. As the applied CO_2 pressure increases on the organic solvent, the GNRs precipitate out of solution. The GNRs demonstrated the greatest dispersibility in cyclohexane, where the first signs of precipitation begin around 100 psi and all particles are precipitated at 400 psi. GNR precipitation from CO_2-expanded toluene begins at 100 psi and is complete at 350 psi. Increased CO_2 pressure in *n*-hexane has been shown to enable precipitation of sub 10 nm gold nanoparticles;[19, 21] expectedly, this GXL mixture demonstrated the poorest solvation for the GNRs. GNR precipitation began at 50 psi and all nanoparticles were precipitated out of solution near 250 psi.

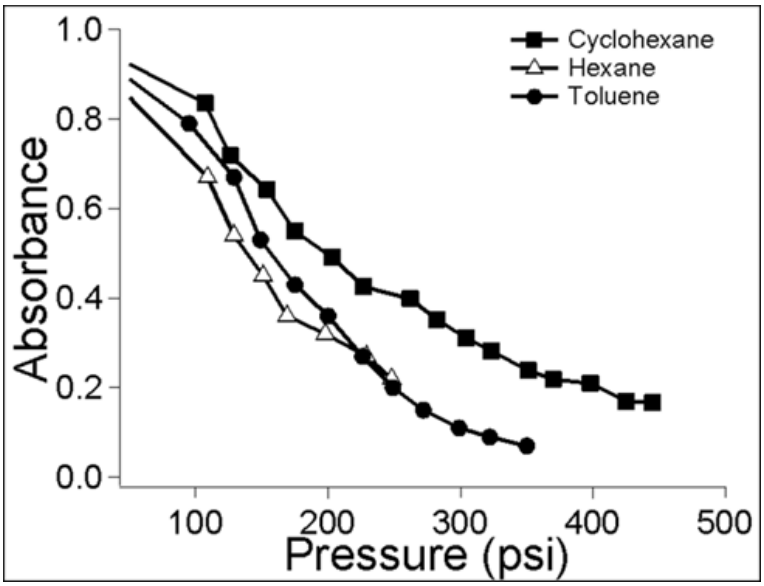

Figure 4.7: UV-VIS spectra for ODS/octadecanethiol modified GNRs dispersed in varying CO_2-expanded solvents at varying pressure. All UV-VIS spectra were corrected for dilution effects using the volume expansion coefficients determined with the Patel-Teja equation of state.

GNR Fractionation with Varying Pressure Conditions

During the wet-chemical seed mediated GNR synthesis, the conversion of seeds to GNRs is inevitably less than 100%. Moreover, large spherical gold nanoparticles are often formed during the growth stage of GNR synthesis. Optimization of the synthesis conditions (generally limited to shorter aspect ratio nanoparticles) can minimize the presence of the spherical nanoparticles.[10] Minimizing GNR polydispersity can be controlled by post-synthesis purification steps which involve recursive centrifugation; however, this process is time intensive and volumes are limited to the restrictions in size of the centrifuge tubes.[41]

This study demonstrates the use of GXLs[21, 22] to fractionate polydisperse populations of hydrophobically stabilized GNR solutions (containing gold seeds, spheres, and GNRs) into more monodisperse populations of particles. Interaction energy modeling predicts that the largest nanoparticles (those with the greatest van der Waals attractive forces) should precipitate at lower anti-solvent conditions.[36, 40, 42] Hence, the largest nanoparticles dispersed in solution (based on volume or mass) in the octadecanethiol/ODS stabilized GNR dispersions should precipitate out of the solvent prior to the smallest. In order to demonstrate a fractionation, the synthesis employed to obtain GNRs was not optimized to achieve maximum uniformity in shape, but was tuned to yield large volumes of GNRs (i.e. excess seed particles and large spheres were present in the sample). More uniform shape-distributions of GNRs are achievable if NaCl is added during synthesis (NaCl concentrations typically vary between 1 to 4 times the quantity of gold salt employed in the growth solution).[2]

Figure 4.8 shows TEM images of octadecanethiol/ODS stabilized GNRs isolated at A) 0 psi, B) 100 psi and lower, C) between 100 and 150 psi, and D) between 250 and 300 psi using CO_2-expanded toluene. TEM image analysis showed that the GNRs which were not fractionated had an average aspect ratio of 3.3 ± 0.6, length of 42.1 ± 6.8 nm, and width of 14.7 ± 2.9 nm. The large spherical gold nanoparticles were measured to be 27.8 ± 7.2 nm in diameter. We assumed that the GNRs have a circular cross section (volume = $\pi*l*(w/2)^2$, nm^3) for simplicity, and then calculated their volumes. The GNR volumes are presented instead of their aspect ratios (length/width) because of the polydispersity within both axial directions.

Figure 4.9 shows a bar graph for the calculated volumes of ODS/octadecanethiol modified GNRs which were precipitated at varying pressure conditions from CO_2-expanded toluene. The mean volume of GNRs which were not fractionated was calculated to be 7,145 nm^3, and the large spherical particles had a volume of 11,249 nm^3. Fractionation of the largest nanoparticles was achieved by precipitation at 100 psi and lower, yielding an average volume of 7,299 nm^3 for GNRs and 11,994 nm^3 for the large spheres. Increasing the isolation pressure while maintaining a constant change in pressure (ΔP = 50 psi), demonstrates the fractionation of GNRs. Between 100 to 150 psi, 150 to 200 psi, and 250 to 300 psi the mean GNR volume was determined to be 6,446 nm^3, 5,882 nm^3, and 5,744 nm^3, respectively—showing a decreasing trend with increasing pressure. Likewise, a decrease in both length and width is observed by increasing the isolation pressures (see Figures 4.9B-C).

Calculation of the 95% confidence interval (see error bars in Figure 4.9A-C) demonstrates significant statistical difference among the mean volumes of GNRs isolated at several different CO_2 pressures. The 95% confidence interval for the GNRs which were not fractionated do not overlap with the GNRs isolated between 150 and 200 psi, as well as those isolated between 250 and 300 psi—thus demonstrating the volumes of GNRs in those fractions are different. Additionally, GNRs precipitated below 100 psi proved to be statistically different from the GNRs isolated between 150 and 200 psi, as well as those precipitated between 250 to 300 psi. Although the monodispersity of the GNRs increases during the fractionation process, polydispersity still remains within the length and width dimensions of the GNRs (see Figure 4.9B-C). Hence, the 95% confidence intervals for adjacent isolation pressures (eg. comparing fractions isolated between 100 and 150 psi with those isolated between 150 and 200 psi) do not show a significant difference.

The GNR fractionation employed also demonstrates an improvement in the frequency of spherical seed nanoparticles present in solution. The separation of GNRs from seed nanoparticles is more evident than separation of the large spherical nanoparticles from GNRs due to the greater disparity in overall particle volume. The seed nanoparticles were determined to be 4.3 ± 1.1 nm in diameter (volume ~ 41 nm^3). The GNRs which were not fractionated had a seed concentration of 15% by volume (determined from TEM analysis). The nanoparticle dispersion isolated at 100 psi showed a 73% improvement, containing as little as 4% seeds. As the isolation pressures were increased for fractionation between 100 and 150 psi, the GNR dispersion contained 7%

seed nanoparticles. Fractionation between 150 and 200 psi showed a significant increase in the concentration of seed nanoparticles, reaching 27%. As expected, the smaller size gold nanoparticles remain dispersed in solution at pressures greater than larger GNRs or large spherical nanoparticles. Albeit the GNR fractionation and shape separation was not 100% effective, this work demonstrates a tunable process for GNR purification. The efficiency of this process may be explained by an averaging effect between nanoparticle interactions, hence why a low concentration of excess seeds precipitated at lower CO_2 pressures.[43] Recursive fractionations using either liquid-liquid[44] or GXLs[19, 21] have shown significant improvements, ultimately increasing the monodispersity of the nanoparticle dispersion and may be beneficial in future GNR processing studies. For example, McLeod et al.[34] and Kitchens and coworkers[18] employed the GXL technique at different isolation pressure increments, including $\Delta P = 50$ psi and 25 psi for dodecanethiol stabilized silver nanoparticles. The smaller step in pressure, i.e. 25 psi compared to 50 psi facilitated more efficient nanoparticle fractionation. Comparatively, the use of a co-solvent in addition to cyclohexane, toluene, or hexane may also enhance the selectivity of the GNR fractionation process. Saunders et al. recently demonstrated greater size selectivity of dodecanethiol stabilized gold nanoparticles using ethanol or acetone in combination with gas-expanded hexane, compared to hexane alone.[39]

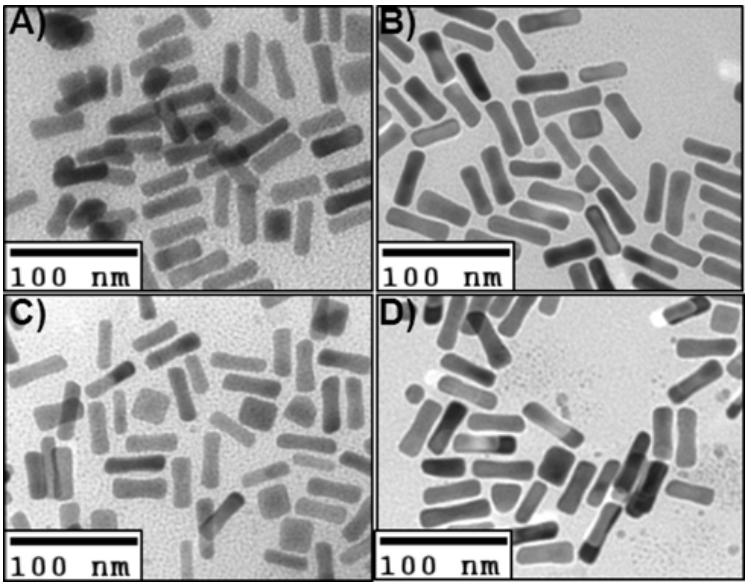

Figure 4.8: TEM images of octadecanethiol/ODS stabilized GNRs isolated at A) 0 psi, B) 100 psi and lower, C) between 100 and 150 psi, and D) between 250 and 300 psi using CO_2-expanded toluene.

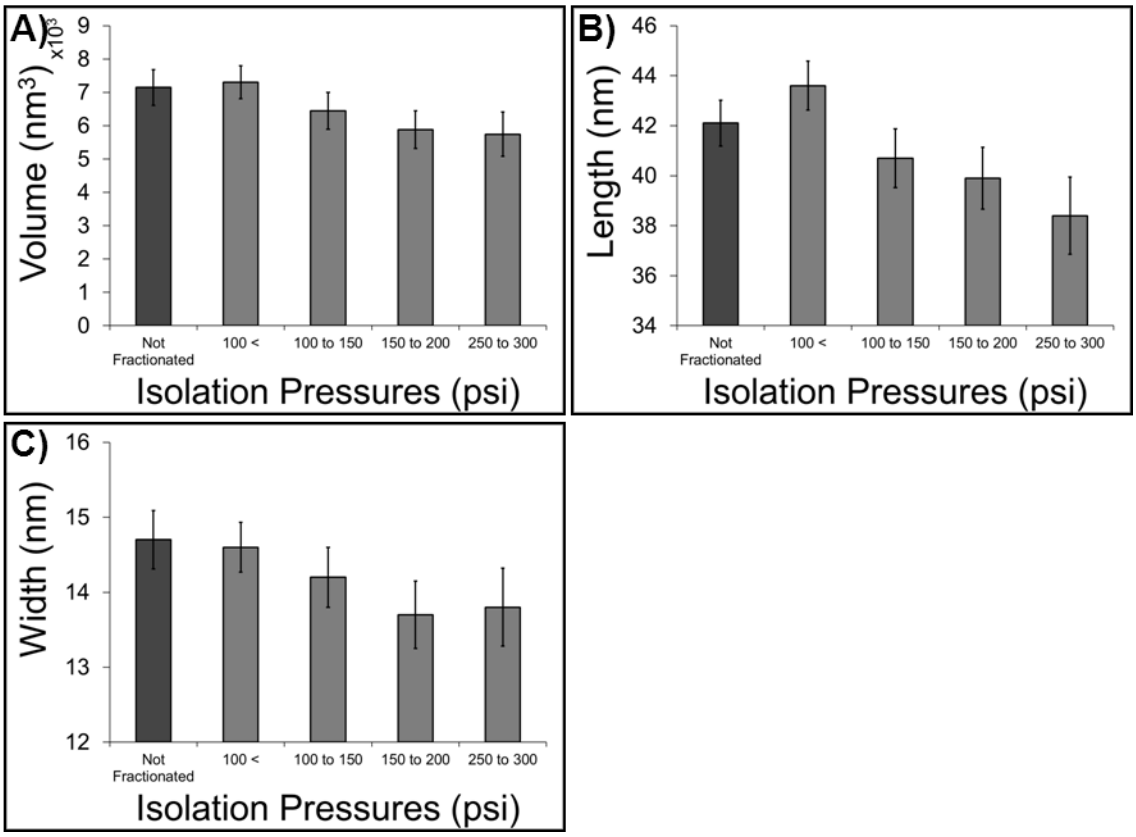

Figure 4.9: Calculated A) volumes, B) lengths, and C) widths of ODS/octadecanethiol modified GNRs dispersed isolated at varying pressure conditions using CO_2-expanded toluene.
* The error bars shown represent the 95% confidence interval and demonstrate significant differences between varying GNR fractions obtained during isolation.

Conclusions

This investigation showed an adapted protocol for the surface modification of GNRs enabling their suspension in several organic solvents including cyclohexane, toluene, and *n*-hexane. This work demonstrates the first ever fractionation of hydrophobically stabilized GNRs using CO_2-expanded toluene, which increased the GNR

monodispersity and decreased the excess seed concentration by 73% when precipitated at100 psi and lower. We also showed that varying both the alkane chain length and the dispersing solvent directly impacts GNR dispersibility. Chain lengths consisting of 12 carbons enabled GNR dispersibility up to 525 psi in CO2 expanded toluene, compared to 350 psi for chain lengths of 18 carbons. Varying the dispersing solvent (cyclohexane, toluene, or *n*-hexane) was shown to alter the precipitation pressures required for complete GNR precipitation. Cyclohexane proved to be the best solvent studied for GNR dispersibility, enabling dispersion up to 400 psi of CO_2 pressure, while toluene and *n*-hexane only dispersed GNRs up to 350 psi and 250 psi, respectively. Future work will include recursive fractionations to better evaluate the limitations of this technique. We also hope to explore the precipitation conditions which will enable the formation of wide-area networks of GNRs on substrates.

References

(1) Wang J.; Chen, C.; Yang, J.; Wu., J.; Wu, Y. *Chem. Phys. Lett.* **2005** *416* 215-19.

(2) Jana, N. R. *Small* **2005** *1* 875-82.

(3) Murphy, C. J.; Sau, T. K.; Gole, A. M.; Orendorff, C. J.; Gao, J.; Gou, L.; Hunyadi, S. E.; Li, T. *J. Phys. Chem. B* **2005** *109* 13857-70.

(4) Nusz, G. J.; Marinakos, S. M.; Curry, A. C.; Dahlin, A.; Hook, F.; Wax, A.; Chilkoti, A. *Anal. Chem.* **2008** *80* 984-989.

(5) Ding, H.; Yong, K.; Roy, I.; Pudavar, H. E.; Law, W. C.; Bergey, E. J.; Prasad, P. N. *J. Phys. Chem. C* **2007** *111* 12552-12557.

(6) Didychuk, C. L.; Ephrat, P.; Chamson-Reig, A.; Jacques, S. L.; Carson, J. J. L. *Nanotechnol.* **2009** *20* 195102 (9 pp.).

(7) Dickerson, E. B.; Dreaden, E. C.; Huang, X.; El-Sayed, I. H.; Chu, H.; Pushpanketh, S.; McDonald, J. F.; El-Sayed, M. A. *Cancer Lett.* **2008** *269* 57-66.

(8) Urena-Benavides, E. E.; Brown, P. J.; Kitchens, C. L. *Langmuir* **2010** *26* 14263-14270.

(9) Chen, J.; Wiley, B. J.; Xia, Y. *Langmuir* **2007** *23* 4120-4129.

(10) Sau, T. K.; Murphy, C. J. *Langmuir* **2004** *20* 6414-6420.

(11) Jana, N. R.; Gearheart, L.; Murphy, C. J. *J. Phys. Chem. B* **2001** *105* 4065-7.

(12) Murphy, C. J.; Thompson, L. B.; Alkilany, A. M.; Sisco, P. N.; Boulos, S. P.; Sivapalan, S. T.; Yang, J. A.; Chernak, D. J.; Huang, J. *J. Phys. Chem. C* **2010** *1* 2867-2875.

(13) Boca, S. C.; Astilean, S. *Nanotechnol.* **2010** *21* 235601 (8 pp.).

(14) Pastoriza-Santos, I.; Perez-Juste, J.; Liz-Marzan, L. M. *Chem. Mater.* **2006** *18* 2465-2467.

(15) Chandran, S. P.; Pasricha, R.; Bhatta, U. M.; Satyam, P. V.; Sastry, M. *J. Nanosci. Nanotechnol.* **2007** *7* 2808-2817.

(16) Mitamura, K.; Imae, T.; Saito, N.; Takai, O. *J. Phys. Chem. B* **2007** *111* 8891-8898.

(17) Jessop, P. G.; Subramaniam, B. *Chem. Rev.* **2007** *107* 2666-2694.

(18) Kitchens, C. L.; Roberts, C. B.; Juncheng, L.; Robert, A. W.; Madhu, A.; Von, W. G.; Hurst, K. M.; Saunders, S. R. In *Application of Gas-Expanded Liquids for Nanoparticle Processing: Experiment and Theory;* Gas-Expanded Liquids and Near-Critical Media; American Chemical Society: Washington, DC, 2009; pp 290-308.

(19) Anand, M.; McLeod, M. C.; Bell, P. W.; Roberts, C. B. *J. Phys. Chem. B* **2005** *109* 22852-22859.

(20) Liu, J.; Anand, M.; Roberts, C. B. *Langmuir* **2006** *22* 3964-3971.

(21) Saunders, S. R.; Roberts, C. B. *Nanotechnol.* **2009** *20* .

(22) McLeod, M. C.; Anand, M.; Kitchens, C. L.; Roberts, C. B. *Nano Lett.* **2005** *5* 461-5.

(23) Liu, J.; Sutton, J.; Roberts, C. B. *J. Phys. Chem. C* **2007** *111* 11566-11576.

(24) Brust, M.; Walker, M.; Bethell, D.; Schiffrin, D. J.; Whyman, R. *J. Chem. Soc. - Chem. Commun.* **1994** 801-802.

(25) Mitamura, K.; Imae, T.; Saito, N.; Takai, O. *J. Phys. Chem. B* **2007** *111* 8891-8.

(26) Patel, N. C.; Teja, A. S. *Chem. Eng. Sci.* **1982** *37* 463-473.

(27) Cuadros, F.; Faúndez, C. A.; Renuncio, J. A. R.; Mulero, A. *Thermochim. Acta* **2002** *389* 167-177.

(28) Ohgaki, K.; Katayama, T. *J. Chem. Eng. Data* **1976** *21* 53-55.

(29) Von White, G.; Kitchens, C. L. *J. Phys. Chem. C* **2010** *114* 16285-16291.

(30) Houndonougbo, Y.; Jin, H.; Rajagopalan, B.; Wong, K.; Kuczera, K.; Subramaniam, B.; Laird, B. *J. Phys. Chem. B* **2006** *110* 13195-202.

(31) Mukhopadhyay, M. *J. Supercrit. Fluids* **2003** *25* 213-223.

(32) Cabañas, A.; Renuncio, J. A. R.; Pando, C. *Ind Eng Chem Res* **2000** *39* 3566-3575.

(33) Abramoff, M. D.; Magalhaes, P. J.; Ram, S. J. *Biophoton Int.* **2004** *11* 36-41.

(34) McLeod, M. C.; Anand, M.; Kitchens, C. L.; Roberts, C. B. *Nano Lett.* **2005** *5* 461-465.

(35) White II, G. V.; Kitchens, C. L. In Preparation **2010**.

(36) Anand, M.; You, S.; Hurst, K. M.; Saunders, S. R.; Kitchens, C. L.; Ashurst, W. R.; Roberts, C. B. *Ind. Eng. Chem. Res.* **2008** *47* 553-559.

(37) McLeod, M. C.; Kitchens, C. L.; Roberts, C. B. *Langmuir* **2005** *21* 2414-2418.

(38) Kitchens, C. L.; McLeod, M. C.; Roberts, C. B. *J. Phys. Chem. B* **2003** *107* 11331-11338.

(39) Saunders, S. R.; Roberts, C. B. In *In Precipitation and fractionation of nanoparticles using gas-expanded mixtures as tunable solvents;* Boston, MA, 2010.

(40) Fernandez, C. A.; Hoppes, E. M.; Bekhazi, J. G.; Wang, C.; Wiacek, R. J.; Warner, M. G.; Fryxell, G. E.; Bays, J. T.; Addleman, R. S. *J. Phys. Chem. C* **2008** *112* 13947-13957.

(41) Alekseeva, A. V.; Bogatyrev, V. A.; Khlebtsov, B. N.; Mel'nikov, A. G.; Dykman, L. A.; Khlebtsov, N. G. *Colloid J.* **2006** *68* 661-678.

(42) Shah, P. S.; Holmes, J. D.; Johnston, K. P.; Korgel, B. A. *J. Phys. Chem. B* **2002** *106* 2545-51.

(43) Saunders, S. R.; Madhu, A.; You, S.; Roberts, C. B. In *In Total Interaction Energy Model to Predict Nanoparticle Dispersability in CO2-Expanded Solvents;* 2010; .

(44) Korgel, B. A.; Fullam, S.; Connolly, S.; Fitzmaurice, D. *J Phys Chem B* **1998** *102* 8379-88.

CHAPTER FIVE

GREEN SYNTHESIS OF ROBUST SILVER NANOPARTICLES USING GARLIC EXTRACT

Introduction

Metallic nanoparticles have been extensively investigated due to their unique size-dependent properties[1-4] which make them useful in a variety of applications including optical/chemical sensors,[5, 6] electronic devices,[7] and catalysts.[8] Widespread synthesis protocols used for nanoparticle production often require the use of harsh organic solvents/surfactants[9-11] and strong reducing agents (e.g. borohydride or hydrazine),[12-15] which typically generate large quantities of hazardous waste. Hence, synthesis procedures which eliminate the use of hazardous reagents[9, 16-18] and afford cost-effective alternatives for the isolation of stable nanoparticle dispersions are becoming more desirable as the number of nanoparticle applications increases.

In particular, biomedical research and application of metallic nanoparticles is growing due to their potential as therapeutic[19, 20] and contrasting agents.[21] Unfortunately, nanoparticle stability at *in vivo* conditions continues to be a drawback. It has been well demonstrated that biological media necessary for cellular growth and proliferation—solutions of glucose, amino acids, salts, vitamins, and water at an approximate pH of 7 (chemically similar to *in vivo* conditions)—cause irreversible nanoparticle agglomeration. For example, Greulich et al. found that silver nanoparticles stabilized by polyvinyl pyrrolidone (PVP) aggregate once exposed to biological media; however, nanoparticle conjugation with fetal calf serum improved stability.[22] In addition, Liu et al. showed that

increasing the concentration of capping agent (citrate) in solution and/or altering the pH of the aqueous dispersions of silver nanoparticles reduced aggregation and led to a decrease in Ag^+ release in biological media.[23] Exposure to reactive oxygen species (ROS, e.g. H_2O_2, $^{\cdot}OH$, and O_2^{-}) can also inhibit or render the intended nanoparticle application useless as a result of oxidization. Research has shown that living cells exposed to toxins and/or nanoparticles can result in ROS production[24-26] in response to stress and may lead to cell death.[23] Hence, methods to provide stable nanoparticle dispersions that do not aggregate in biological media and have high oxidation resistance are of significant importance. It is also desirable to employ natural and renewable reagents during synthesis because they 1) are more likely to be biocompatible and may eliminate the need for post-synthesis purification or surface modification as compared to other synthesis procedures,[18, 27] and 2) provide a cost-effective and facile nanoparticle production process with potential for industrial scale-up.

A common approach for green nanoparticle synthesis at ambient temperature is to begin with naturally available resources containing phytochemicals that function as both the reducing and stabilizing agents (following Green Chemistry Principles #'s 3- 8, and 12—Less Hazardous Chemical Syntheses, Designing Safer Chemicals, Safer Solvents and Auxiliaries, Design for Energy Efficiency, Use Renewable Feedstocks, Reduce Derivatives, Inherently Safer Chemistry for Accident Prevention, respectively).[28, 29] For example, ~15 nm diameter gold nanoparticles have been synthesized in aqueous media by Philip et al. using honey.[30] Similarly, Shukla et al. used soybean extracts to produce nontoxic gold nanoparticles and suggested that they are ideal for use in nanomedicine as

a result of their stability in various biological media and *in vitro* compatibility.[31] Other studies of silver and gold nanoparticle synthesis have employed herbal extracts from alfalfa,[32] lemongrass,[33] and geranium leaves,[34] where the natural extracts serve as both reducing and stabilizing agents.

Here we demonstrate a facile one-pot "green" synthesis of silver nanoparticles (4 to 6 nm) which utilizes *Allium sativum* (garlic) extract as the reducing and stabilizing agents. Garlic was studied in this investigation because of its well-known oxidative properties and its potent phytochemical contents. Our study of the wet-chemical synthesis conditions (garlic extract quantity and temperature) enabled control over nanoparticle size and size-distribution of the final dispersions. Furthermore, this investigation shows that garlic extract stabilized silver nanoparticles are resistant to aggregation in the presence of biological media and have high oxidative resistance in the presence of hydrogen peroxide (H_2O_2) compared to commonly prepared nanoparticles (citrate). As a result of the abundant and desirable medicinal characteristics of garlic,[35-38] these nanoparticles may be applicable in biomedical therapies, diagnosis, and sensing or aid in the development of novel technologies where nanoparticle health and safety is a primary concern.

Experimental

Materials

Silver nitrate ($AgNO_3$, 99.995%) was purchased from VWR. The stabilizing agent sodium citrate dihydrate (99%) and reducing agent sodium borohydride ($NaBH_4$,

98%) were purchased from VWR. Sodium hydroxide (H_2O_2, 30%) was obtained from Thermo Fisher. Sterile and filtered (0.1 μm) Hyclone DMEM/high modified media (4.0 mM L-glutamine, 4.500 mg/L glucose, without sodium pyruvate and phenol red) and minimum essential media (MEM, without phenol red) were obtained from Thermo Scientific. Softneck Garlic was purchased from a local grocery store (Ingles in Central, SC), peeled, and then rinsed with deionized water before use. All glassware was washed and rinsed with deionized water, followed by subsequent drying.

Characterization

Transmission Electron Microscopy (TEM) and Energy Dispersive X-ray (EDX)

All TEM images were obtained using a Hitachi 7600 with an accelerating voltage of 120 kV. TEM and EDX samples were prepared by drop casting ~5 µL of nanoparticle dispersion onto a formvar carbon coated copper TEM grid (Ted Pella), followed by air drying at ambient conditions. The size distributions were determined by image analysis using the ImageJ software package.[39] At least 300 nanoparticles were counted for meaningful and relevant statistics. All EDX analysis was performed on a Hitachi 4800 (scanning electron microscope, SEM) in TEM mode with an accelerating voltage of 30 kV.

Ultraviolet-visible (UV-VIS) *light spectroscopy*

UV-VIS analysis was performed on a Varian Cary 50 spectrophotometer. Deionized water was used for background correction of all UV-VIS spectra. All samples were loaded into a 1 cm path length quartz cuvette for UV-VIS analysis. UV-VIS spectra

were fit with Gaussian curves correcting for a cubic background in Igor Pro 6.1 (Wavemetrics, Portland, Oregon) for full-width at half maximum (FWHM) measurements. The Gaussian fits to the UV-VIS spectra all had goodness of fit values ($\chi^2 \sim 1$), indicating accurate curve analysis.

Attenuated total reflectance Fourier transform infrared (ATR-FTIR) spectroscopy

ATR-FTIR spectroscopy was performed on a Thermo-Fisher instrument using a Thermo-Nicolet Magna 550 FTIR spectrometer equipped with a Thermo-SpectraTech Foundation Series Diamond ATR accessory. Here, 16 sample scans were taken (at room temperature) and the resolution for both, the sample and background, was 4 cm^{-1}. All purified nanoparticle dispersions and garlic extracts were dried in a vacuum oven set to 40˚C to form powders. The dried samples were then placed on the spectrophotometer for analysis.

Zeta-Potential

Zeta-potential measurements were performed on a Malvern Zetasizer Nano-ZS (ZEN3600) at 25 ºC with an incident wavelength of 633 nm and a 173º backscattering angle. Clear disposable zeta potential cells (1 cm path length) were rinsed with ethanol, followed by deionized water prior to sample loading. The viscosity, refractive index, and absorption values were provided in the Malvern software for water (μ = 0.8872 cP, RI = 1.333) and crystalline silver (RI = 0.135, absorption = 3.987). Twelve runs were averaged for each liquid sample for accurate determination of zeta potential measurements.

Garlic Extract Preparation

Approximately 6 g of garlic was chopped (not crushed) into ~1/4" pieces and added to 50 mL of deionized water. Next, the garlic-water mixture was allowed to sit at room temperature for 24 hours. The resulting solution was decanted to collect the pale white transparent garlic extract solution, and the solid garlic pieces were removed. The garlic extract concentration was determined to be 22.9 ± 0.5 mg/mL by measuring the remaining solid weight after evaporating 2.0 mL of liquid extract in a vacuum oven at 40 °C, averaging over three measurements. Crushing the garlic prior to soaking and/or soaking at elevated temperatures was found to increase the extraction efficiency resulting in larger mass concentrations of extract. The variation in garlic extract preparation directly impacts the nanoparticle synthesis; i.e. larger quantities of garlic extract employed during synthesis were found to generate polydisperse populations of nanoparticles.

Silver Nanoparticle Synthesis

For silver nanoparticles capped by garlic, varying quantities of garlic extract solution (1 mL to 2.5 mL) were added to a 51 mL solution of 0.98mM of $AgNO_3$ in DI water. Within 2 hours, a light orange color change was noticeable, indicating the presence of silver nanoparticles. The solution was allowed to age for 48 hours yielding a deep orange/brown color. The silver nanoparticle dispersions were centrifuged for 15 min at 8,000 rpm to remove any large aggregates from solution and excess free garlic extract. The yellow/orange supernatant was collected and kept as the final silver

nanoparticle product. The precipitate containing excess garlic extracts (the higher molecular weight components, likely fructan) and nanoparticle aggregates were discarded appropriately. A water bath maintained at 60°C was used in experiments investigating the effect of temperature on nanoparticle synthesis. Accelerated synthesis was achievable by using a strong reducing agent, for example $NaBH_4$.

A procedure adapted from Jana et al. was used for the synthesis of citrate stabilized silver nanoaprticles.[40] In short, 100 µL of 0.05 M $AgNO_3$ was combined with 100 µL of 0.05 M of sodium citrate dihydrate, followed by dilution of the mixture to 20 mL with deionized water. Subsequently, the solution was reduced with 200 µL of ice cold 0.05 M $NaBH_4$ producing a yellow/orange solution indicating the presence of silver nanoparticles (4.0 ± 1.0 nm) in solution.

Stability of Silver Nanoparticles

Stability of the citrate and garlic extract capped nanoparticles was investigated by adding 1 mL of DMEM high modified biological media to 1 mL of dispersion. Additional experiments with DMEM and MEM biological media were performed by adding 4 mL of media to 1 mL of nanoparticle dispersion. UV-VIS measurements were performed over time for both the citrate and garlic extract stabilized nanoparticles. Nanoparticle resistance to oxidation was measured by UV-VIS before and after the addition (~ 5 minutes) of 100 μL of 30% H_2O_2 to 5 mL silver nanoparticle dispersion.

Results and Discussion

Nanoparticle Synthesis and Characterization

Nanoparticle size and size-distribution was investigated as a function of the garlic extract concentration used during nanoparticle synthesis. Figure 5.1 shows an image of the silver nanoparticle dispersions with increasing garlic extract amounts. Representative TEM images and histograms are shown in Figure 5.2 for silver nanoparticles prepared using 1.0 mL and 2.0 mL of garlic extract, respectively. Figure 5.3A shows the corresponding UV-VIS spectra for the nanoparticle dispersions shown in Figure 5.1. An increase in both color intensity (Figure 5.1) and UV-VIS absorbance (Figure 5.3A) are attributed to the increase in nanoparticle size. Additional UV-VIS analysis performed one week after synthesis showed no variation in absorbance. The UV-VIS results suggest that all nucleation or growth occurs within the first 48 hour period. Samples which have been stored for more than 9 months remain stable in solution with no visible sign of precipitation or aggregation.

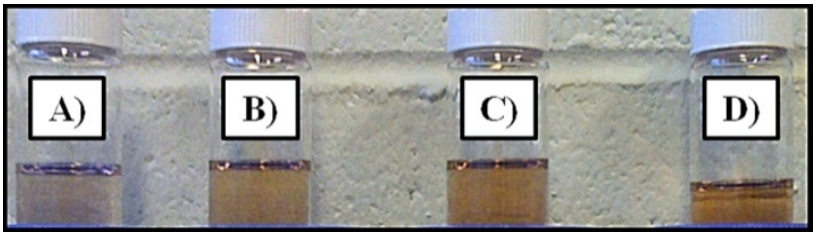

Figure 5.1: Representative images of silver nanoparticle dispersions synthesized with varying amounts of garlic extract solution at 25 °C after a 48 hour reaction time and purification by centrifugation A) 1.0 mL B) 1.5 mL C) 2.0 mL D) 2.5 mL.

The peak absorbance values were determined to be 404 nm by fitting a Gaussian curve to the UV-VIS spectra. Noticeable peak broadening and increases in absorbance amplitude are evident for the UV-VIS spectra shown in Figure 5.3A. The peak broadening is attributed to an increase in polydispersity as a result of increased garlic extract solution employed during synthesis. As the garlic extract quantity increased during nanoparticle synthesis from 1.0 mL to 2.0 mL, the FWHM values increased from 118 to 134 nm. TEM analysis of the garlic stabilized silver nanoparticles confirms variation in nanoparticle polydispersity, increasing from 25% to 36% with increasing garlic extract quantity (1.0 mL to 2.0 mL, see Table 1) and in size from 3.7 to 4.1 nm in core-diameter. Sileikaite et al. also observed increases in FWHM of UV-VIS spectra that correspond to increases in polydispersity for citrate stabilized silver nanoparticles.[41]

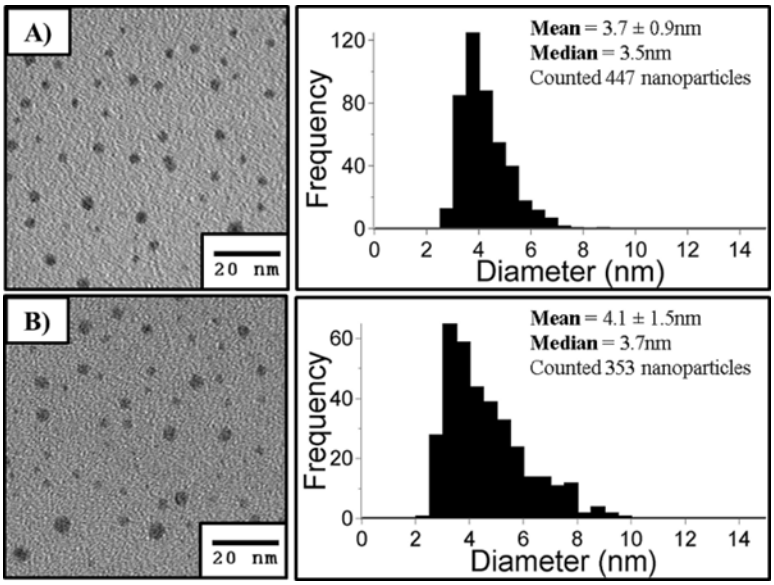

Figure 5.2: Representative TEM images and histograms for silver nanoparticles synthesized using garlic extract A) 1.0 mL of garlic extract and B) 2.0 mL of garlic extract.

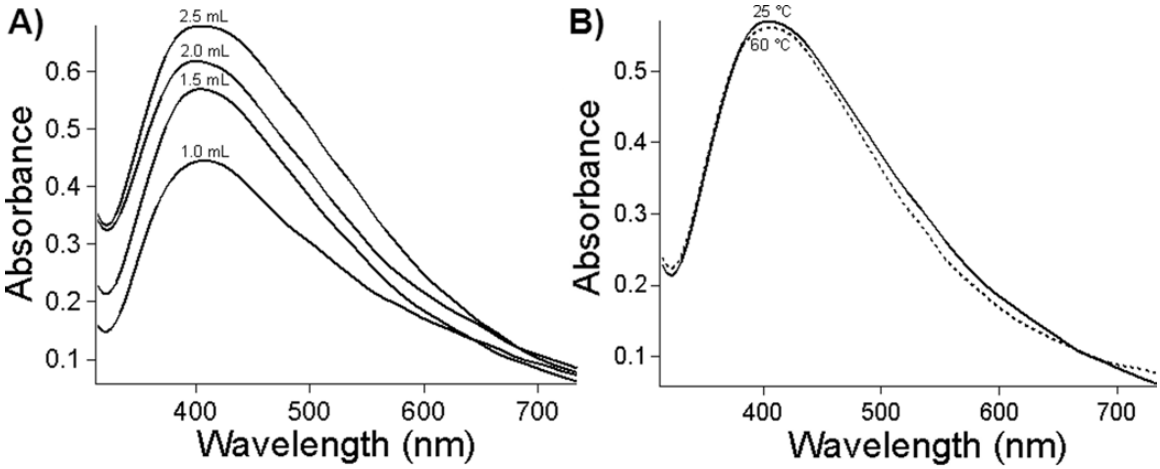

Figure 5.3: UV-VIS spectroscopy data for silver nanoparticles prepared using A) varying amounts garlic extract (1.0, 1.5, 2.0, and 2.5 mL) and B) 1.5 mL garlic extract at varying temperature (25 and 60 °C).

Comparatively, 2.5 mL of garlic extract used during nanoparticle synthesis produced the largest intensity in UV-VIS absorbance and also demonstrated a decrease in FWHM to 127 nm. According to Mie scattering theory, a decrease in FWHM is suggestive of an increase in silver nanoparticle core-diameter.[42] TEM results confirm an increase in nanoparticle diameter from 4 to 6 nm with increasing garlic extract amount from 2.0 to 2.5 mL. Jana et al. observed similar results for oleic acid stabilized Fe_3O_4, where larger quantities of oleic acid were shown to produce larger diameter nanocrystals.[43] Overall, lower concentrations of garlic extract yield smaller and more monodisperse populations of silver nanoparticles, and support previous work which demonstrates that tailoring the reducing and/or stabilizing ligand concentrations affords control over nanoparticle size and size-distribution.[15, 44-46] Table 1 is a summary of the mean core-diameter, size-distributions, and polydispersity of the silver nanoparticles

synthesized using garlic extract, complementing the UV-VIS spectra shown in Figure 5.3A and the FWHM results.

Table 5.1: The measured mean core-diameter, size-distributions, and polydispersity of silver nanoparticles prepared using varying garlic extract amounts. All core-diameter measurements were performed by TEM and ImageJ analysis.[39]

garlic extract used, (mL)	T, (°C)	diameter, (nm)	polydispersity, %
1.0	25	3.7 ± 0.9	25
1.5	25	3.8 ± 1.3	33
2.0	25	4.1 ± 1.5	36
2.5	25	6.2 ± 2.7	43
1.5	60	4.4 ± 1.5	35

In addition to controlling nanoparticle size and size-distribution with garlic extract quantity, reaction temperature was shown to impact nanoparticle size, polydispersity, and reaction kinetics. An elevated synthesis temperature of 60 ºC with 1.5 mL of garlic extract produced nanoparticles in 15 min, compared to 2 hours at 25 ºC. UV-VIS analysis showed a plasmon resonance peak at 404 nm for both the ambient and elevated temperatures. The FWHM value obtained from a Gaussian fit of the UV-VIS spectra was determined to be 133 nm; 10% broader than the 25 ºC synthesis, indicating increased polydispersity and particle diameter. TEM and UV-VIS analysis confirmed that the elevated temperature produced a more polydisperse population of silver nanoparticles. The increase in polydispersity is likely due to variation in the nucleation and growth rates of the nanoparticles during synthesis. Although the polydispersity is slightly greater for the elevated synthesis temperature, nanoparticle formation occurs at a faster rate and yields similar concentrations of nanoparticles (see UV-VIS absorbance peak amplitude in Figure 5.3B). This work supports other investigations, like Kasture et al., who

demonstrated that increased temperatures enabled faster synthesis times for silver nanoparticles stabilized by sophorolipids in water.[47]

Measured ATR-FTIR spectra (Figure 5.4A) show large –OH and –CH stretches obtained for the dried garlic extract (3300 and 2930 cm^{-1}) and garlic extract prepared silver nanoparticles (3270 and 2930 cm^{-1}). The presence of –OH and –CH characteristic peaks suggest that sugars are present in the garlic extract solution and nanoparticle dispersion. Sucrose and fructose are the primary non-structural sugars that are readily extracted from garlic[48] and likely function as both the reducing agent and stabilizing chemistries. This theory is supported by recent work which shows that sucrose and fructose can function as reducing agents for the synthesis of aqueous dispersions of silver nanoparticles[49] and also function as stabilizing ligands for various metal nanoparticles (e.g. Au, Ag, Pd, Pt).[13-15, 40] EDX chemical analysis (Figure 5.4B) performed on a dried film of garlic extract prepared nanoparticles shows that sulfur is also present in the garlic extract. The presence of sulfur is expected as result of the organosulfur compounds (primarily allyl sulfides) readily extracted from garlic using either water or ethanol.[50] Adding garlic extract solution to citrate stabilized silver nanoparticles demonstrated an increase in FWHM (57%), decrease in absorbance, and a shift in wavelength absorbance of 16 nm (see Figure 5.5). Cai et al. attributed large shifts in UV-VIS absorbance and increases in FWHM to a change in surface chemistry for unmodified silver nanoparticles when hexanethiol was added to the dispersion.[51] The organosulfur compounds present in the garlic extract may modify the surface chemistry of the silver nanoparticles through thiolate bonding. The variation in UV-VIS spectra may also be caused by a second

nucleation and growth stage caused by the fructose and sucrose present in the garlic extract. TEM images obtained after garlic extract was added to the citrate stabilized nanoparticles show an increase in both size and polydispersity. The mean core diameter was measured to be 6.6 ± 2.9 nm (44% polydispersity). Albeit further chemical analysis may be beneficial in determining the exact stabilizing chemistries of the silver nanoparticles, the organosulfur compounds may also function as stabilizing agents[52,50] in addition to the sugars.

Zeta potential measurements were performed for a direct comparison to conventional studies of nanoparticle stability. Zeta potential analysis demonstrated that the garlic extract and citrate stabilized nanoparticles had negative potentials of -31 mV and -30 mV, respectively. Both silver nanoparticle dispersions indicate that they are sufficiently charged to maintain stability in solution over long periods of time (both chemistries have maintained stable dispersions at room temperature over a month). Similarly, Kittler et al. measured the zeta potential for citrate stabilized silver nanoparticles to be -30 mV.[53]

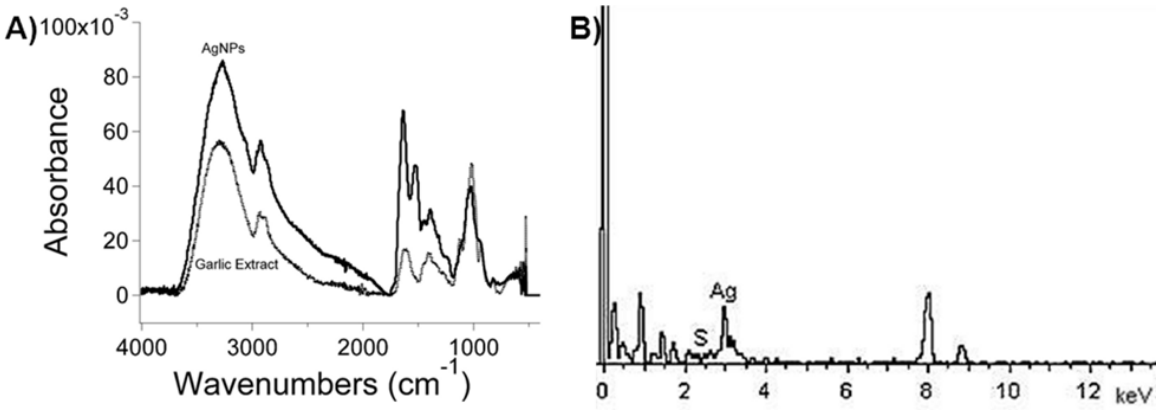

Figure 5.4: A) Representative diamond ATR-FTIR data from dried garlic extract and dried silver nanoparticles synthesized using garlic extract. B) EDX spectra of garlic extract prepared silver nanoparticles obtained from FE SEM.

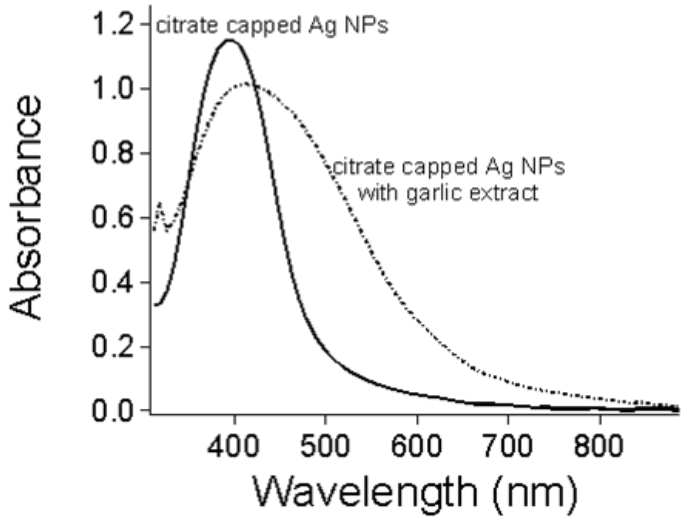

Figure 5.5: UV-VIS spectra for Ag NPs stabilized by citrate prior to and after the addition of garlic extract

Nanoparticle Stability: Resistance to Aggregation and Oxidation

Applications of silver nanoparticles in the biomedical field and commercial industry are growing rapidly due to the unique antibacterial properties.[54-57] Therefore, understanding nanoparticle stability at biological conditions and in biological media is becoming increasingly critical. We have studied the stability of garlic extract stabilized silver nanoparticles in biological cell culture media (DMEM/high modified and MEM). We have also examined nanoparticle oxidation resistance against H_2O_2 in order to predict nanoparticle behavior in the presence of large quantities of ROS. Understanding nanoparticle aggregation and oxidation at biological conditions will provide insight to *in vivo* nanoparticle behavior.

Silver nanoparticles stabilized with the garlic extract are compared to commonly synthesized citrate stabilized silver nanoparticles (4.0 ± 1.0 nm). Figure 5.6 shows UV-

VIS spectra for the 1.5 mL garlic extract and citrate prepared silver nanoparticles as a function of time after 50% by volume addition of DMEM biological media to the nanoparticle dispersion. In Figure 5.6A, the UV-VIS absorbance for the garlic stabilized silver nanoparticles exhibits a decrease over 18 hours. The decrease in plasmon resonance may be a result of reversible clustering, as gentle mixing of the liquid readily re-suspends the nanoparticles back into solution. After 18 hours of incubation in DMEM media, the characteristic plasmon resonance peak at 404 nm is still present. Visual inspection of the garlic stabilized silver nanoparticles showed no signs of visible aggregation. Increasing the ratio of DMEM to nanoparticle dispersion (4:1 by volume) provided similar results to the 1:1 ratio. The addition of MEM biological media to the garlic stabilized silver nanoparticles at a ratio of 4:1 by volume also showed a decrease in UV-VIS absorbance; however, no red shift in UV-VIS absorbance or aggregation was observed.

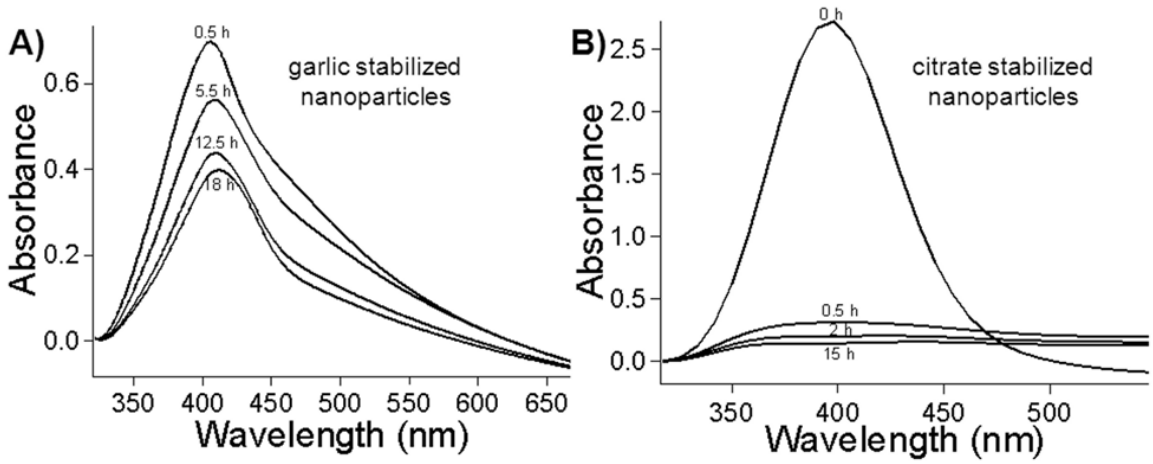

Figure 5.6: UV-VIS spectra for Ag NPs stabilized by A) garlic extract and B) citrate in the presence of DMEM/High Mod cell culture media with varying time

Comparatively, Figure 5.6B shows a significant decrease in surface plasmon resonance (SPR) absorbance at 404 nm in less than 30 minutes with the addition of DMEM biological media to the citrate stabilized nanoparticles (1:1 ratio by volume). At 15 hours of incubation in DMEM biological media, the nanoparticles have completely and irreversibly precipitated out of solution. The significantly enhanced stability of garlic extract stabilized silver nanoparticles in biological media makes them a potential candidate for *in vivo* application and studies to differentiate the toxicity effects of Ag^+ and nanosilver.[23,53]

In addition to investigating nanoparticle compatibility with biological media, the garlic extract stabilized silver nanoparticles were tested for oxidation resistance to H_2O_2 exposure. Figure 5.7 shows the UV-VIS spectra of citrate and garlic extract stabilized silver nanoparticles exposed to H_2O_2. Fitting the UV-VIS spectra in Figure 5.7A demonstrates a red shift (4 nm) in SPR absorbance and an increase in FWHM (24 nm) suggesting an in increase in polydispersity and/or size. Upon H_2O_2 addition, the citrate stabilized nanoparticle dispersion immediately turns clear. The loss of SPR absorbance (Figure 5.7B) demonstrates poor oxidation resistance and indicates Ag^0 oxidation to Ag^+ for the citrate stabilized silver nanoparticles. The SPR absorbance peak for the garlic extract stabilized silver nanoparticles is still present after H_2O_2 addition, though at a lower absorbance value.

The oxidation resistance to H_2O_2 may be attributed to the phytochemical compounds present in the aqueous garlic extract, more explicitly allicin (diallyl-thiosulfinate) and other allyl sulfides.[50] To confirm this hypothesis, garlic extract was

added to the citrate stabilized silver nanoparticles and the oxidation resistance was measured by UV-VIS. We observed a significant increase in oxidation resistance for citrate stabilized silver nanoparticles when adding garlic extract to the dispersion (see Figure 5.7C). Allicin is the primary organosulfur compound found in garlic[37] and is credited with having strong anti-oxidant properties including scavenging hydroxyl radicals[58] and suppressing oxygen radical formation.[59] We propose that the freely available allyl sulfides dispersed in solution, or bound to the surface of the silver nanoparticles, increases nanoparticle oxidation resistance.

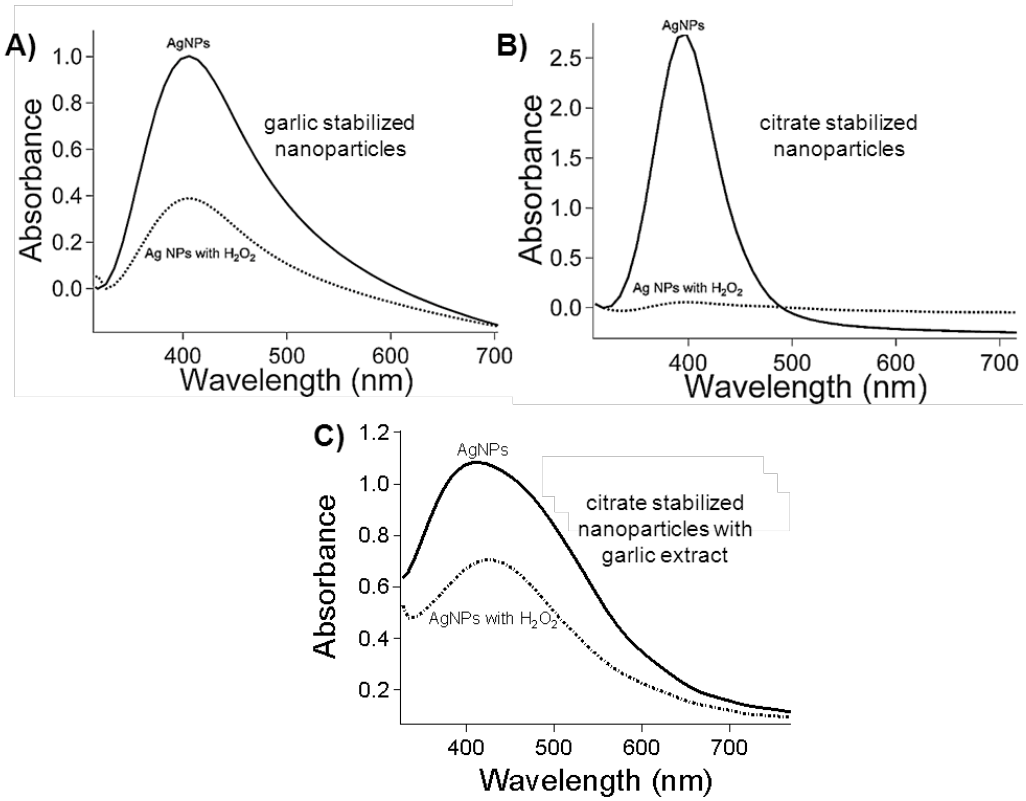

Figure 5.7: UV-VIS spectra for Ag NPs stabilized by A) garlic extract, B) citrate, and C) citrate with garlic extract in the presence of 30% H_2O_2

Conclusions

We have demonstrated a one pot "green" synthesis of silver nanoparticles using garlic extract as both the reducing and stabilizing agents. This procedure offers a cost-effective and "green" alternative to traditional protocols and may be readily scaled-up for industry as a result of the low synthesis temperatures and times required. We show that controlling the quantity of the garlic extract employed during synthesis enables facile variation of nanoparticle size and size-distribution (approximately 4 and 6 nm in core-diameter). An increased synthesis temperature of 60 °C facilitated an increased synthesis time, but also increased the polydispersity and size of the nanoparticle dispersion. ATR-FTIR and EDX chemical analysis suggest that the reducing and stabilizing agents are likely sugars (fructose and/or sucrose), where co-stabilization may also occur by the organosulfur compounds present in the garlic extract. The silver nanoparticles prepared using garlic extract demonstrated compatibility with frequently used biological media. Oxidation resistance was also observed when H_2O_2 was added to nanoparticle dispersions. The strong oxidation resistance of the garlic extract prepared silver nanoparticles is attributed to the presence of organosulfur compounds in the form of allyl sulfides.

References

(1) Grassian, V. H. *J. Phys. Chem. C* 2008 *112* 18303-18313.

(2) Jain, P. K.; Lee, K. S.; El-Sayed, I.; El-Sayed, M. *J. Phys. Chem. B* 2006 *110* 7238-48.

(3) Liu, C.; Zhang, Z. J. *Chem. Mater.* 2001 *13* 2092-6.

(4) Xu, X. -. N.; Huang, S.; Brownlow, W.; Salaita, K.; Jeffers, R. B. *J. Phys. Chem. B* 2004 *108* 15543-51.

(5) Manno, D.; Filippo, E.; Di Giulio, M.; Serra, A. *J. Non Cryst. Solids* 2008 *354* 5515-20.

(6) Kim, Y. J.; Yang Y. S.; Ha S.; Cho, S. M.; Kim Y. S.; Kim H. Y.; Yang, H.; Kim Y. T. *Sensor. Actuat. B-Chem.* 2005 *106* 189-98.

(7) Prakash, A.; Ouyang, J.; Lin, J.; Yang, Y. *J. Appl. Phys.* 2006 *100* .

(8) LaLonde, A. D.; Grant Norton, M.; Zhang, D.; Ganadean, D.; Alkhateeb, A.; Padmanabhan, R.; McIlroy, D. N. *J. Mater. Res.* 2005 *20* 3021-7.

(9) Brust, M.; Walker, M.; Bethell, D.; Schiffrin, D. J.; Whyman, R. *J. Chem. Soc. - Chem. Commun.* 1994 801-802.

(10) Herrera, A. P.; Resto, O.; Briano, J. G.; Rinaldi, C. *Nanotechnol.* 2005 *16* 618-25.

(11) Kitchens, C. L.; McLeod, M. C.; Roberts, C. B. *Langmuir* 2005 *21* 5166-5173.

(12) Wu, M.; Lai, L. *Colloids Surf. Physicochem. Eng. Aspects* 2004 *244* 149-157.

(13) Liu, J.; Sutton, J.; Roberts, C. B. *J. Phys. Chem. C* 2007 *111* 11566-11576.

(14) Liu, J.; Anand, M.; Roberts, C. B. *Langmuir* 2006 *22* 3964-3971.

(15) Liu, J.; He, F.; Gunn, T. M.; Zhao, D.; Roberts, C. B. *Langmuir* 2009 *25* 7116–7128.

(16) Sook, Y. M.; Kusunose, T.; Sekino, T. *Mater. Lett.* 2009 *63* 2038-40.

(17) Chen, X.; Sui, Z. M.; Wang, L. Y.; Xu, L. M.; Zhuang, W. C.; Chai, Y. C.; Yang, C. J. *Physica E* 2006 *33* 308-14.

(18) Boca, S. C.; Astilean, S. *Nanotechnol.* 2010 *21* 235601 (8 pp.).

(19) Urbina, M. C.; Zinoveva, S.; Miller, T.; Sabliov, C. M.; Monroe, W. T.; Kumar, C. S. S. R. *J. Phys. Chem. C* 2008 *112* 11102-11108.

(20) Bhattacharya, R.; Patra, C. R.; Earl, A.; Wang, S.; Katarya, A.; Lu, L.; Kizhakkedathu, J. N.; Yaszemski, M. J.; Greipp, P. R.; Mukhopadhyay, D.; Mukherjee, P. *Nanomed. Nanotechnol. Biol. Med* 2007 *3* 224-38.

(21) Rosensweig, R. E. *J. Magn. Magn. Mater.* 2002 *252* 370-374.

(22) Greulich, C.; Kittler, S.; Epple, M.; Muhr, G.; Köller, M. *Langenbecks Arch. Surg.* 2009, *394*, 495-502.

(23) Liu, J.; Hurt, R. H. *Environ. Sci. Technol.* 2010 *44* 2169-2175.

(24) Halter, M.; Almeida, J. L.; Tona, A.; Cole, K. D.; Plant, A. L.; Elliott, J. T. *Assay Drug Dev. Technol.* 2009 *7* .

(25) Carlson, C.; Hussain, S. M.; Schrand, A. M.; Braydich-Stolle, L.; Hess, K. L.; Jones, R. L.; Schlager, J. J. *J. Phys. Chem. B* 2008 *112* 13608-19.

(26) AshaRani, P. V.; Mun, G. L. K.; Hande, M. P.; Valiyaveettil, S. *ACS Nano* 2009 *3* 279-290.

(27) Leonov, A. P.; Zheng, J.; Clogston, J. D.; Stern, S. T.; Patri, A. K.; Wei, A. *ACS Nano* 2008 *2* 2481-2488.

(28) Anastas, P. T.; Warner, J. C. Twelve Principles of Green Chemistry. *http://www.epa.gov/gcc/pubs/principles.html* (accessed October 20, 2010).

(29) Anastas, P. T.; Warner, J. C. In *Green Chemistry: Theory and Practice;* Oxford University Press: New York, NY, 1998; pp 30.

(30) Philip, D. *Spectrochim. Acta, Part A* 2009 *73* 650-653.

(31) Shukla, R.; Nune, S. K.; Chanda, N.; Katti, K.; Mekapothula, S.; Kulkarni, R. R.; Welshons, W. V.; Kannan, R.; Katti, K. V. *Small* 2008 *4* 1425-36.

(32) Gardea-Torresdey, J.; Gomez, E.; Peralta-Videa, J.; Parsons, J. G.; Troiani, H.; Jose-Yacaman, M. *Langmuir* 2003 *19* 1357-1361.

(33) Shankar, S. S.; Rai, A.; Ahmad, A.; Sastry, M. *Chem. Mater.* 2005 *17* 566-72.

(34) Shankar, S. S.; Ahmad, A.; Sastry, M. *Biotechnol. Prog.* 2003 *19* 1627-1631.

(35) Naganawa, R.; Iwata, N.; Ishikawa, K.; Fukuda, H.; Fujino, T.; Suzuki, A. *Appl. Environ. Microbiol.* 1996 *62* 4238-4242.

(36) Tedeschi, P.; Maietti, A.; Boggian, M.; Vecchiati, G.; Brandolini, V. *J. Environ. Sci. Health. , Part B* 2007 *42* 795-799.

(37) Rahman, M. S. *Int. J. Food Prop.* 2007 *10* 245-268.

(38) Srinivasan, K. *Food Res. Int.* 2005 *38* 77-86.

(39) Abramoff, M. D.; Magalhaes, P. J.; Ram, S. J. *Biophoton Int.* 2004 *11* 36-41.

(40) Jana, N. R.; Gearheart, L.; Murphy, C. J. *J. Phys. Chem. B* 2001 *105* 4065-7.

(41) Sileikaite, A.; Puiso, J.; Prosycevas, I.; Tamulevicius, S. *Mater. Scien. - Medziagotyra* 2009 *15}* 21-27.

(42) Bhui, D. K.; Bar, H.; Sarkar, P.; Sahoo, G. P.; De, S. P.; Misra, A. *J. Mol. Liq.* 2009 *145* 33-37.

(43) Jana, N. R.; Chen, Y.; Peng, X. *Chem. Mater.* 2004 *16* 3931-5.

(44) Ji, X.; Song, X.; Li, J.; Bai, Y.; Yang, W.; Peng, X. *J. Am. Chem. Soc.* 2007 *129* 13939-13948.

(45) Sun, Y.; Xia, Y. *Science* 2002 *298* 2176-9.

(46) Pileni, M. P.; Jiang, X. C. *Colloids Surf. , A* 2007 *295* 228-32.

(47) Kasture, M. B.; Patel, P.; Prabhune, A. A.; Ramana, C. V.; Kulkarni, A. A.; Prasad, B. L. V. *J. Chem. Sci.* 2008 *120* 515-520.

(48) Losso, J. N.; Nakai, S. *J. Agric. Food Chem.* 1997 *45* 4342-4346.

(49) Mehta, S. K.; Chaudhary, S.; Gradzielski, M. *J. Colloid Interface Sci.* 2010 *343* 447-453.

(50) Block, E. *Sci. Am.* 1988 *252* 114.

(51) Cai, M.; Chen, J.; Zhou, J. *Appl. Surf. Sci.* 2004 *226* 422-426.

(52) Love, J. C.; Estroff, L. A.; Kriebel, J. K.; Nuzzo, R. G.; Whitesides, G. M. *Chem. Rev.* 2005 *105* 1103-1169.

(53) Kittler, S.; Greulich, C.; Diendorf, J.; Koeller, M.; Epple, M. *Chem. Mater.* 2010 *22* 4548-4554.

(54) Marambio-Jones, C.; Hoek, E. *J. Nanopart. Res.* 2010, *12*, 1531-1551.

(55) Sharma, V. K.; Yngard, R. A.; Lin, Y. *Adv. Colloid Interface Sci.* 2009 *145* 83-96.

(56) Kvitek, L.; Pancek, A.; Soukupova, J.; Kolar, M.; Vecerova, R.; Prucek, R.; Holecova, M.; Zboril, R. *J. Phys. Chem. C* 2008 *112* 5825-34.

(57) Shrivastava, S.; Bera, T.; Roy, A.; Singh, G.; Ramachandrarao, P.; Dash, D. *Nanotechnol.* 2007 *18* 9.

(58) Prasad, K.; Laxdal, V. A.; Yu, M.; Raney, B. L. *Mol. Cell. Biochem.* 1995 *148* 183-189.

(59) Astashkin, E. I.; Khokhlova, O. A.; Til'kunova, N. A.; Zalepugin, D. Y.; Glezer, M. G.; Grachev, S. V. *Dokl Biol Sci* 2003, *389*, 188-191.

CHAPTER SIX

INVESTIGATION OF GOLD NANOPARTICLE LOADING IN LIPID VESICLE BILAYERS USING SMALL-ANGLE NEUTRON SCATTERING

Introduction

Significant advances in metal nanoparticle synthesis have afforded facile control of size,[1-3] shape,[4, 5] and surface chemistry.[6, 7] The biomedical field has greatly benefited by these advances,[8-10] which has resulted in the use of nanoparticles as contrast agents,[8] hyperthermia agents,[10] and targeted drug delivery devices.[11, 12, 12] Tailoring the surface chemistry of the nanoparticles enhances their effectiveness in application by increasing bioavailability, decreasing macrophage uptake, and enabling site-specific targeting.[6, 13-15] Hence, research which investigates the surface modification of nanoparticles and increases their biocompatibility is critical for the development future nanotherapies.

Coating or encapsulating nanoparticles with lipids is a useful approach to increase biocompatibility, as the stabilizing surface chemistry is similar to the structural components of the cellular membrane.[14, 16-18] Research of hybrid lipid vesicle-nanoparticle systems is particularly attractive because it affords the potential use of hydrophobically stabilized nanoparticles in biomedical applications,[19] and maintains a hydrophilic vesicle core which can be used for drug loading.[20] Numerous studies demonstrate the successful loading of hydrophobically stabilized nanoparticles into the bilayer of lipid vesicles.[16, 17] Disruptions to lipid ordering (fluidity of the membrane)[16, 17] and variation in lipid phase behavior[17] has been observed with the addition of hydrophobic nanoparticles. This necessitates detailed characterization of these vesicle-

nanoparticle systems prior to *in vivo* use because this directly impacts vesicle size and phase behavior.

Park et al. encapsulated 3 – 4 nm stearylamine stabilized gold nanoparticles into the hydrophobic bilayer of lipid vesicles and showed that increasing nanoparticle loading within the bilayer caused increased membrane fluidity (or decrease lipid ordering).[16] Bothun showed that loading decanethiol silver nanoparticles into DPPC bilayers resulted in altered lipid phase behavior, as observed by decreases in both pre-transition and melting temperatures, corresponding to the ripple and fluid phases, as well as increased bilayer fluidity.[17] This work is complemented by the investigation of Chen et al., who used radio frequency to tunably release hydrophilic fluorescent molecules (representative of a drug) from DPPC vesicles with 5 nm oleic acid capped magnetic nanoparticles partitioned into the bilayer.[21] Chen et al. showed that radio frequency induced nanoparticle heating resulted in increases in membrane fluidity and the on demand release of fluorescent molecules from within the vesicle core. Rasch et al. demonstrated uniform encapsulation of sub 2 nm dodecanethiol stabilized gold nanoparticles into the hydrophobic acyl core of phosphatidylcholine bilayers and demonstrated no variation to the vesicle structure (determined by cryo-TEM), even at loadings of 1,500 lipids to nanoparticle, and suggests that nanoparticle size may impact nanoparticle ordering. [14] Investigations that study the effects of size, shape, and nanoparticle loading concentration on bilayer thickness, fluidity, and phase transitions are critical for the development of effective nanotherapies. For a general overview, Figure 6.1 shows a schematic of the significant areas of interest for hybrid vesicle-nanoparticle systems.

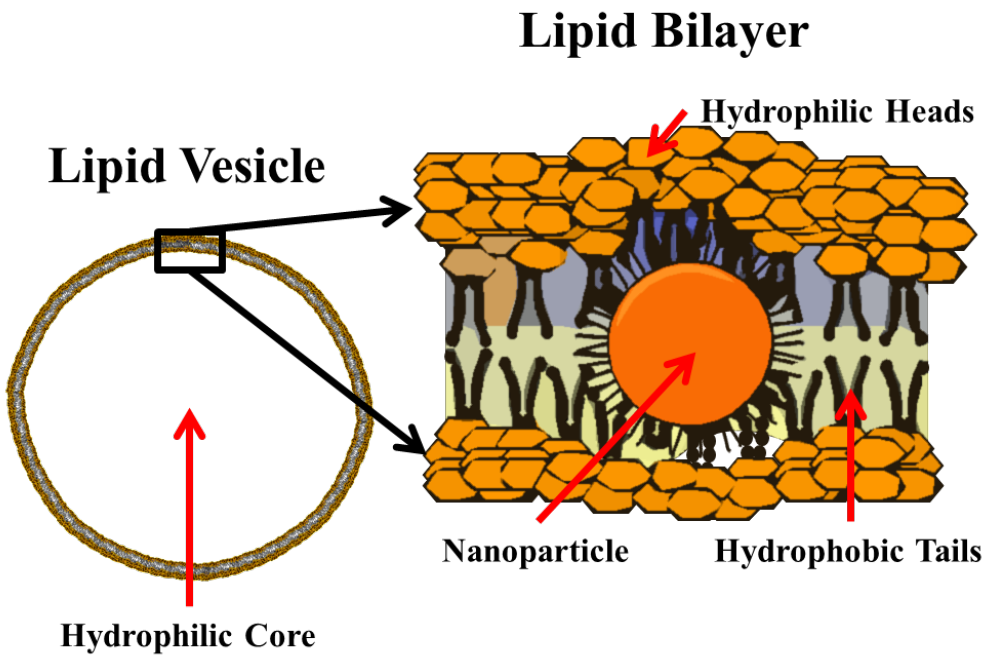

Figure 6.1: Schematic of a lipid vesicle and lipid bilayer with hydrophobic nanoparticle partitioned into the bilayer.

Small-angle neutron scattering (SANS) is a powerful technique which can provide structural and compositional information of a variety of samples (both liquid and solid), due to neutron scattering length density (SLD, a function of atomic composition, density, and incident neutron wavelength) dependence.[22] Selective deuteration of lipid vesicle dispersions enables simultaneous measurement of lipid vesicle size and bilayer thickness (deuterium oxide as the solvent is typically used in conjunction with hydrogenated lipids).[23, 24] Kiselev et al. used SANS to investigate the vesicle bilayer thickness as a function of temperature, demonstrating that increasing temperatures from 10 °C to 60°C (corresponding to the gel and fluid phases, respectively for DPPC) results in a decrease in thickness from nearly 44 Å to 37Å for dimyristoylphosphatidylcholine (DMPC, contains

two 14 carbon chains) vesicles.[23] Boggara et al. recently employed SANS to determine bilayer thickness variation with varying quantities of a common nonsteroidal anti-inflammatory drug, and observed low pH values induced decreases in the bilayer thickness of DMPC vesicles (decrease from 40 Å to 39 at 30 °C measured at pH values of 2 and 8, respectively).[25] These investigations demonstrate the feasibility of SANS for bilayer thickness measurements of hybrid vesicle-nanoparticle systems.

We have employed SANS to determine the effects of A) nanoparticle concentration (10,000:1, and 5,000:1 lipids to nanoparticles, corresponding to ~17 and 35 nanoparticles per 1000 Å diameter vesicle), B) nanoparticle size (3.9 and 4.2 nm), and C) temperature (25 °C, 37°C, and 50°C corresponding to the gel, ripple, and fluid phases, respectively) on dimyristoylphosphatidylcholine (DPPC, contains two 16 carbon chains)/ dipalmitoylphosphatidylglycerol (DPPG, charged lipid containing two 16 carbon chains), and DPPC/DPPG vesicles containing cholesterol as a stabilizing agent. We show that the DPPC/DPPG bilayer thickness increases with gold nanoparticle (GNP, ~3.9 and 4.2 nm) loading ratios of 10,000: 1 and 5,000: 1 compared to the control vesicle sample. Temperature increases from 25 °C to 50 °C, demonstrated decreases in bilayer thickness in DPPC/DPPG vesicle-GNP systems as expected, due to the self-assembly temperature dependence of the lipids. The results from this work have helped create a better fundamental understanding of the impact nanoparticle loading has on the vesicle bilayer thickness and vesicle clustering in solution which will be useful in the development of vesicle-nanoparticle therapeutic systems.

A special note regarding the units used in this chapter: we intend to be consistent with the current literature, and therefore units of Å will used to describe bilayer thickness values and vesicle diameters. Comparatively, nm will be used to describe the size (core-diameter) of the nanoparticles.

Experimental Methods

Materials

The metal precursor hydrogen tetrachloroaurate (III) trihydrate ($HAuCl_4 \cdot 3H_2O$, 99.99%) was purchased from VWR. The stabilizing agents sodium citrate dihydrate (99%), stearylamine (> 80%) and reducing agent sodium borohydride ($NaBH_4$, 98%) were purchased from VWR. ACS grade ethanol (95%) and toluene (99.7%) were purchased by VWR. Deuterium oxide (D_2O, 99.9%) was purchased from Cambridge Isotope Laboratories. The phospholipids 1,2-dipalmitoyl-sn-glycero-3-phosphocholine (DPPC) and 1,2-dipalmitoyl-sn-glycero-3-phospho-(1'-rac-glycerol) (DPPG), and cholesterol were provided by Dr. Bothun from University of Rhode Island. All chemicals were used without further purification.

Nanoparticle Synthesis

Citrate stabilized gold nanoparticles (GNPs) were prepared by a modified procedure similar to Jana et al.[26] yielding ~4 nm diameter particles. In short, 30 mL of citrate solution (0.05 M) was added to 567 mL of DI water in a 1 L volumetric flask. Next, 3 mL of 0.05M $HAuCl_4$ was added to the mixture and reduced with 3 mL $NaBH_4$ (0.05 M). The resulting aqueous dispersed GNPs were ruby red in color.

Next, the GNPs were resuspended in toluene by surface modification using stearylamine, similar to procedures previously described.[27] Briefly, between 100 to 300 mL of 0.01 M steartylamine solutions in toluene were added to the 600 mL aqueous GNP dispersion in a volumetric flask. The biphasic mixture was vigorously shaken until the GNPs transferred from the aqueous phase to the toluene phase. The biphasic mixture was placed in a 1 L separatory funnel, where the toluene dispersed GNPs were isolated from the aqueous phase. Next, ethanol was added to the GNPs (4:1 ethanol to GNP dispersion by volume) followed by centrifugation at 14,500 rpms for 10 min to induce nanoparticle precipitation. The supernatant liquid, containing excess stabilizing ligands and organic solvent was decanted. The GNPs were resuspended in 20 mL neat solvent (hexane or toluene) followed by 5 min of sonication. The purification procedure was performed a total of three times before use. It is important to mention that Bothun and coworkers observed changes in lipid phase behavior for purchased nanoparticles dispersions and vesicles synthesized with excess ligands (results not published). Hence, the removal of excess surfactants or ligands is extremely critical for accurate characterization of lipid phase behavior, particularly when nanoparticles are employed.

Recursive fraction using the anti-solvent/solvent pair ethanol/toluene combined with centrifugation was performed as described by Korgel et al.[28] and White et al.[29] to isolate GNPs, measured to be 3.9 nm and 4.2 nm in core-diameter. The synthesis, surface modification, and fractionation of GNPs were repeated until enough samples were prepared (nearly ~30 mL at 5 mg/mL for each size). Figure 6.2 shows TEM images and

size distributions for the two size-fractions of stearylamine stabilized GNPs employed during lipid vesicle preparation.

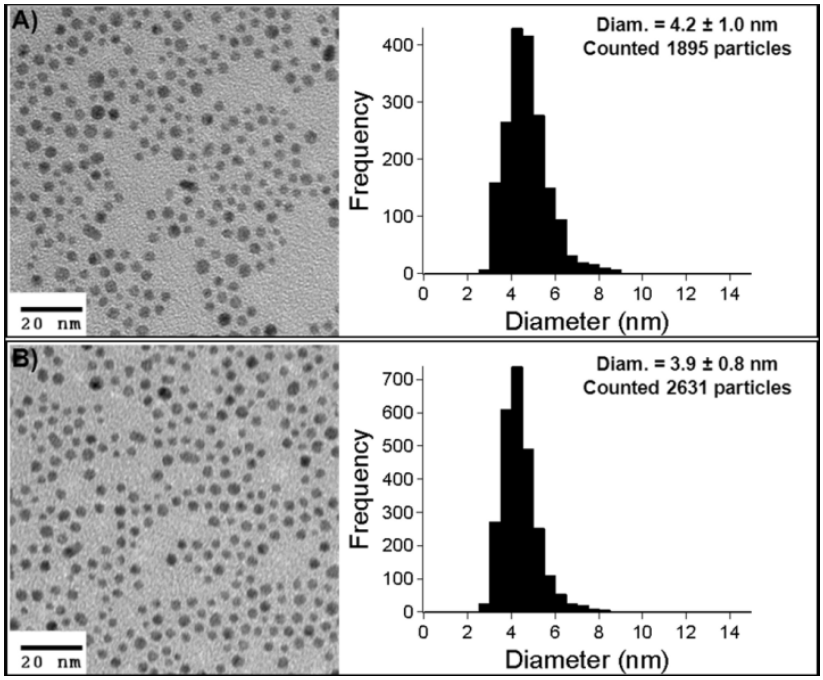

Figure 6.2: TEM images and respective histograms for stearylamine stabilized gold nanoparticles measured to be A) 4.2 nm and B) 3.9 nm in core-diameter.

Lipid Vesicle Preparation

The stearylamine modified gold nanoparticles were shipped to Dr. Geoffrey Bothun and Yanjing Chen at the University of Rhode Island. Yanjing Chen prepared all lipid vesicles employed during SANS experiments. A control lipid vesicle solution was prepared consisting of DPPC/DPPG (85%/15% ratio of DPPC/DPPG) dispersed in D_2O. DPPC/DPPG lipid vesicles were also prepared, with the stearylamine stabilized GNPs partitioned into the bilayer (3.9 nm and 4.2 nm). The loading ratios used were 10,000:1

and 5,000:1 (lipids to nanoparticles). An additional lipid vesicle sample was prepared using DPPC/DPPG (80%) with cholesterol (20%) loaded with 5,000: 1GNPs (4.2 nm). Both DPPC and DPPG lipids were employed for vesicle formation because phosphatidylcholine (PC) and phosphotidylglycerol (PG) lipids make up the majority of surfactants in human cellular membranes, for example pulmonary cells membranes are composed of ~80% PC and 10% PG lipids, by mass.

Characterization

Transmission Electron Microscopy (TEM)

All TEM images of GNPs were obtained using a Hitachi 7600 with a 120 kV accelerating voltage. TEM samples were prepared by drop casting ~5 μL of nanoparticle dispersion onto a 300 mesh formvar carbon coated copper TEM grid (Ted Pella), followed by solvent evaporation. The size distributions were obtained by image analysis performed with the ImageJ software package[30] counting at least 1500 particles for meaningful and relevant statistics.

Small-Angle Neutron Scattering (SANS)

SANS experiments were performed on the CG-2 General SANS instrument at the High Flux Isotope Reactor (HFIR) at Oak Ridge National Laboratories (ORNL, Oak Ridge, TN). All samples were prepared to be 1% by volume and considered dilute. Each sample was loaded into a 2 mm path length banjo cell and measured at 25, 37, and 50 °C. Two sample-to-detector distances were used for the 25 and 37 °C measurements (0.3 m and 6 m) to obtain a q range from ~0.007 to 0.67 $Å^{-1}$ with a neutron wavelength of $\lambda = 6$ Å. An additional sample-to-detector distance of 14.5 m and a neutron wavelength of 18Å

was used for the 50 °C measurements at to expand the q range to ~0.001 $Å^{-1}$. The neutron resolutions, $\Delta\lambda/\lambda$, were equal to 12% (FWHM). Empty beam background, empty cell background, solvent (deuterium oxide) background, detector sensitivity, sample transmission, and sample thickness were considered during raw data reduction. The solvent and empty cell background measurements were used to normalize all SANS data. The reduced scattering intensities, I(q), were fit as a function of the scattering vector, q(θ). Here, $q(\theta) = 4\pi\sin(\theta)/\lambda$ and θ is defined as the scattering angle. All SANS fitting was performed using Igor Pro 6.03 software and models provided by NIST.[31]

In order to determine the impact of small hydrophobic nanoparticles embedded into a lipid bilayer (change in bilayer thickness), a lamellar model was used for all SANS spectra.[32] In the lamellar model, the bilayer thickness (T_{BL}), polydispersity of T_{BL}, were set as adjustable parameters, while the solvent SLD (SLD_{solv}) for deuterium oxide and the hydrogenated phospholipid bilayers (SLD_{BL}) were held to be 6.33 x 10^{-6} $Å^{-2}$ and -2.77 x 10^{-7} $Å^{-2}$, respectively. Figure 6.3 shows the adjustable parameters used in the lamellar model. For an in depth discussion of the lamellar model, see Appendix A.

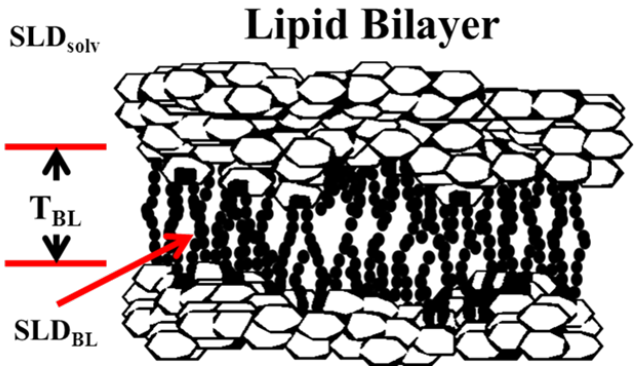

Figure 6.3: Schematic of the lamellar model used for SANS data analysis

Results and Discussion

DPPC/DPPG-GNP Lipid Vesicles

Figure 6.4 shows fit SANS data for the DPPC/DPPG control vesicle solutions using a lamellar model[32] at 25 °C, 37°C, and 50 °C. Figure 6.5 shows fit SANS spectra for the 3.9 nm GNPs partitioned into the DPPC/DPPG bilayer with varying temperatures and loading ratios. A noticeable increase in scattering intensity is observed at low q (between 0.001 and 0.004 $Å^{-1}$) for the control DPPC/DPPG vesicles, compared to the DPPC-GNP concentrations of 10,000:1 and 5,000:1 suggesting an increase in vesicle size (50 °C). Based on the SANS spectra, the vesicles are larger than 1200 Å in diameter; however, the exact diameter could not be determined due to the polydispersity of vesicles in solution and presence of large aggregates of vesicles (decreasing intensity with increasing q is evident at the low q range in place of the expected Guinier regions are observed in the SANS spectra). Dynamic light scattering (DLS) studies performed by Bothun demonstrated that the mean vesicle size in solution increases with decreased lipid to nanoparticle ratios (measured to be between 1000 and 1500 Å in diameter),[17] and supports the increase in scattering intensity measured in the SANS spectra.

Table 6.1: Bilayer thickness values determined from SANS spectra for varying lipid vesicles systems measured at varying temperatures.

lipid sample	T_{BL} (Å), 25 °C	T_{BL} (Å), 37 °C	T_{BL} (Å), 50 °C
DPPC/DPPG Control	43.8 ± 6.8	43.6 ± 7.3	40.2 ± 10.2
DPPC/DPPG 3.9 nm GNPs 10K:1	44.2 ± 7.2	43.9 ± 7.3	40.0 ± 12.0
DPPC/DPPG 3.9 nm GNPs 5K:1	44.9 ± 8.8	44.2 ± 7.9	39.9 ± 1.9
DPPC/DPPG 4.2 nm GNPs 10K:1	43.6 ± 8.3	43.2 ± 6.8	38.9 ± 10.3
DPPC/DPPG 4.2 nm GNPs 5K:1	40.6 ± 6.5	41.3 ± 6.3	38.7 ± 9.3
DPPC/DPPG 4.2 nm GNPs 5K:1 w/cholesterol	44.1 ± 7.7	45.2 ± 6.6	46.6 ± 8.1

Figure 6.6 shows a bar chart for T_{BL} of DPPC/DPPG vesicles with varying temperature and GNP loading. As expected, T_{BL} decreases with increasing temperature for the DPPC/DPPG control sample, from 43.8 ± 6.8 Å to 40.2 ± 10.2 Å between 25 °C to 50 °C, respectively. Table 6.1 shows a summary of all of T_{BL} for all of the SANS spectra collected. When 3.9 nm GNPs are embedded into the lipid bilayer, an increasing trend is noticeable for T_{BL} at 25 °C and 37 °C. Figure 6.6A shows the T_{BL} measured at 25 °C and a loading of 10,000: 1 to be 44.2 ± 7.2 Å. The T_{BL} was shown to increase at a loading of 5,000:1 to 44.9 ± 8.8 Å, also at 25 °C. Near the rippled transition stage for DPPC (37 °C), T_{BL} increases as the ratio of lipids to nanoparticles decreases—the same trend is noted for 25 °C. Interestingly, the T_{BL} values measured at 50 °C for the DPPC/DPPG vesicles with GNPs were smaller than the control and larger for the 10,000:1 sample compared to the 5,000:1 suspension (Figure 6.6A).

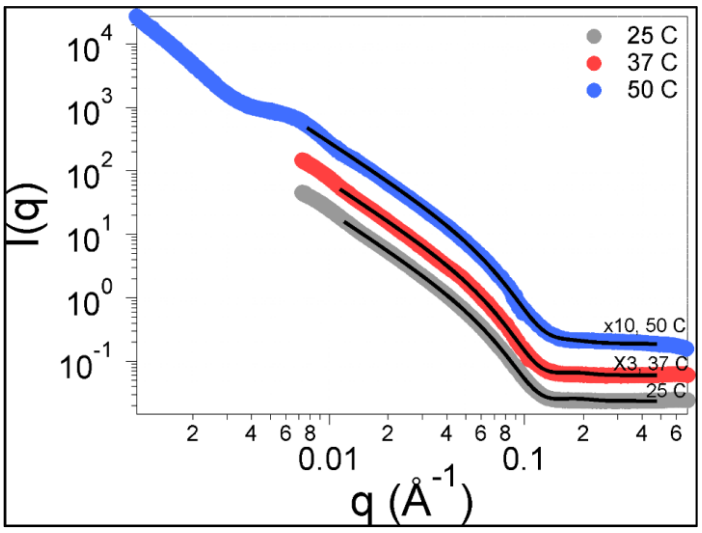

Figure 6.4: SANS spectra fit with a lamellar model for DPPC/DPPG vesicles (~ 1000 Å in diameter) dispersed in deuterium oxide with varying temperature.

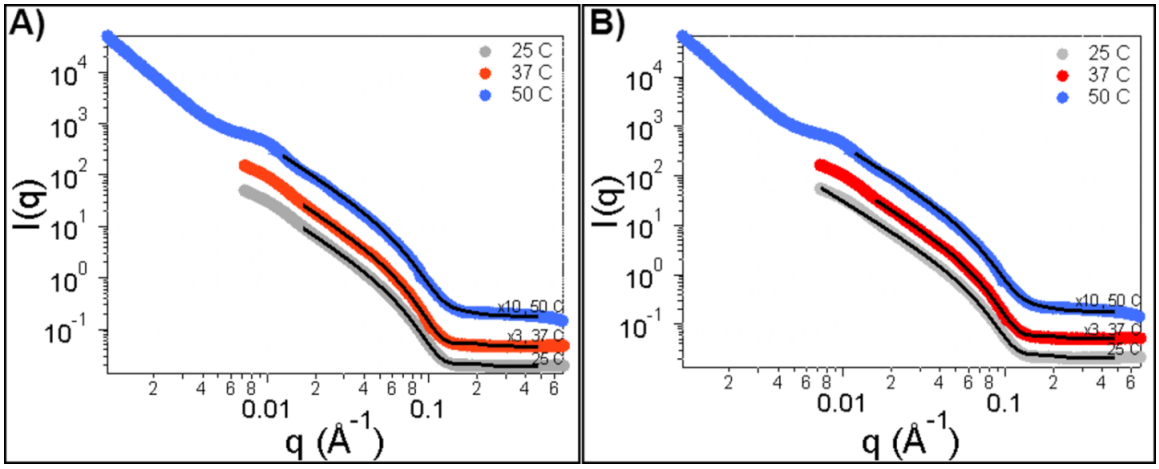

Figure 6.5: Fit SANS spectra for DPPC/DPPG vesicles with 3.9 nm gold nanoparticles partitioned into the bilayer at loading ratios of A) 10,000:1 and B) 5,000:1 lipids to nanoparticle measured at varying temperatures.

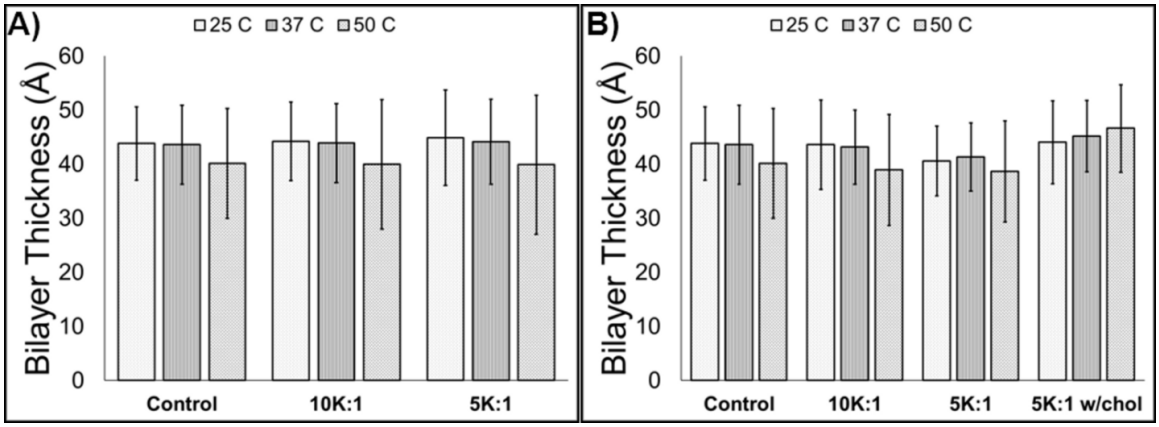

Figure 6.6: Bilayer thickness results for DPPC/DPPG lipid vesicles with varying A) 3.9 nm and B) 4.2 nm gold nanoparticle loadings measured at varying temperatures and with cholesterol added as a stabilizer.

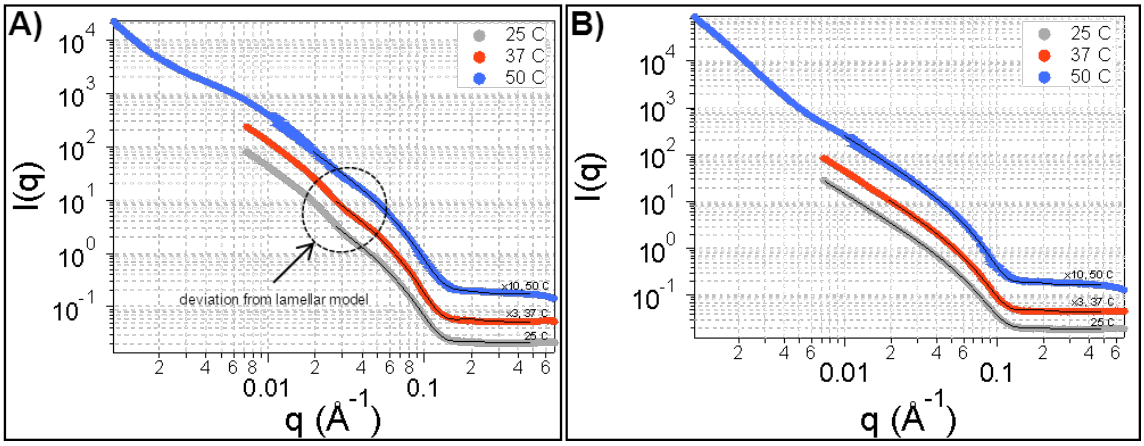

Figure 6.7: Fit SANS spectra for DPPC/DPPG vesicles with 4.2 nm gold nanoparticles partitioned into the bilayer at a loading ratio 5,000:1 lipids to nanoparticle measured at varying temperatures A) without cholesterol, and B) with cholesterol added as a stabilizing agent.

Temperature increases have been shown to increase the fluidity of the DPPC bilayer,[16] the addition of small nanoparticles has been shown to enhance this effect.[16, 17] Park et al. demonstrated a concentration dependent increase in bilayer fluidity for 3 - 4 nm stearylamine stabilized GNPs (similar to those studied in this investigation).[16] The fluid state of the lipids may enable free movement of the GNPs within the bilayer, inducing GNP cluster formation. We hypothesize that small centrally localized clusters of GNPs within the DPPC/DPPG bilayer will provide a lower mean T_{BL} compared to evenly distributed GNPs, and may explain the smaller measured T_{BL} value at 50 °C, compared to the lower temperatures. Further investigation of nanoparticle location and clustering effects within the bilayer can be achieved with cryo-TEM and DLS experiments.

Thermodynamic modeling has predicted that nanoparticles up to 8 nm in diameter may be accommodated into a lipid bilayer.[33] Park et al. calculated the theoretical size of

the bilayer to be 41.2 Å in thickness.[16] In addition to 3.9 nm GNPs, we also loaded 4.2 nm GNPs into the DPPC/DPPG bilayer to determine if noticeable changes in T_{BL} are measureable. We expect the 4.2 nm GNPs to readily partition into the DPPC/DPPG bilayer at 25 °C; however, they may be too large when the bilayer decreases at elevated temperatures (50 °C).[34] Figure 6.6B shows the T_{BL} values for 4.2 nm GNPs at varying temperatures and loading ratios. As expected, we observed that increasing temperature results in decreases in T_{BL} with increasing nanoparticle loading. However, the SANS data obtained from the 4.2 nm GNPs demonstrates a decrease in T_{BL} compared to the control sample for all temperatures studied. Bothun demonstrated that the affinity of the hydrophobic surface chemistry of the GNPs for the acyl chains of the lipids directly disrupts bilayer formation.[17] The larger size of the 4.2 nm GNPs compared to the 3.9 nm GNPs previously described, likely have a lower efficiency at partitioning into the DPPC bilayer (more so when considering the polydispersity of the sample). A change in scattering intensity near 0.03 $Å^{-1}$ is observed for the vesicles with 4.2 nm GNPs loaded at 5,000:1, which deviates from the lamellar model (all temperatures, see Figure 6.7A). The Guinier region expected for a 4.2 nm GNPs is expected to begin at ~0.03 $Å^{-1}$ and the change in scattering intensity is likely caused by lipid capped GNPs. During DLS analysis of DPPC lipid vesicles with silver nanoparticles partitioned into the bilayer, Bothun observed scattering from objects similar in size to DPPC capped nanoparticles.[17] This work suggests that larger sized nanoparticles may not partition into the DPPC bilayer, and instead become coated in a monolayer of lipids enabling their dispersibility in aqueous solution.[17] Hence, the deviations in the scattering spectra caused by the lipid

capped GNPs may cause the lamellar model to be less accurate in predicting the bilayer thickness, and may explain the decreased T_{BL} compared to the DPPC/DPPG control.

DPPC/DPPG-GNP Lipid Vesicles with Cholesterol

4.2 nm GNPs were also embedded into the bilayers of DPPC/DPPG vesicles with cholesterol present as a stabilizer (5,000: 1). Figure 6.6B shows a bar graph of T_{BL} with varying temperature. T_{BL} increases with variation in temperature, noticeably different from the samples without cholesterol. Cholesterol has been shown to cause an increase in T_{BL} by 3 to 4 Å for DMPC lipid vesicles as it orients perpendicular to the membrane minimizing any tilted orientation of lipids and therefore also increases the fluidity of the bilayer.[35] The change in T_{BL} induced by cholesterol may be more noticeable at elevated temperatures (due to negation of the lipid tilt orientation) and therefore may explain the reverse in T_{BL} for variation in temperature. No change in scattering intensity near 0.03 $Å^{-1}$ is present in the SANS spectra for vesicle solutions containing cholesterol (Figure 6.7B). This suggests that cholesterol has increased the stability of the vesicles in solution and minimized the formation of lipid capped GNPs, compared to the 5,000:1 DPPC/DPPG sample (4.2 nm GNPs). The increase in stability for the DPPC/DPPG vesicles is likely a result of the increased bilayer thickness induced by cholesterol addition. Future studies should include measuring the T_{BL} for DPPC/DPPG vesicles with cholesterol present to quantify how thick the DPPC/DPPG bilayer is without nanoparticles present. This would facilitate a better understanding of the effects of GNPs on the bilayer.

Conclusions

This present work utilized SANS to determine the effects of GNP loading on T_{BL} for DPPC/DPPG and DPPC/DPPG with cholesterol. For DPPC/DPPG vesicles, increased concentrations of 3.9 nm GNPs stabilized by stearylamine lead to an increase in T_{BL} for samples measured at 25, 37, and 50°C compared to the control vesicle sample. A decrease in T_{BL} was observed for the larger 4.2 nm GNPs partitioned into the bilayer, along with variation in SANS scattering intensity near 0.03 $Å^{-1}$ (indicative of lipid capped nanoparticles). These results support previous findings which suggest that larger nanoparticles may partition into the lipid bilayer at lower efficiency than smaller nanoparticles. In general, T_{BL} decreased with increasing temperature as expected. Comparatively, the T_{BL} was observed to increase with increasing temperature when cholesterol is added as a stabilizing agent and suggests further investigation is necessary to better understand lipid ordering. The results from this work are useful to applications which propose to use lipid vesicles as transport vehicles for hydrophobically modified nanoparticles in nanomedicine. These results also provide substantial reasoning to support further investigation on T_{BL} changes.

References

(1) Liu, J.; He, F.; Gunn, T. M.; Zhao, D.; Roberts, C. B. *Langmuir* **2009** *25* 7116–7128.

(2) Sook, Y. M.; Kusunose, T.; Sekino, T. *Mater. Lett.* **2009** *63* 2038-40.

(3) Jana, N. R.; Chen, Y.; Peng, X. *Chem. Mater.* **2004** *16* 3931-5.

(4) Pileni, M. P.; Jiang, X. C. *Colloids Surf. , A* **2007** *295* 228-32.

(5) Murphy, C. J.; Sau, T. K.; Gole, A. M.; Orendorff, C. J.; Gao, J.; Gou, L.; Hunyadi, S. E.; Li, T. *J. Phys. Chem. B* **2005** *109* 13857-70.

(6) Boca, S. C.; Astilean, S. *Nanotechnol.* **2010** *21* 235601 (8 pp.).

(7) Shukla, R.; Nune, S. K.; Chanda, N.; Katti, K.; Mekapothula, S.; Kulkarni, R. R.; Welshons, W. V.; Kannan, R.; Katti, K. V. *Small* **2008** *4* 1425-36.

(8) Ding, H.; Yong, K.; Roy, I.; Pudavar, H. E.; Law, W. C.; Bergey, E. J.; Prasad, P. N. *J. Phys. Chem. C* **2007** *111* 12552-12557.

(9) Dickerson, E. B.; Dreaden, E. C.; Huang, X.; El-Sayed, I. H.; Chu, H.; Pushpanketh, S.; McDonald, J. F.; El-Sayed, M. A. *Cancer Lett.* **2008** *269* 57-66.

(10) Rosensweig, R. E. *J. Magn. Magn. Mater.* **2002** *252* 370-374.

(11) Bhattacharya, R.; Patra, C. R.; Earl, A.; Wang, S.; Katarya, A.; Lu, L.; Kizhakkedathu, J. N.; Yaszemski, M. J.; Greipp, P. R.; Mukhopadhyay, D.; Mukherjee, P. *Nanomed. Nanotechnol. Biol. Med* **2007** *3* 224-38.

(12) Urbina, M. C.; Zinoveva, S.; Miller, T.; Sabliov, C. M.; Monroe, W. T.; Kumar, C. S. S. R. *J. Phys. Chem. C* **2008** *112* 11102-11108.

(13) Nadagouda, M. N.; Varma, R. S. *Green Chem.* **2008** *10* 859-862.

(14) Rasch, M. R.; Rossinyol, E.; Hueso, J. L.; Goodfellow, B. W.; Arbiol, J.; Korgel, B. A. *Nano Lett.* **2010** *10* 3733-3739.

(15) Cabral, H.; Kataoka, K. *Sci. Technol. Adv. Mater.* **2010**, *11*, 014109.

(16) Park, S.; Oh, S.; Mun, J.; Han, S. *Colloids Surf. , B* **2006** *48* 112-118.

(17) Bothun, G. D. *J. Nanobiotech* **2008** *6* 13.

(18) Wijaya, A.; Hamad-Schifferli, K. *Langmuir* **2007** *23* 9546-9550.

(19) Bothun, G. D.; Rabideau, A. E.; Stoner, M. A. *J. Phys. Chem. B* **2009** *113* 7725-7728.

(20) Hossann, M.; Wang, T.; Wiggenhorn, M.; Schmidt, R.; Zengerle, A.; Winter, G.; Eibl, H.; Peller, M.; Reiser, M.; Issels, R. D.; Lindner, L. H. *J. Controlled Release* **2010** .

(21) Chen, Y.; Bose, A.; Bothun, G. D. *ACS Nano* **2010** *4* 3215-3221.

(22) Hammouda, B. Probing Nanoscale Structures: the SANS Toolbox. *book available online at: www.ncnr.nist.gov/staff/hammouda/the_SANS_toolbox.pdf* (accessed October 20, 2010).

(23) Kiselev, M. A.; Zemlyanaya, E. V.; Aswal, V. K.; Neubert, R. H. H. *Eur. Biophys. J.* **2006** *35* 477-93.

(24) Kucerka, N.; Kiselev, M. A.; Balgavy, P. *Eur. Biophys. J.* **2004** *33* 328-34.

(25) Boggara, M., B.; Krishnamoorti, R. *Langmuir* **2010** *26* 5734-5745.

(26) Jana, N. R.; Gearheart, L.; Murphy, C. J. *J. Phys. Chem. B* **2001** *105* 4065-7.

(27) Liu, J.; Anand, M.; Roberts, C. B. *Langmuir* **2006** *22* 3964-3971.

(28) Korgel, B. A.; Fullam, S.; Connolly, S.; Fitzmaurice, D. *J Phys Chem B* **1998** *102* 8379-88.

(29) White II, G. V.; Kitchens, C. L. In Preparation **2010** .

(30) Abramoff, M. D.; Magalhaes, P. J.; Ram, S. J. *Biophoton Int.* **2004** *11* 36-41.

(31) Kline, S. R. *J. Appl. Crystallogr.* **2006** *39* 895-900.

(32) Berghausen, J.; .Zipfel, J.; Lindner, P.; Richtering, W. *J. Phys. Chem. B* **2001** *105* 11081-11088.

(33) Ginzburg, V. V.; Balijepalli, S. *Nano Lett.* **2007** *7* 3716-3722.

(34) Kucerka, N.; Nagle, J. F.; Sachs, J. N.; Feller, S. E.; Pencer, J.; Jackson, A.; Katsaras, J. *Biophys. J.* **2008** *95* 2356-67.

(35) Leonard, A.; Escrive, C.; Laguerre, M.; Pebay-Peyroula, E.; Neri, W.; Pott, T.; Katsaras, J.; Dufourc, E. J. *Langmuir* **2001** *17* 2019-2030.

CHAPTER SEVEN

CONCLUSIONS AND RECOMMENDATIONS

Conclusions

This work provides the first *in-situ* measurements of ligand structure and solvation under anti-solvent conditions which mimic the precipitation process using SANS. We show that increasing the anti-solvent composition (CO_2 or ethanol), leads to decreases in ligand length and solvation for both dodecanethiol and octadecanethiol, respectively. The weakened solvent strength, caused by ethanol or CO_2 addition, induces a decrease in ligand length for both dodecanethiol and octadecanethiol ligands on both gold and silver nanoparticles. The SANS results demonstrate that the driving force for anti-solvent precipitation is the simultaneous decrease in ligand length and solvation and is the same for both the liquid-liquid and gas-liquid processes. Overall, the SANS investigations showed that nanoparticle dispersibility is a function of ligand surface coverage, nanoparticle curvature (size), and chain length. During this investigation, we confirm that nanoparticles can be fractionated based on size, as well as fractionation based on degree of ligand surface-coverage.

We anticipate that the results obtained from the SANS experiments will lead to the development of more accurate interaction energy models aimed at predicting nanoparticle dispersibility at defined solvent compositions, ligand length, metal type, varying surface coverage, and nanoparticle size and shape. These models will lead to decreased nanoparticle processing times, and potentially to the development of new nanoparticle synthesis procedures in GXLs.

This work also demonstrates the first ever gold nanorod fractionation using GXLs. This technique is highly advantageous because it is pressure tunable, and resulted in both increases in GNR sample monodispersity and removal of excess seed nanoparticles. GNR dispersibility was also investigated as a function of A) solvent choice, including CO_2-expanded cyclohexane, toluene, and *n*-hexane, and B) ligand length comparing 12 carbon chains to 18 carbon chains. These results will prove useful to nanoparticle applications which may benefit from rod shaped nanoparticles, for example polymer nanocomposites. We hope that this technique can be used to create a new class of nanomaterials which utilizes the unique properties of GNRs,

The research performed within this dissertation also presents a facile synthesis procedure for silver nanoparticles using garlic extracts, and follows Green Chemistry Principles. Variation of the garlic extract quantity employed during synthesis was shown to enable control over nanoparticle size and size-distribution. These nanoparticles proved to be stable in biological media and showed high oxidation resistance against H_2O_2 providing evidence that they may be suitable candidates for *in vivo* therapies. Future work may also employ these garlic stabilized silver nanoparticles in studies which aim to distinguish the toxicities between silver ions and silver nanoparticles.

Lastly, we used SANS to investigate the effect of gold nanoparticle loading on hybrid lipid-vesicle systems composed of DPPC/DPPG lipids which have the potential to be used as nanotherapies delivery devices. The SANS results demonstrate that increased nanoparticle loading resulted in increased bilayer thicknesses and correlated to increase bilayer fluidity. These results suggest that further work must be performed to develop

better vesicle-nanoparticle delivery devices, as high membrane fluidity can negatively impact the membrane transport properties—and hence the application of the vesicles. As expected, increases in temperature led to decreases in bilayer thickness, with the exception to those vesicles which were stabilized by cholesterol.

Recommendations

After completing this dissertation, a fundamental question has revealed itself after analyzing the SANS data for ligand solvation. Though interaction energy models will directly benefit from the results presented in this work, I am confident that further understanding is necessary with respect to preferential solvation within the solvent mixtures. We were unsuccessful in determining if anti-solvent conditions caused localized solvation by the "good" solvent, i.e. is there a hexane rich portion of the ligand shell when CO_2 is added to a GXL dispersion?

One potential approach to determine preferential solvation would be to perform SANS on either hydrophobically modified nanoparticles or alkane chains adsorbed to a substrate (silica or gold). The solvent conditions would need to be varied as previously demonstrated; however, contrast matching must also be employed. For example mixtures of deuterated hexane and hydrogenated hexane can be used with hydrogenated ligands. The same measurement would be nicely complemented by using deuterated ligands and hydrogenated solvents, though this approach may prove to be more expensive. In the event that monolayers of alkane chains are used instead of hydrophobically stabilized nanoparticles, advanced neutron diffractometer/reflectometer (AND/R) may be used in

place of SANS. This experiment may afford the use of a step function to model the solvent composition with respect to the axial length of the ligand shell.

I also recommend that a detailed and mechanistic investigation should be performed for the synthesis of gold nanoparticles in a gas-expanded liquid. My first experiment would employ hydrophobic amines as the phase transfer catalysts (for example stearylamine) and stabilizing agents to move aqueous gold ions into toluene. I would then add CO_2 to the toluene solution of hydrophobically stabilized ions to a pre-determined pressure (50 to 100 psi would be a good starting point). If no nucleation step occurs, 4-hexadecylaniline could be used as a reducing agent to catalyze nanoparticle synthesis, and could be readily added to the GXL mixture using a metering pump or injection loop. Sodium borohydride ($NaBH_4$) could also be used in lieu of 4-hexadecylaniline. I would avoid attempting to perform the Brust method in a GXL due to the high cost and quantity of TOAB surfactant needed.

With respect to gold nanorod processing, I believe the next logical step in the research is to investigate the precipitation conditions necessary to deposit wide-area arrays of GNRs. This would be beneficial because it could provide the opportunity for the development of a new nanoparticle device. Because the GNRs are hydrophobic, this device could be a biosensor as it should not degrade in aqueous media. Plasmon resonance changes could be measured by UV-VIS.

The work performed investigating the synthesis of silver nanoparticles using garlic extract demonstrated a unique potential for phytochemicals to replace the traditionally employed reagents used within our group. Moreover, they proved to

increase compatibility with biological media and had high oxidation resistance. Future work should include further exploring the reduction and stabilizing capabilities of the garlic extract. One proposed goal would be to synthesize non-spherical nanoparticles using biocompatible polymers (Pluronics for example), and would provide an alternative to wet-chemical synthesis procedures which employ CTAB. My first experiment would utilize gold or silver salts as the precursor metals, garlic extract as the reducing and stabilizing agents, and pluronic as the shape directing surfactant. If this experiment does not provide positive results, a seed mediated approach could also be investigated using garlic extract stabilized nanoparticles as the seeds in combination with another shape directing surfactant (Triton X100).

Future experiments may also include incorporating GNRs into PLA polymer (cast films or extruded polymer). Any approach for this work should utilize hydrophobically stabilized GNRs, either by surface modification or through synthesis. Chloroform has been shown to readily dissolve PLA and would be my first solvent choice for dispersing both PLA and GNRs in the same solution. I hypothesize that the hydrophobic surface chemistry of the GNRs will afford well dispersed nanoparticles within the polymer matrix when dry. However, if this is not the case, one may attempt to better disperse the GNRs within the PLA matrix by either rapidly spraying the PLA/GNR mixture into super critical CO_2 to facilitate encapsulation, or using super critical drying techniques (replacing the chloroform with liquid CO_2 and then removal of the CO_2). The PLA/GNR nanocomposites should have enhanced surface plasmon resonance, increased stiffness, and photothermal activity making a new type of nanomaterial.

APPENDICES

APPENDIX A

SANS THEORY AND MODELS

The scattering intensity, I(q), of neutrons collected during a small-angle neutron scattering (SANS) experiment is described as:

$$I(q) = \varphi P(q) S(q) \qquad \textbf{(A1)}$$

Here, φ is the volume fraction of the particles in the solution (i.e. nanoparticle concentration). The form factor P(q) describes the size and shape of the particles in solution (several form factors will be discussed later). The structure factor, S(q), describes any particle-particle interactions (for example attractive forces). For dilute samples of particles in solution ($\varphi = 1\%$), S(q) is assumed to be unity and therefore only a form factor is required to describe I(q). The scattering variable, $q = (4\pi/\lambda)\sin(\theta/2)$, units of $Å^{-1}$.

Sphere Model[1]

The spherical model calculates the form factor, P(q), for monodisperse spherical particles with uniform scattering length density (SLD). The form factor is normalized by the particle volume, $V = (4\pi/3)r^3$.

$$P(q) = \frac{scale}{V}\left[\frac{3V(\Delta\rho)(\sin(qr)-qr\cos(qr)}{(qr)^3}\right] + bkg \qquad \textbf{(A2)}$$

The adjustable parameters in the sphere model are the scale, particle radius, r (Å), scattering length density (SLD, $Å^{-2}$) of the particle sphere SLD_{core}, the solvent SLD_{solv}, and the background (bkgd, cm^{-1})—see Figure A1. Here, $\Delta\rho = SLD_{core} - SLD_{solv}$. In general practice, the scale is set equal to φ, thus $I(q) = \varphi P(q)$, though this is not required.

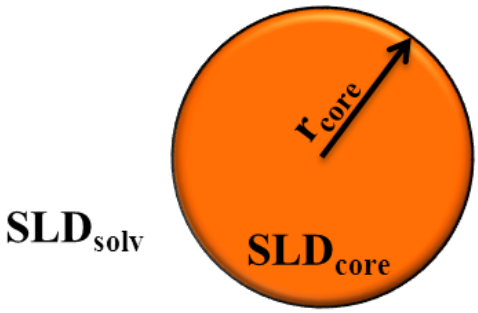

Figure A1: Schematic of the sphere model

Core-Shell Model[1]

The core-shell model calculates the form factor, P(q), for monodisperse spherical particles with a core-shell structure. As with the sphere model, the form factor is normalized by the total particle volume, $V_{shell} = (4\pi/3)r_{shell}^3$. The nanoparticle core volume, $V_{core} = (4\pi/3)r_{core}^3$. This form factor is described as:

$$P(q) = \frac{scale}{V_s}\left[\frac{3V_c(\mathrm{SLD}_{core}-\mathrm{SLD}_{shell})\frac{(\sin qr_{core}-qr_{core}\cos qr_{core})}{qr_{core}^2}(\mathrm{qr}_{core})}{\mathrm{qr}_{core}} + \frac{3V_s(\mathrm{SLD}_{shell}-\mathrm{SLD}_{solv})\frac{(\sin qr_{shell}-qr_{shell}\cos qr_{shell})}{qr_{shell}^2}(\mathrm{qr}_{shell})}{qr_{shell}}\right]^2 + bkg \quad \textbf{(A3)}$$

Here, the adjustable parameters are the scale, core radius (Å), shell thickness (Å), SLD_{core}, SLD_{Shell}, $SLD_{solvent}$, and background (bkg, cm^{-1})—see Figure A2. Here, $r_{shell} = r_{core} + t$.

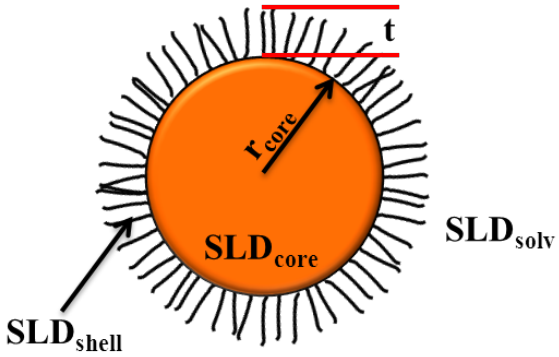

Figure A2: Schematic of the core-shell model

Polydisperse Core-Shell Model[2]

The polydisperse core-shell model calculates the form factor, P(q), for polydisperse core-shell particles with constant shell thicknesses. The form factor is normalized by the average particle volume such that P(q) = scale * <f*f>/Vol + bkg, where f is the single particle scattering amplitude, appropriately averaged over the Schulz distribution of radii. The adjustable parameters are the scale, average core radius (Å), core polydispersity, shell thickness (Å), SLD_{core}, SLD_{shell}, SLD_{solv}, and background (bkg). The returned form factor is normalized by the average particle volume <*V*>:

$$\langle V \rangle = \frac{4\pi}{3}\langle r^3 \rangle \qquad \textbf{(A4)}$$

$$\text{and } \langle r^3 \rangle = \frac{(z+3)(z+2)}{(z+1)^2}\langle r \rangle \qquad \textbf{(A5)}$$

$$\text{where, } z = \left(\frac{1}{p^2}\right) - 1 \qquad \textbf{(A6)}$$

For a more in depth discussion of the Schulz distribution, see J. Hayter in "Physics of Amphiphiles – Micelles, Vesicles, and Microemulsions" V. DeGiorgio and M. Corti, Eds. (1983) p. 69.

Fractal Model[3]

The fractal model calculates the scattering from fractal-like clusters or aggregates in solution which are composed of spherical building blocks. The adjustable parameters within the fractal model are the volume fraction (scale), repeat block radius (Å), fractal dimension (D_f), correlation length (Å), SLD of the block, SLD_{solv}, and the background (bkgd)—see Figure A3.

Here, $I(q) = P(q)S(q) + bkgd$.

$$P(q) = \varphi V_p \Delta\rho^2 F(qR_o)^2 \qquad \textbf{(A7)}$$

$$\text{where, } V_p = \frac{4}{3}\pi {R_o}^3 \qquad \textbf{(A8)}$$

$$\text{and, } F(x) = \frac{3[\sin(x) - x(\cos(x)]}{x^3} \qquad \textbf{(A9)}$$

The spherical building blocks flocculate to form fractal-like clusters. The clusters have a correlation length, L, which corresponds to the size of their short range order, and a fractal dimension of self-similarity, D_f. The particle clustering interactions is calculated by S(q), which is shown below:

$$S(q) = \frac{sin[(D_f - 1)tan^{-1}(qL)]}{(qR_o)^{D_f}} \frac{D_f \Gamma(D_f - 1)}{[1 + 1/(q^2L^2)]^{(D_f - 1)/2}} \qquad \textbf{(A10)}$$

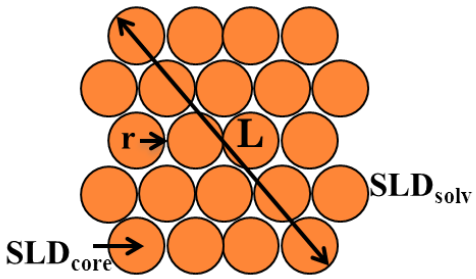

Figure A3: Schematic of the fractal model.

Lamellar Model[4]

The lamellar model calculates the form factor for the lyotropic lamellar phase. The scattering intensity is calculated for the lamellae bilayers of uniform scattering length density, which are randomly distributed in solution. The thickness of the lamellae is polydisperse. The adjustable parameters in the lamellar model are the scale, bilayer thickness ($T_{BL,}$ Å), polydispersity of the thickness, bilayer SLD (SLD_{BL}), SLD_{solv}, and the background (bkdg). Here, the scattering intensity is calculated as:

$$I(q) = \frac{2\pi P(q)}{T_{BL}q^2} \qquad \textbf{(A11)}$$

$$\text{where, } P(q) = \frac{2\Delta\rho^2}{q^2}\left[1 - \cos(qT_{BL})\, e^{-q^2\sigma^2/2}\right] \qquad \textbf{(A12)}$$

σ = variation in T_{BL} or T_{BL}* polydispersity. Δρ is the difference in SLD_{BL} and $SLD_{solv.}$

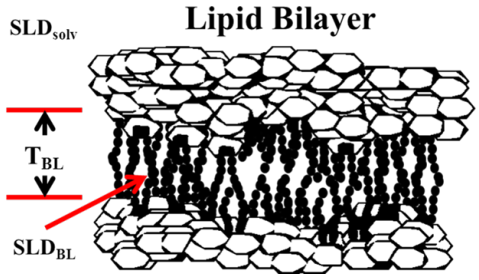

Figure A4: Schematic of the lamellar model.

References

(1) Guinier, A. and Fournet, G., Small-Angle Scattering of X-Rays", John Wiley and Sons, New York, 1955.

(2) Bartlett, P.; Ottewill, R. H. *J. Chem. Phys.* **1992** *96* 3306-18.

(3) Teixeira, J. In *In Small-angle scattering by fractal systems;* International Conference on Applications and Techniques of Small-Angle Scattering; Denmark, 1988; Vol. 21, pp 781-5.

(4) Berghausen, J.; .Zipfel, J.; Lindner, P.; Richtering, W. *J. Phys. Chem. B* **2001** *105* 11081-11088.

APPENDIX B

ADDITIONAL SANS RESULTS FOR GOLD AND PALLADIUM NANOPARTICLES IN GAS-EXPANDED HEXANE

In Chapter 3, we discussed the small-angle neutron scattering (SANS) results obtained from four populations of dodecanethiol stabilized silver nanoparticles in gas-expanded *n*-hexane-d_{14} with varying CO_2 mole fractions. In Appendix B, we provide additional results obtained at both the NCNR at NIST (Gaithersburg, MD) and HFIR at ORNL (Oak Ridge, TN) for gold and palladium nanoparticles in gas-expanded *n*-hexane-d_{14}, respectively.

Experimental Methods

Materials

The metal precursor gold (III) chloride hydrate ($HAuCl_4$, 99.99%) was purchased from VWR. The stabilizing agents 1-hexanethiol (>95%) and sodium citrate dihydrate (99%) were purchased from VWR. The reducing agent sodium borohydride ($NaBH_4$, 98%) was also purchased at VWR. *n*-Hexane was purchased from VWR (95%). The deuterated solvent, *n*-hexane-d_{14} was purchased from Cambridge Isotope Laboratories (98%). The CO_2 was obtained from National Welders and was Coleman Grade (99.99%). All chemicals were used without further purification. All glassware used for the synthesis of metallic nanoparticles were washed and rinsed with acetone, rinsed with DI water, and then dried using compressed air.

Gold Nanoparticle Synthesis

Gold nanoparticles (GNPs) were synthesized with a modified Liu method[6]. In short, 200 μL of a 0.05 M $HAuCl_4$ solution was added to 200 μL of a freshly prepared 0.05 M citrate solution. This mixture was then diluted to 20 mL with water. The gold ions were reduced by the addition of 600 μL of ice cold $NaBH_4$ (0.05 M). The resulting solution was ruby red in color, indicative of the presence of GNPs (~4 nm in core diameter).

Subsequent surface modification of the GNPs afforded suspension in *n*-hexane. Briefly, 10 mL of the aqueous GNP dispersion was placed in a test tube, followed by 5 mL of *n*-hexane. Next, 200 μL of hexanethiol was added to the organic phase and the biphasic mixture was vigorously shaken enabling interaction between the thiol group and the surface of the GNPs. The shaking afforded the phase transfer of the nanoparticles into *n*-hexane. The GNP dispersion was purified from excess hexanethiol ligands as previously described for dodecanethiol stabilized silver nanoparticles in Chapter 3. Prior to SANS experiments, the GNPs were dried to a thin film using nitrogen and then redispersed in *n*-hexane-d_{14}.

Palladium Nanoparticles Synthesis

Dr. Juncheng Liu from Dr. Christopher Roberts' research group (Auburn University, AL) provided palladium nanoparticles dispersed in *n*-hexane capped by either dodecanethiol or hexanethiol (reported to be 3.4 ± 0.7 nm and 4.8 ± 0.9 nm, respectively). These particles were precipitated from *n*-hexane using the hexane/ethanol

solvent/anti-solvent pair in combination with centrifugation. The palladium nanoparticles were re-dispersed in *n*-hexane-d_{14} prior to SANS experiments.

GNP Isolation

The GNPs were isolated using the GXL technique described in Chapter 3. Hexanethiol stabilized GNPs were isolated between 600 and 650 psi of CO_2 and were measured to be 4.6 ± 0.8 nm by TEM.

Results and Discussion

Gold nanoparticles capped by hexanethiol (ORNL) and palladium nanoparticles capped by either dodecanethiol or hexanethiol (NIST) dispersed in *n*-hexane-d_{14} were investigated using SANS at varying CO_2 mole fractions. Figure B1 shows the mean core diameter for alkanethiol capped gold and palladium nanoparticles dispersed in solution as a function of CO_2 mole fraction. Figure B1 shows that mean core-diameter of nanoparticles decreases with increasing CO_2 mole fraction.

Figure B2 shows the shell thickness values obtained from the SANS spectra for the dodecanethiol stabilized palladium nanoparticles. The dodecanethiol ligand length at ambient pressure was determined to be between 11 Å. At elevated CO_2 mole fractions, the dodecanethiol shell decreases to ~6.5 Å prior to nanoparticle precipitation. The shorter ligand length of hexanethiol combined with the Q range allowable at high scattering angles (θ) did not provide enough resolution for measurements of the ligand length and shell SLD (SLD_{shell}) for the gold and palladium particles.

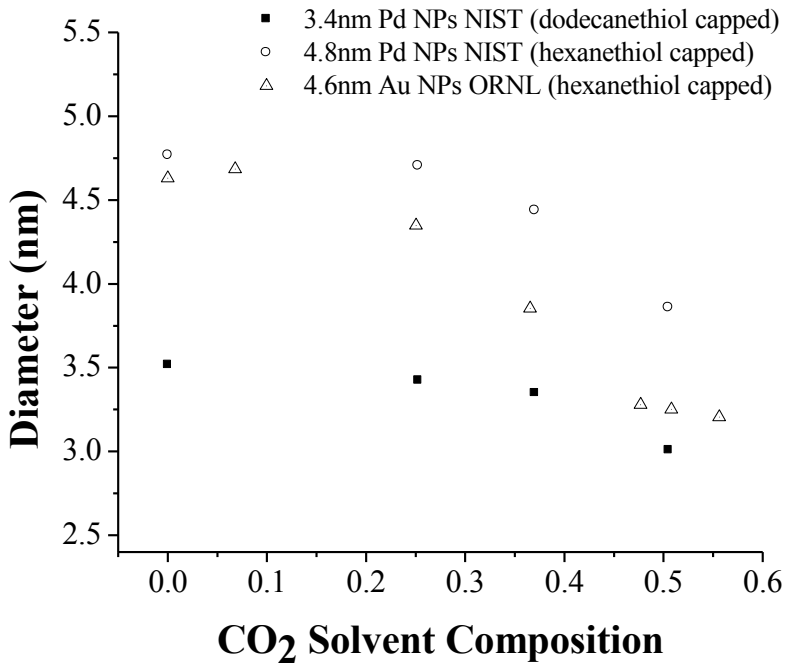

Figure B1: Mean particle diameter for gold and palladium nanoparticles capped by hexanethiol or dodecanethiol dispersed in n-hexane, d14/CO_2 GXL as a function of CO_2 mole fraction.

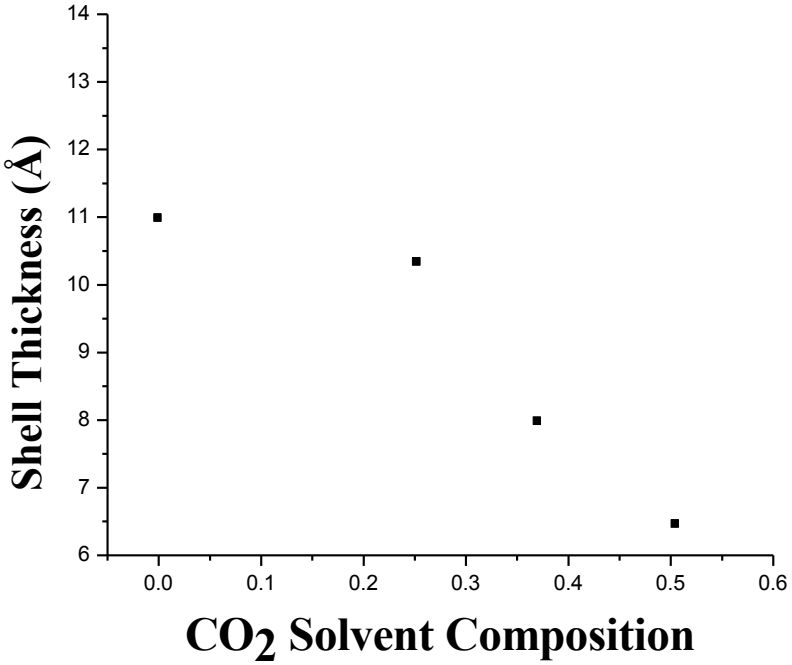

Figure B2: Dodecanethiol shell thickness of palladium nanoparticles with varying CO_2 mole fraction determined from a core-shell model fit of SANS spectra.

The fit values of SLD_{shell} for dodecanethiol on palladium nanoparticles are shown in Figure B3 with varying CO_2 mole fraction. The increase in CO_2 mole fraction results in a decrease in the SLD_{shell}, beginning at ~25% CO_2 mole fraction. The low and even negative SLD_{shell} values at elevated CO_2 mole fractions indicate that the molar composition of the shell is largely composed of the hydrogenated alkanethiol tail opposed to the gas-expanded hexane. Analysis of the SLD_{shell} values as a function of increasing CO_2 mole fraction demonstrates decreasing ligand solvation which supports decreased nanoparticle dispersibility. Using Equation 3.1 from Chapter 3 will yield the dodecanethiol ligand solvation—the shape of the curve is identical to that shown in Figure B3 and is therefore omitted. However, Table B1 shows the ligand solvation data. Corresponding to the decreases in SLD_{shell}, the ligand solvation decreases with increasing CO_2 mole fraction as a result of the weakened solvent conditions.

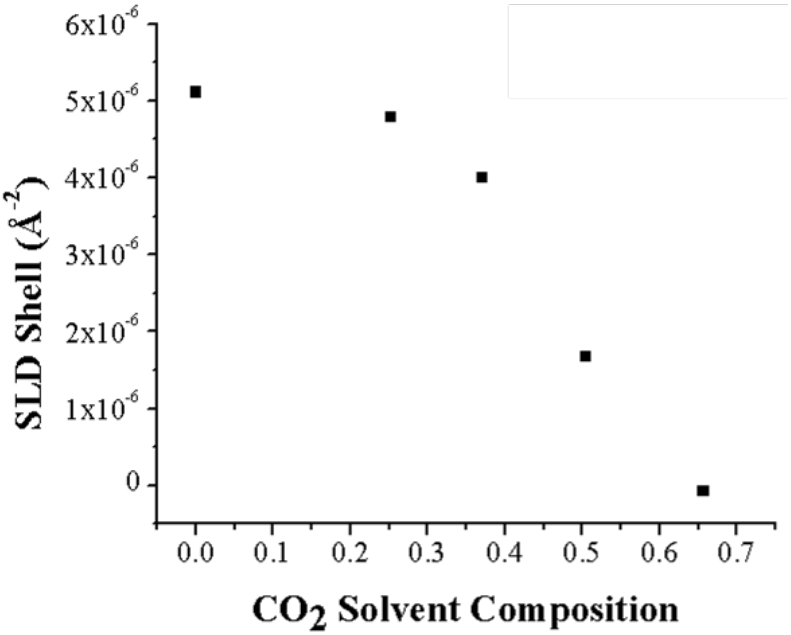

Figure B3: Scattering length densities of dodecanethiol stabilized ligands on 3.4 nm palladium nanoparticles with varying CO_2 mole fraction dispersed in *n*-hexane-d_{14}.

Table B1: 3.4nm Pd NPs capped by dodecanethiol data measured from SANS experiments performed at NIST (core-shell model)

% CO_2	diam. (nm)	SLD_{shell} ($Å^{-2}$)	Shell Thickness (Å)	%Ligand Solvation	χ^2
0	3.52	5.11E-06	11.0	84	2.23
25	3.42	4.79E-06	10.3	85	1.94
37	3.35	4.00E-06	8.0	76	1.85
51	3.01	1.67E-06	6.5	39	1.86
66	2.53	-7.22E-08	6.4	6	1.55

The ligand surface coverage and percent ligand solvation was determined by evaluating the SLD_{shell}, SLD_{solv}, the SLD of dodecanethiol ligand (SLD_{DDT}), and the mean core-diameter values. The mean surface coverage was determined to be 57% for the palladium nanoparticles (see Equation 3.2 in Chapter 3). The ligand solvation of dodecanethiol on the palladium nanoparticles was measured to be 84% at ambient pressure. As the CO_2 mole fraction increased in the GXL, the ligand solvation decreased to approximately 6% prior to nanoparticle precipitation. The large ligand solvation is a result of the *extreme* curvature of the palladium nanoparticle and the low surface coverage (57%).

Conclusions

SANS demonstrated that increasing CO_2 mole fraction result in decreases in the dispersible core-diameter of gold and palladium nanoparticles. The short ligand length and limited q range during SANS experiments prevented the measurement of the ligand structure and solvation of hexanethiol stabilized gold and palladium nanoparticles. We

observed the dodecanethiol ligand shell on palladium nanoparticles to decrease from 11 Å to nearly 6.5 Å prior to precipitation at 66 mol% of CO_2. A core-shell model fit to the SANS spectra demonstrated the dodecanethiol ligand shell to be 84% solvated at ambient pressure—a result of the extreme curvature of the palladium nanoparticle and the low surface coverage (57%). As the CO_2 mole fraction increased in the gas-expanded mixture, the dodecanethiol solvation decreased to nearly 0% prior to nanoparticle precipitation.

References

(1) Liu, J.; Anand, M.; Roberts, C. B. *Langmuir* **2006** *22* 3964-3971.

APPENDIX C

TRANSMISSION ELECTRON MICROSCOPE OPERATING PROCEDURES

Getting Started

- Ensure both liquid nitrogen traps are full. One is located on the rear of the microscope and the other is near the condenser stage. I topped off both traps at least every hour during experimentation.

- Ensure the accelerating voltage is at least 100 kV. For the images obtained in this dissertation, 120 kV was always used.

- Turn on the filament current, and make sure that the filament bias is on.

- Place your sample in the sample holder and load into the "standby" position within the column.

Alignment Procedure for Imaging Mode

- Ensure the objective and diffraction apertures are in the out position

- Ensure that you are at the lowest magnification setting (far left controller on left panel turned all the way counter clockwise)

- Push the beam horizontal button, BH, on the right hand panel, and then use the multifunction xy knobs to center the brightly focused beam. If you cannot see the beam, adjust the brightness (middle knob on the left panel) until it is a small focused spot.

- Align the condenser using the two xy screws located on the aperture (this is the large metal knob located at the right/middle section of the column well above head level when seated).

- Systematically increase the brightness and simultaneously increase the magnification until you are at 600 kx magnification. Each time the magnification is increased, the spot size will also increase, but light intensity will decrease.

- Insert your sample by rotating it clockwise enabling it to fully load into the column

- Decrease the magnification to ~100 kx and find something to focus on. Nanoparticles are a good choice!

- Increase the magnification until the object of interest is reasonably visible

- Press the wobble button, WOB, and adjust the Z control knob to adjust the height of your sample until your specimen stops moving

- Toggle off the wobble button, WOB

- Turn on modulation, MODU, and adjust the xy knobs until your specimen stops moving—this ultimately controls the beam tilt. The small knobs will now control the beam tilt.

- Toggle off modulation, MODU

- Re-evaluate the beam alignment. If it is not centered, use the xy controls to re-center the beam.

- Press the IN/OUT button to insert the aperture

- Find another specimen on to evaluate on the sample and turn on the monitor for imaging mode, and insert the camera.

- Begin taking images with the AMT Camera..

APPENDIX D

IMAGEJ ANALYSIS

ImageJ is a commercially freeware software which enables the user to measure nanoparticle size and shape. Here I outline the basic steps for successful nanoparticle sizing.

1) Set scale

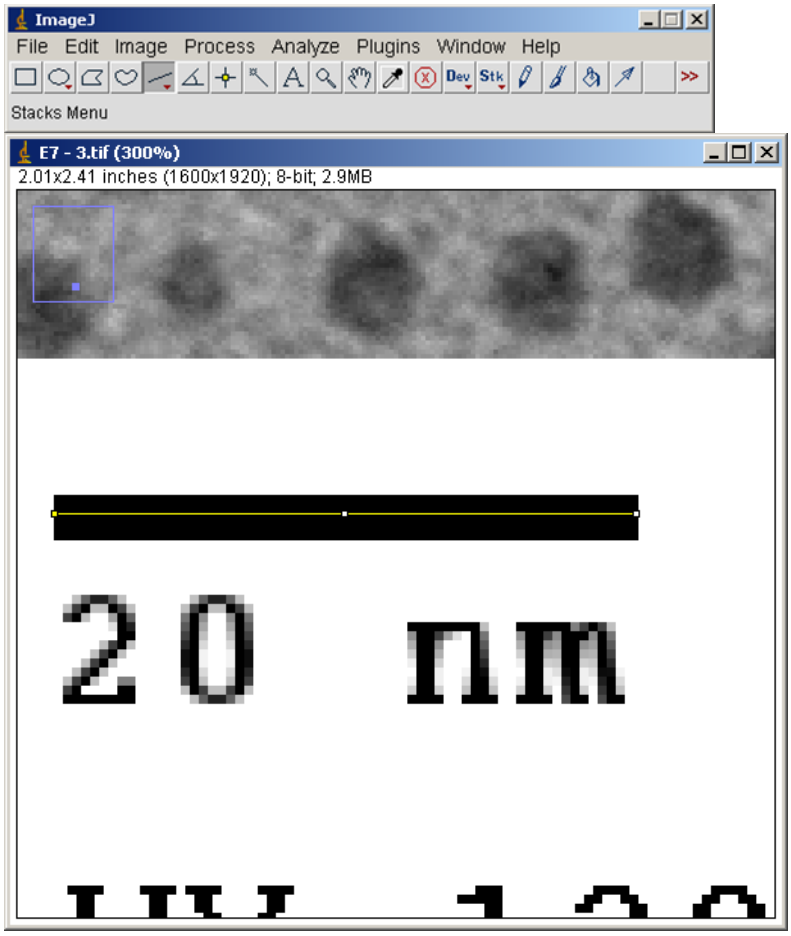

CLICK >>Analyze >> Set Scale

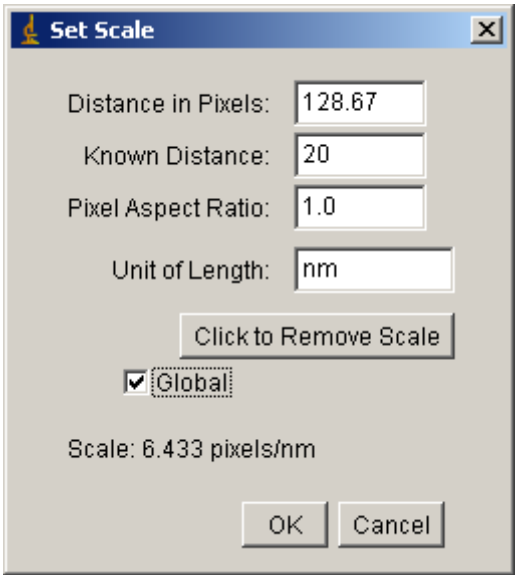

Adjust Threshold until your particles look nice and circular
CLICK >> Image >> Adjust Threshold

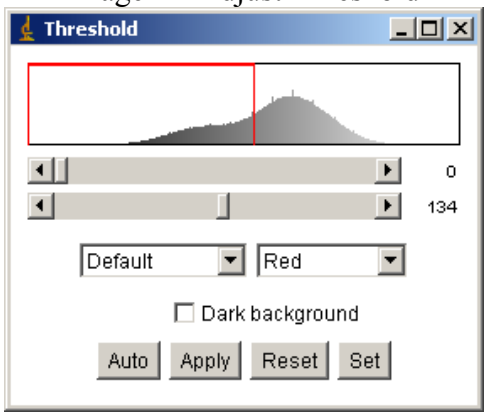

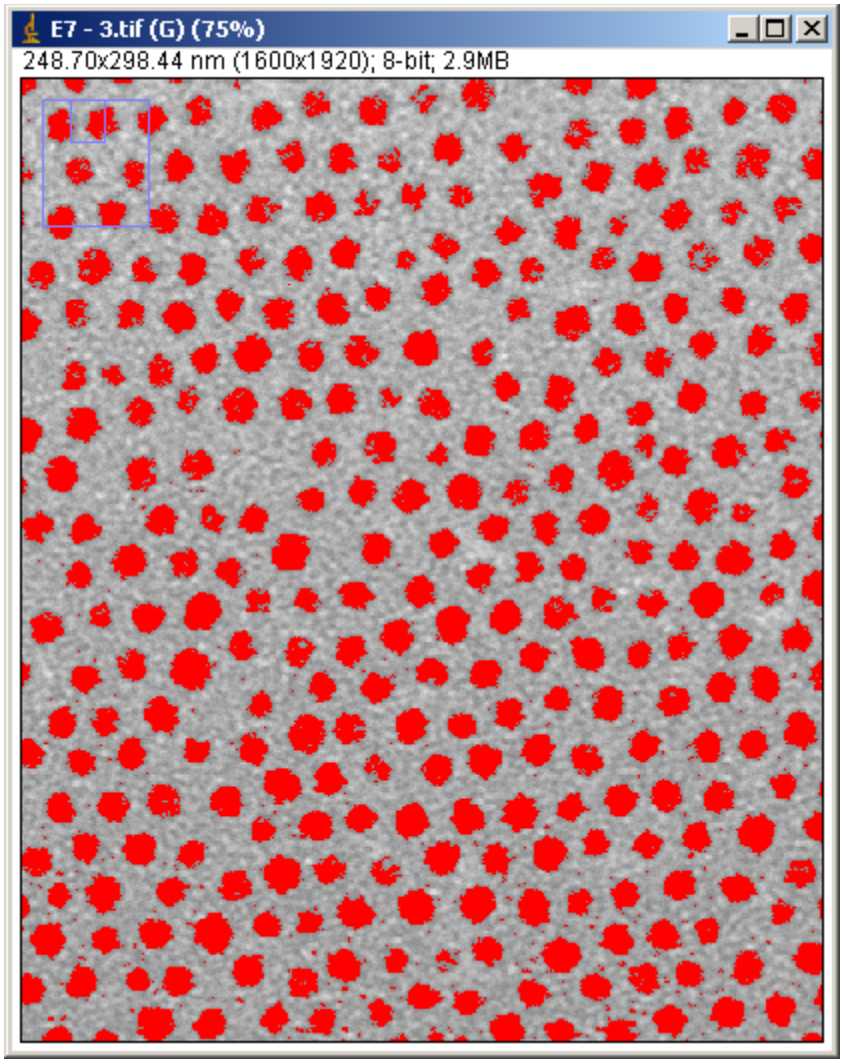
E7 - 3.tif (G) (75%)
248.70x298.44 nm (1600x1920); 8-bit; 2.9MB

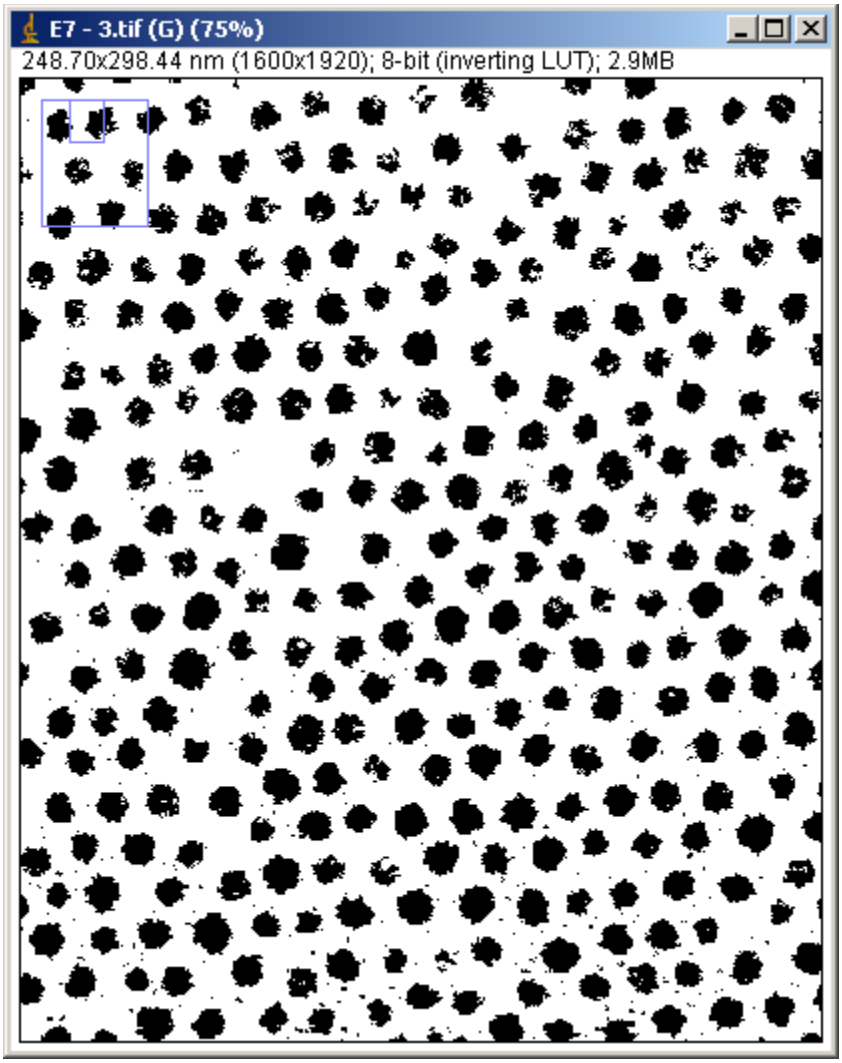

If you have nanoparticle coloring issues, where they overlap etc, that's ok, just use the section of the image where the particles look great!

If particles are touching each other, it can get tricky. So use the Watershed tool.
CLICK >>Process >> Binary >> Watershed
Make sure your particles are spherical, and clearly represent the sample you are measuring!

2) Make sure you have the correct measurements selected to measure

CLICK >>Analyze >> Set Measurements

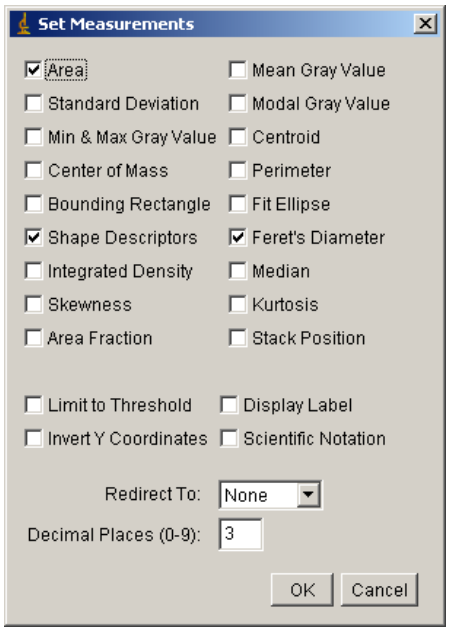

3) Count your particles

CLICK >> Analyze >> Analyze Particles
*make sure to "show outlines" to verify you are counting what you think you are counting.

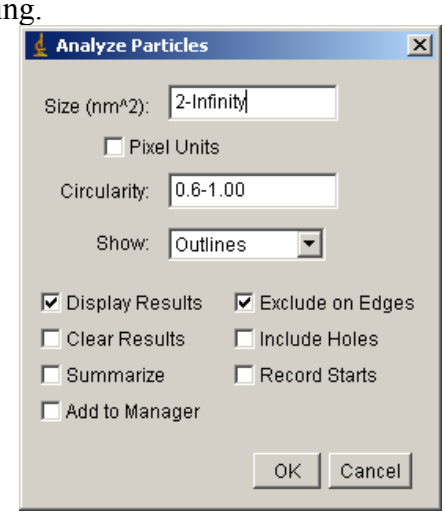

4) Collect data

Results

File Edit Font

	Area	Circ.	Feret	FeretAngle	MinFeret	AR	Round	Solidity
776	7.211	0.554	3.801	101.768	3.042	1.110	0.901	0.836
777	11.994	0.640	4.816	176.309	3.968	1.115	0.897	0.835
778	5.384	0.612	3.340	21.801	2.676	1.103	0.907	0.833
779	7.620	0.688	3.876	53.130	3.153	1.138	0.879	0.872
780	7.211	0.536	3.876	16.260	3.128	1.134	0.882	0.821
781	10.168	0.575	4.664	158.552	3.566	1.172	0.853	0.831
782	8.341	0.680	3.727	16.928	3.238	1.103	0.906	0.884
783	8.990	0.518	4.464	69.677	3.509	1.125	0.889	0.784
784	8.076	0.571	3.835	75.964	3.215	1.114	0.898	0.833
785	12.643	0.597	4.528	141.953	4.136	1.041	0.961	0.865
786	11.778	0.593	4.809	20.772	3.898	1.116	0.896	0.851
787	10.504	0.536	4.507	130.815	3.721	1.107	0.904	0.850
788	8.197	0.604	3.829	121.759	3.522	1.222	0.818	0.822
789	8.894	0.593	4.266	19.093	3.357	1.164	0.859	0.846
790	8.894	0.638	4.078	171.254	3.340	1.145	0.873	0.849
791	8.846	0.534	4.440	77.905	3.256	1.398	0.715	0.826
792	10.672	0.566	4.743	11.310	3.826	1.052	0.950	0.815
793	9.831	0.723	4.232	28.443	3.566	1.034	0.967	0.906
794	8.076	0.625	4.070	107.745	3.327	1.138	0.879	0.851

Book2 - Micro

Home Insert Page Layout Formulas Data Review View

Cut Copy Format Painter Paste Clipboard

Calibri 11 Font

Wrap Text Merge & Center Alignment

General

K10

	A	B	C	D	E	F	G	H	I	J
1	Number	Area	Circ	Diameter	Angle	Min Diam.	AR	Roudness	Solidity	
2	1	8.749	0.7	3.775	109.179	3.411	1.08	0.926	0.883	
3	2	6.033	0.555	3.775	70.821	2.718	1.353	0.739	0.777	
4	3	5.865	0.675	3.237	16.699	2.669	1.245	0.803	0.837	
5	4	6.226	0.532	3.498	77.196	2.77	1.317	0.759	0.824	
6	5	5.721	0.564	3.101	53.13	2.791	1.045	0.957	0.852	
7	6	7.187	0.522	3.727	45	3.093	1.121	0.892	0.807	
8	7	5.937	0.526	3.484	147.724	2.777	1.138	0.878	0.798	
9	8	7.067	0.679	3.734	48.366	2.944	1.235	0.809	0.861	
10	9	6.995	0.673	3.484	110.854	3.175	1.047	0.955	0.848	
11	10	5.529	0.52	3.442	172.235	2.741	1.058	0.945	0.768	
12	11	6.129	0.516	3.535	127.875	2.789	1.28	0.781	0.843	
13	12	8.894	0.684	4.093	24.624	3.179	1.301	0.769	0.875	
14	13	6.418	0.506	3.318	142.595	2.997	1.144	0.874	0.85	
15	14	7.548	0.521	3.888	66.501	3.238	1.148	0.871	0.833	
16	15	8.052	0.582	3.785	145.008	3.256	1.136	0.88	0.87	
17	16	7.043	0.6	3.619	99.866	3.101	1.158	0.863	0.852	
18	17	5.048	0.698	3.196	112.834	2.521	1.32	0.758	0.861	
19	18	7.884	0.593	3.851	40.101	3.256	1.15	0.87	0.853	
20	19	6.634	0.659	3.386	164.055	2.98	1.074	0.931	0.858	
21	20	7.187	0.508	3.775	19.179	3.101	1.099	0.91	0.787	
22	21	9.903	0.667	4.232	98.427	3.565	1.184	0.845	0.857	
23	22	4.231	0.589	2.913	64.799	2.326	1.339	0.747	0.819	
24	23	5.553	0.527	3.432	161.565	2.885	1.181	0.847	0.78	
25	24	7.355	0.576	3.606	154.537	3.256	1.075	0.931	0.83	
26	25	7.331	0.556	3.539	61.189	3.123	1.144	0.874	0.862	
27	26	6.129	0.53	3.4	133.152	2.946	1.103	0.907	0.812	

Sheet1 Sheet2 Sheet3

Ready

5) Data Analysis:

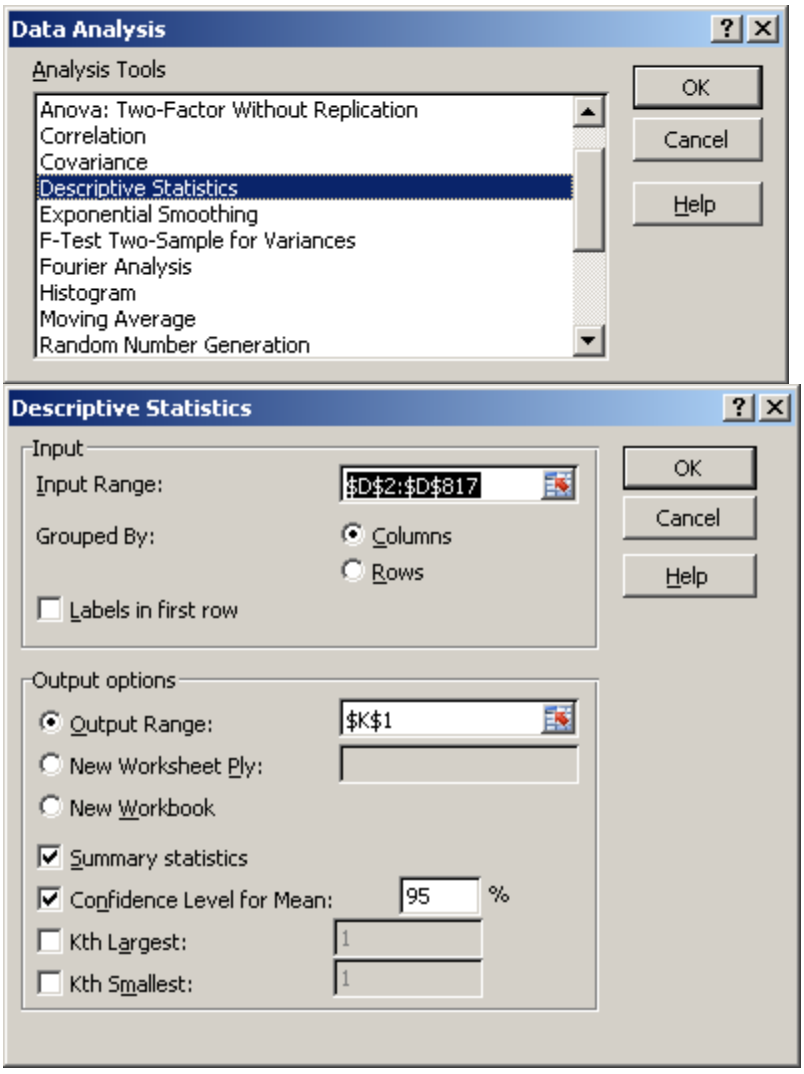

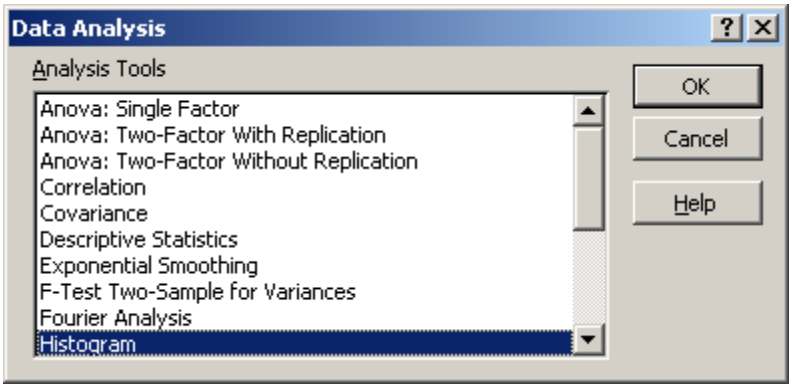

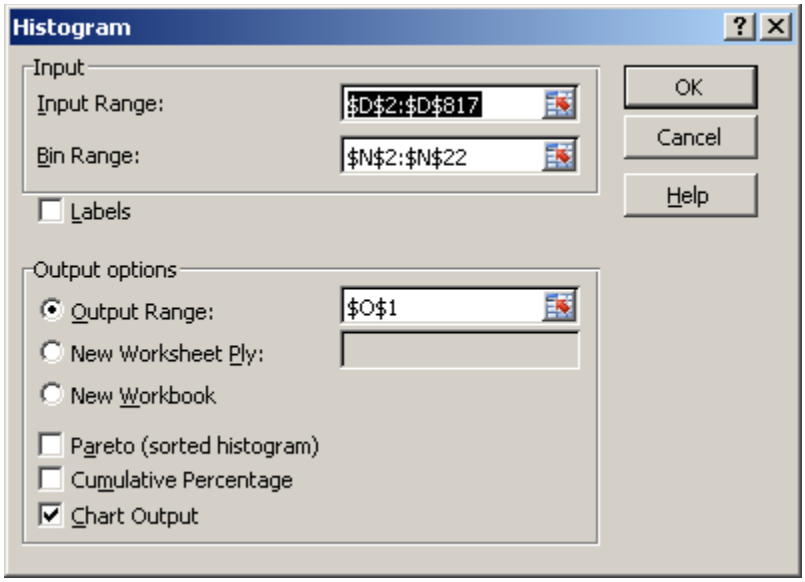
Histogram
Input
Input Range:
$D$2:$D$817
Bin Range:
$N$2:$N$22
Labels
OK
Cancel
Help
Output options
Output Range:
$O$1
New Worksheet Ply:
New Workbook
Pareto (sorted histogram)
Cumulative Percentage
Chart Output

APPENDIX E

MULTI-ANGLE LIGHT AND DYNMAIC LIGHT SCATTERING

General Notes

- Clean all glassware thoroughly prior to sample preparation and sample loading
- Ensure no fingerprints are evident on the outside of the scintillation vial by cleaning with a Kimwipe and alcohol
- Light scattering samples should be loaded into scintillation vials and contain at least 5 mL of sample.
- The calibration constant should be measured and updated once a month and hand written on a sticky note visible on the front of the instrument. Please see the Astra Operator's manual for further discussion.

Getting Started

- Load your solvent sample into the instrument
- Initiate the Astra Software
- Begin a new experiment
    - CLICK >> File >> New >> Experiment from Default
        - I have already created default templates for DLS so no new templates creations are necessary

- Selective solvent

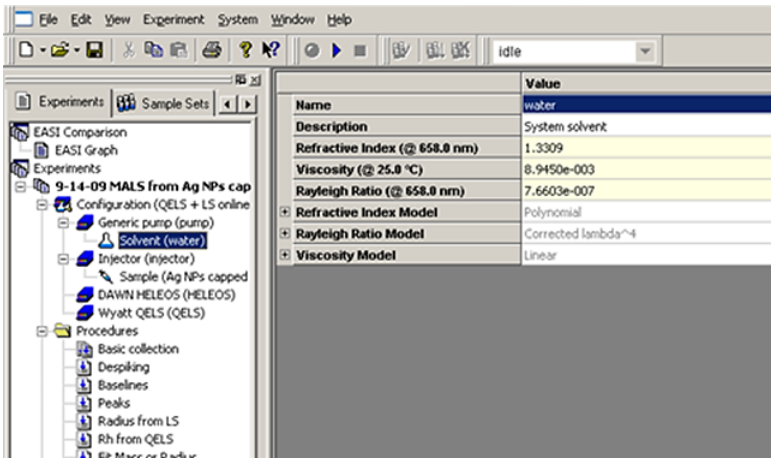

- Give your sample a name

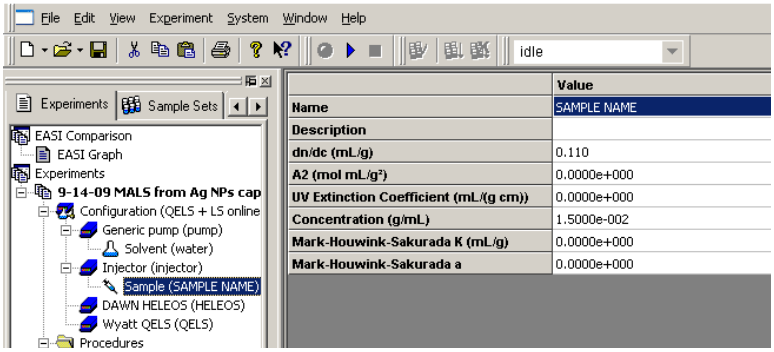

- For colored solutions, including nanoparticle dispersions make sure you set the divide laser to the FORWARD MONITOR

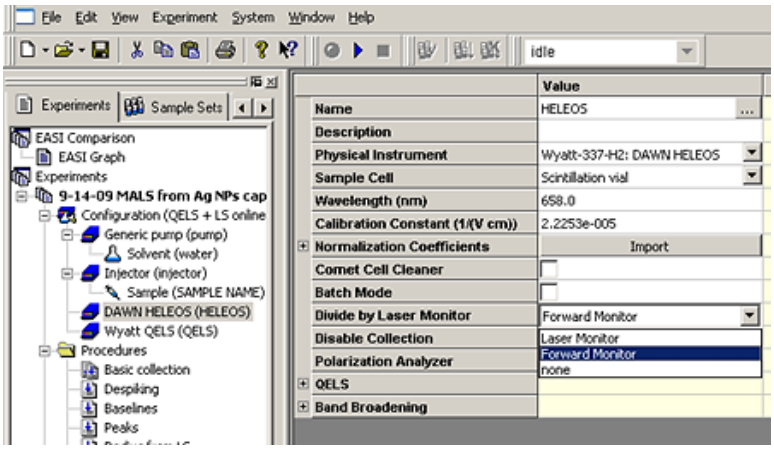

- Make sure your calibration constant matches the value hand written on the top of the instrument—the calibration constant should be measured once a month
- CLICK >> Experiment >> Run

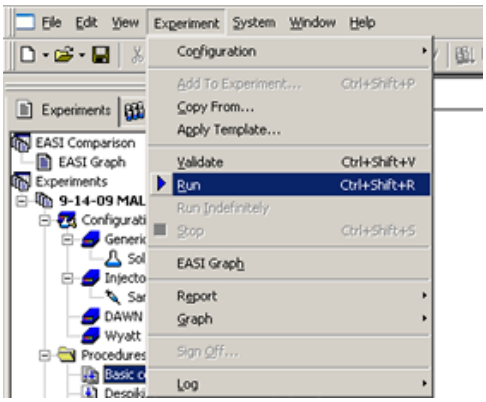

- CLICK >> Experiment >> Run Indefinitely
    - Failure to do so will result in the experiment automatically terminating after 15 min

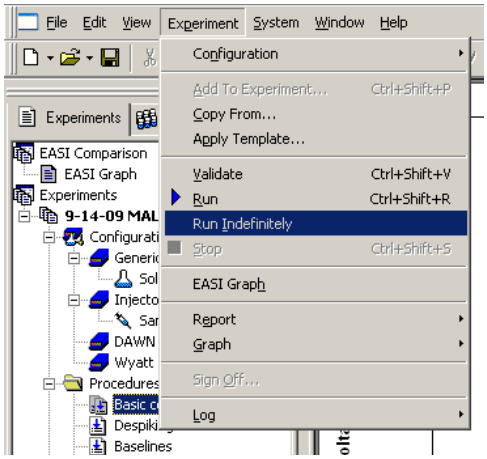

- Click Basic Collection to monitor scattering from solvent
- Measure the solvent scattering for ~2 to 5 min
    - Ensure that scattering from your solvent is a FLAT LINE producing low scattering intensities—this is dependent upon the solvent
- Remove the solvent, and put your sample into the instrument.
- Measure sample light scattering for at least 5 min
    - Ensure that the sample scattering is a flat line, and the scattering intensity at least an order of magnitude larger than the solvent scattering
- Remove sample from instrument, and replace with the solvent again
- Measure the solvent scattering for ~2 to 5 min
    - Ensure that scattering from your solvent is a FLAT LINE producing low scattering intensities—this is dependent upon the solvent

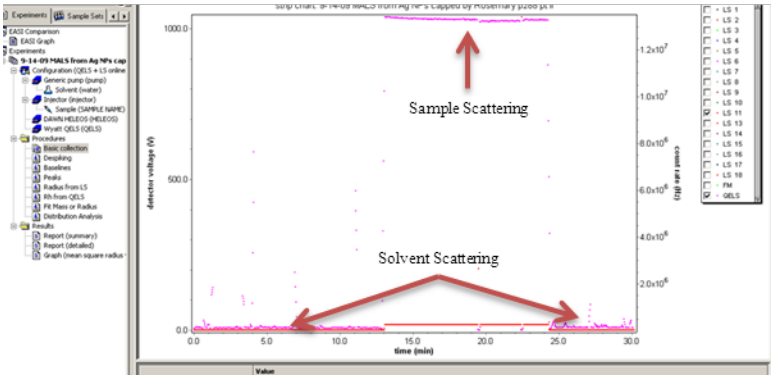

- Select your background scattering in the baselines menu for LS detector 11 and then CLICK Autobaseline
- Ensure all LS detectors have a flat line

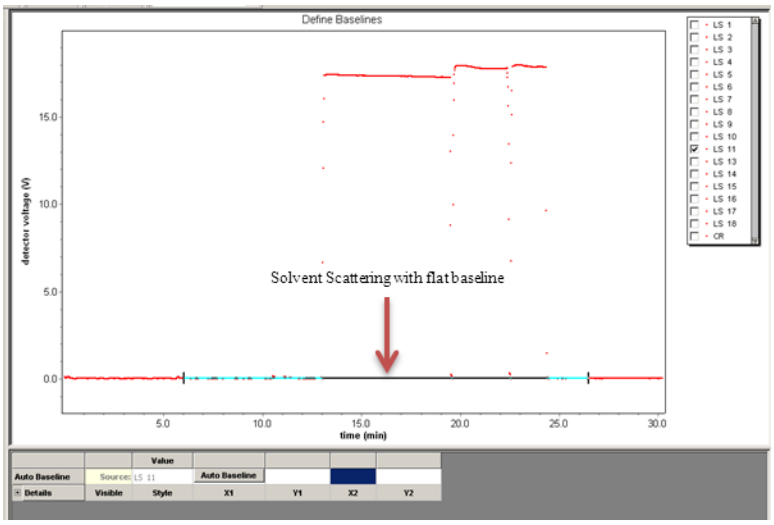

- CLICK Peaks in the left menu to define peaks

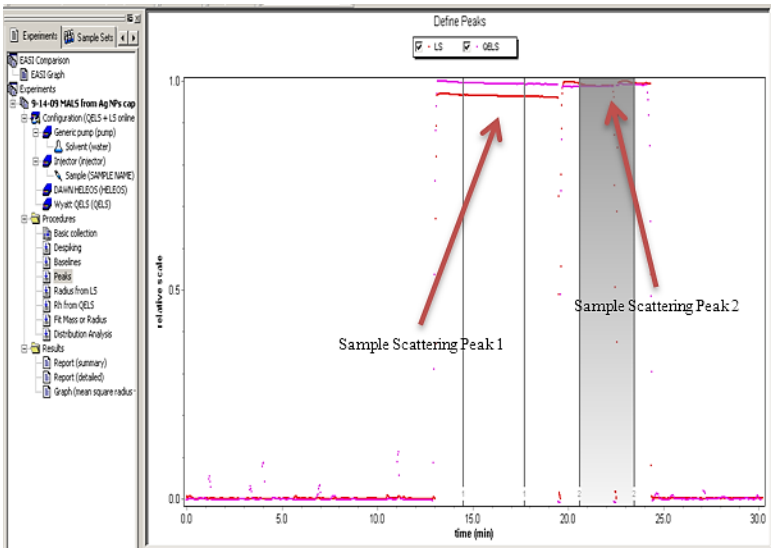

- CLICK Report Detailed to obtain the light scattering results

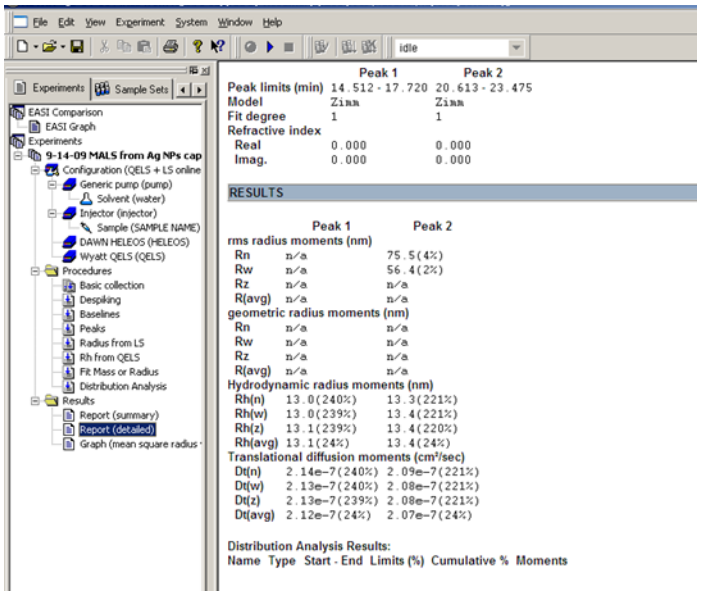

	Peak 1	Peak 2
Peak limits (min)	14.512 - 17.720	20.613 - 23.475
Model	Zimm	Zimm
Fit degree	1	1
Refractive index		
Real	0.000	0.000
Imag.	0.000	0.000

RESULTS

	Peak 1	Peak 2
rms radius moments (nm)		
Rn	n/a	75.5(4%)
Rw	n/a	56.4(2%)
Rz	n/a	n/a
R(avg)	n/a	n/a
geometric radius moments (nm)		
Rn	n/a	n/a
Rw	n/a	n/a
Rz	n/a	n/a
R(avg)	n/a	n/a
Hydrodynamic radius moments (nm)		
Rh(n)	13.0(240%)	13.3(221%)
Rh(w)	13.0(239%)	13.4(221%)
Rh(z)	13.1(239%)	13.4(220%)
Rh(avg)	13.1(24%)	13.4(24%)
Translational diffusion moments (cm²/sec)		
Dt(n)	2.14e-7(240%)	2.09e-7(221%)
Dt(w)	2.13e-7(240%)	2.08e-7(221%)
Dt(z)	2.13e-7(239%)	2.08e-7(221%)
Dt(avg)	2.12e-7(24%)	2.07e-7(24%)

Distribution Analysis Results:

Name	Type	Start - End	Limits (%)	Cumulative %	Moments

AMERICAN CHEMICAL SOCIETY LICENSE
TERMS AND CONDITIONS

Nov 08, 2010

This is a License Agreement between Gregory V White II ("You") and American Chemical Society ("American Chemical Society") provided by Copyright Clearance Center ("CCC"). The license consists of your order details, the terms and conditions provided by American Chemical Society, and the payment terms and conditions.

All payments must be made in full to CCC. For payment instructions, please see information listed at the bottom of this form.

License Number	2544280985801
License Date	Nov 08, 2010
Licensed content publisher	American Chemical Society
Licensed content publication	The Journal of Physical Chemistry C
Licensed content title	Small-Angle Neutron Scattering of Silver Nanoparticles in Gas-Expanded Hexane
Licensed content author	Gregory Von White et al.
Licensed content date	Oct 1, 2010
Volume number	114
Issue number	39
Type of Use	Thesis/Dissertation
Requestor type11	Not specified
Format	Print
Portion	Full article
Author of this ACS article	Yes
Order reference number	
Title of the thesis / dissertation	Synthesis, Stabilization, and Characterization of Metal Nanoparticles
Expected completion date	Dec 2010
Estimated size(pages)	177
Billing Type	Invoice
Billing Address	114 Heritage Riverwood Drive Apt. B Central, SC 29630 United States
Customer reference info	
Total	0.00 USD
Terms and Conditions	

Thesis/Dissertation

ACS / RIGHTSLINK TERMS & CONDITIONS
THESIS/DISSERTATION

INTRODUCTION
The publisher for this copyrighted material is the American Chemical Society. By clicking "accept" in connection with completing this licensing transaction, you agree that the following terms and conditions apply to this transaction (along with the Billing and Payment terms and conditions established by Copyright Clearance Center, Inc. ("CCC"), at the time that you opened your Rightslink account and that are available at any time at <http://myaccount.copyright.com>).

LIMITED LICENSE
Publisher hereby grants to you a non-exclusive license to use this material. Licenses are for one-time use only with a maximum distribution equal to the number that you identified in the licensing process; any form of republication must be completed within 60 days from the date hereof (although copies prepared before then may be distributed thereafter).

GEOGRAPHIC RIGHTS: SCOPE
Licenses may be exercised anywhere in the world.

RESERVATION OF RIGHTS
Publisher reserves all rights not specifically granted in the combination of (i) the license details provided by you and accepted in the course of this licensing transaction, (ii) these terms and conditions and (iii) CCC's Billing and Payment terms and conditions.

PORTION RIGHTS STATEMENT: DISCLAIMER
If you seek to reuse a portion from an ACS publication, it is your responsibility to examine each portion as published to determine whether a credit to, or copyright notice of, a third party owner was published adjacent to the item. You may only obtain permission via Rightslink to use material owned by ACS. Permission to use any material published in an ACS publication, journal, or article which is reprinted with permission of a third party must be obtained from the third party owner. ACS disclaims any responsibility for any use you make of items owned by third parties without their permission.

REVOCATION
The American Chemical Society reserves the right to revoke a license for any reason, including but not limited to advertising and promotional uses of ACS content, third party usage, and incorrect figure source attribution.

LICENSE CONTINGENT ON PAYMENT
While you may exercise the rights licensed immediately upon issuance of the license at the end of the licensing process for the transaction, provided that you have disclosed complete and accurate details of your proposed use, no license is finally effective unless and until full payment is received from you (by CCC) as provided in CCC's Billing and Payment terms and conditions. If full payment is not received on a timely basis, then any license preliminarily granted shall be deemed automatically revoked and shall be void as if never granted. Further, in the event that you breach any of these terms and conditions or any of CCC's Billing and Payment terms and conditions, the license is automatically revoked and shall be void as if never granted. Use of materials as described in a revoked license, as well as any use of the materials beyond the scope of an unrevoked license, may constitute copyright infringement and publisher reserves the right to take any and all action to protect

its copyright in the materials.

COPYRIGHT NOTICE: DISCLAIMER
You must include the following copyright and permission notice in connection with any reproduction of the licensed material: "Reprinted ("Adapted" or "in part") with permission from REFERENCE CITATION. Copyright YEAR American Chemical Society."

WARRANTIES: NONE
Publisher makes no representations or warranties with respect to the licensed material.

INDEMNITY
You hereby indemnify and agree to hold harmless publisher and CCC, and their respective officers, directors, employees and agents, from and against any and all claims arising out of your use of the licensed material other than as specifically authorized pursuant to this license.

NO TRANSFER OF LICENSE
This license is personal to you or your publisher and may not be sublicensed, assigned, or transferred by you to any other person without publisher's written permission.

NO AMENDMENT EXCEPT IN WRITING
This license may not be amended except in a writing signed by both parties (or, in the case of publisher, by CCC on publisher's behalf).

OBJECTION TO CONTRARY TERMS
Publisher hereby objects to any terms contained in any purchase order, acknowledgment, check endorsement or other writing prepared by you, which terms are inconsistent with these terms and conditions or CCC's Billing and Payment terms and conditions. These terms and conditions, together with CCC's Billing and Payment terms and conditions (which are incorporated herein), comprise the entire agreement between you and publisher (and CCC) concerning this licensing transaction. In the event of any conflict between your obligations established by these terms and conditions and those established by CCC's Billing and Payment terms and conditions, these terms and conditions shall control.

JURISDICTION
This license transaction shall be governed by and construed in accordance with the laws of the District of Columbia. You hereby agree to submit to the jurisdiction of the courts located in the District of Columbia for purposes of resolving any disputes that may arise in connection with this licensing transaction.

THESES/DISSERTATION TERMS
Publishing implications of electronic publication of theses and dissertation material
Students and their mentors should be aware that posting of theses and dissertation material on the Web prior to submission of material from that thesis or dissertation to an ACS journal may affect publication in that journal. Whether Web posting is considered prior publication may be evaluated on a case-by-case basis by the journal's editor. If an ACS journal editor considers Web posting to be "prior publication", the paper will not be accepted for publication in that journal. If you intend to submit your unpublished paper to ACS for publication, check with the appropriate editor prior to posting your manuscript electronically.

If your paper has already been published by ACS and you want to include the text or portions of the text in your thesis/dissertation in **print or microfilm formats**, please print the

ACS copyright credit line on the first page of your article: "Reproduced (or 'Reproduced in part') with permission from [FULL REFERENCE CITATION.] Copyright [YEAR] American Chemical Society." Include appropriate information.

Submission to a Dissertation Distributor: If you plan to submit your thesis to UMI or to another dissertation distributor, you should not include the unpublished ACS paper in your thesis if the thesis will be disseminated electronically, until ACS has published your paper. After publication of the paper by ACS, you may release the entire thesis (**not the individual ACS article by itself**) for electronic dissemination through the distributor; ACS's copyright credit line should be printed on the first page of the ACS paper.

Use on an Intranet: The inclusion of your ACS unpublished or published manuscript is permitted in your thesis in print and microfilm formats. If ACS has published your paper you may include the manuscript in your thesis on an intranet that is not publicly available. Your ACS article cannot be posted electronically on a publicly available medium (i.e. one that is not password protected), such as but not limited to, electronic archives, Internet, library server, etc. The only material from your paper that can be posted on a public electronic medium is the article abstract, figures, and tables, and you may link to the article's DOI or post the article's author-directed URL link provided by ACS. This paragraph does not pertain to the dissertation distributor paragraph above.

Other conditions:

v1.1

Gratis licenses (referencing $0 in the Total field) are free. Please retain this printable license for your reference. No payment is required.

If you would like to pay for this license now, please remit this license along with your payment made payable to "COPYRIGHT CLEARANCE CENTER" otherwise you will be invoiced within 48 hours of the license date. Payment should be in the form of a check or money order referencing your account number and this invoice number RLNK10879325.
Once you receive your invoice for this order, you may pay your invoice by credit card. Please follow instructions provided at that time.

Make Payment To:
Copyright Clearance Center
Dept 001
P.O. Box 843006
Boston, MA 02284-3006

If you find copyrighted material related to this license will not be used and wish to cancel, please contact us referencing this license number 2544280985801 and noting the reason for cancellation.

Questions? customercare@copyright.com or +1-877-622-5543 (toll free in the US) or +1-978-646-2777.